Topology optimization for the duct flow problems in laminar and turbulent flow regimes

Seiji Kubo

2019

I would like to dedicate this thesis to my loving family ...

Acknowledgements

First, I would like to show my greatest appreciation to my supervisors, Professor Shinji Nishiwaki, Professor Kazuhiro Izui, and Professor Takayuki Yamada, for their constant encouragement and continuing support during my doctoral studies. I have been able to keep going on because of their intellectual and invaluable advice. I have greatly benefited from the discussion with them.

In addition, I would like to thank several individuals in IHI Corporation. : Dr. Hideto Ikeda, Senior Technical Advisor; Dr. Masafumi Kawai, Chief Engineer; Dr. Masahito Yamaguchi, Chief Engineer; Dr. Takayuki Nishido, General Manager of Technical Research & Development Center at IHI Inspection & Instrumentation Co., Ltd.; Dr. Hidenari Baba, General Manager, Intellectual Property Department; Dr. Iton Chou, General Manager of Research Laboratory; Dr. Yasuhiro Ootake, Deputy General Manager of Research Laboratory; Mr. Osamu Watanabe, Manager; Mr. Kazuo Shimamura, General Manager, Computational & Mathematical Engineering Department; Mr. Motoaki Shito, Manager of Computational Engineering Group; Dr. Takahiro Shimada, Manager of Mathematical Science Group. During my doctoral work at Kyoto University, they have provided the special consideration to my academic research. If not for their receptive attitude and patient, my doctoral dissertation would not be able to be accomplished.

I am also indebt to Professor Kentaro Yaji at Osaka University for his constructive comments and constant discussion with me. I have been impressed at your deep insight into the difficult challenges in a specific issue.

Dr. Atsushi Koguchi at IDAJ Co., LTD. whose meticulous comments were an enormous help to me, especially for the topology optimization of turbulent flow using the IBM.

I would like to show my special thanks to all the members in the Manufacturing Systems Engineering Laboratory at Kyoto University for their kindness during my visit to the Nishiwaki Lab. I would also like to thank Mr. John Goodman for his help in editing the papers I have written in English.

I am extremely grateful to Dr. Tsuguo Kondoh, who have given me the fundamental and thought-provoking advice to the fluid dynamics and optimization approach for the fluids.

Finally, I would like to express my gratitude to my parents for their encouragement. Also, I offer special thanks to my wife, Sayaka Kubo, and my daughter of twins, Hinako Kubo and Nanako Kubo, for their warm support continuously. I have been encouraged from their carefree smiles throughout my doctoral work.

Kyoto, March, 2019

Seiji Kubo

Table of contents

Chapter 1

General introduction

Currently, complex fluid flow in engineering applications can be analyzed using Computational Fluid Dynamics (CFD) through the use of commercial or open-source software. Additionally, due to steady progress in CPU performance, structural optimization approaches have become more attractive and realistic in engineering design applications. For the design of highly efficient configurations of fluidic devices, a numerical approach using structural optimization is considered most useful for exploring the most promising designs among a number of design candidates. In particular, the structures of fluidic devices such as switches, amplifiers, and oscillators, are often composed of complicated flow channel layouts which have multi-terminal and number of inlets and outlets. For the design of such kind of fluidic devices, the achievement of the designated flow rate on each flow channels or outlets is the important design issue in the design process.

With respect to optimization approaches, especially based on the adjoint method, after the pioneering work of Pironneau [60], wide-ranging research for fluid dynamics problems has been conducted [61, 56, 84, 85, 16]. A shape optimization approach is most often applied in aerodynamic optimization problems, such as the optimal shape design of NACA airfoils [37], turbine blades [71], and aircraft wings [16], since small modifications in shape have

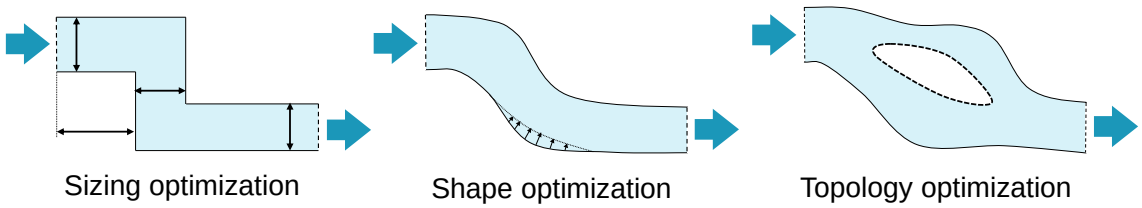

Fig. 1.1 Classification of structural optimization.

sufficient impact on the improvement of a performance, e.g., when drag minimization is an objective.

Regarding to the optimization methods, as shown in Fig. 1.1, the topology optimization approach [12] is an attractive optimization method that offers certain advantages compared with sizing and shape optimization methods, due to its superior flexibility with respect to configuration changes, and allowance of the creation and disappearance of holes during the optimization, which can lead to innovative optimal configurations.

Concerning topology optimization methods applied to fluid problems, Borrvall and Petersson first proposed a method for minimum power dissipation under Stokes flow [14], and this method was later extended to moderate Reynolds number (<1000) laminar flow regimes [31, 51, 30, 83, 24, 1, 20, 44, 80].

In particular, concerning the flow rate constraint for a topology optimization problem, Gersborg-Hansen et al. [30] addressed a topology optimization problem that included an outflow rate constraint under Stokes flow, and obtained an appropriate maximum penalization value corresponding to an artificial source term that was added to the governing equation for the fluid. Aage et al. [1] later extended this approach to large scale 2D and 3D problems. Deng et al. [20] dealt with unsteady incompressible Navier-Stokes flow for the minimization of viscous energy dissipation under an outflow rate constraint within a specific time interval. Liu et al. [44] used the augmented Lagrangian method [34, 62] to replace a flow rate constrained optimization problem under steady-state incompressible Navier-Stokes flow with an unconstrained problem. In their method, the Lagrange multipliers were calculated by solving

additional linearized Navier-Stokes equations, separately from the optimization calculation. Moreover, most of these studies have been on basic topics, for example, examination the formulation or implementation of a topology optimization method for fluids; studies on the development of design methods for actual microchannel devices are relatively scarce.

By the way, from an engineering point of view, in addition to the laminar flow regimes, fluid behavior can be assumed to be turbulent flow, except in microscale fluid machinery such as a microelectromechanical systems (MEMS). However, there has been relatively little research conducted on topology optimization for turbulent flow regimes, compared with the prevalence of shape optimization approaches.

In the conventional topology optimization approaches[57, 38, 82, 23] based on the pioneering work by Borrvall and Petersson[14], employing the so-called Brinkman penalization method, the fixed design domain is assumed to be a porous medium by introducing the Darcy force term as an external source term in the Navier-Stokes equation, where the local porosities are considered as design variables. When considering the physical and numerical characteristics in turbulent flows, the imposition of the wall function, which express the interpolated velocity profile near the wall based on empirical laws, requires clear boundaries in the expression of the fluid-solid interface in the topology optimization. However, in those conventional approaches, the fluid-solid interface lacks clear boundaries because the interface is expressed as a porous medium. Also, when the Brinkman penalization method is used, the no-slip boundary condition can not be explicitly applied to the fluid-solid interface because the porous medium by nature has an indistinct interface.

To fundamentally overcome the problem of the imprecise expression of the fluid-solid interface, there are two important requirements: 1) explicit imposition of the no-slip boundary condition on the interface during the topology optimization process, and 2) a method that expresses the fluid-solid interface with clear boundaries.

Corresponding to the first requirement, an immersed boundary method (IBM) [59, 58] is a popular technique used in CFD analyses to explicitly impose the no-slip boundary condition by adding a body force to the Navier-Stokes equation as a reaction force from an object, using a fixed Cartesian grid.

For clear expression of the fluid-solid interface, the second critical requirement for precise evaluation of the fluid behavior near the wall under turbulent flow, a level set method is attractive. Following the basic methodology for tracking fronts and free boundaries proposed by Osher and Sethian [52], a level set method proposed for structural optimization [77, 3] enjoyed wide use for structural topology optimization problems, along with the SIMP method. In this method, the design domain is fundamentally free of grayscales because structural boundaries are represented as the iso-surface of a scalar function, the level set function (LSF).

In a previous study of a level set-based topology optimization method using the IBM, Kreissl et al. [39] proposed a topology optimization method for a laminar flow problem using an XFEM formulation of the incompressible Navier-Stokes equations, without employing the Brinkman approach. In their method, the no-slip boundary condition along the fluid-solid interface is enforced with a stabilized Lagrange multiplier method. Accordingly, the use of the XFEM inhibits the unrealistic flow penetration through thin walls that can occur when applying Brinkman penalization.

The outline of this thesis is as follows:

In Chapter 2, to develop an energy-efficient structure for MEMS scale fluidic device, we apply a topology optimization method to an optimal design problem for a steady state incompressible viscous flow. We use a level set-based topology optimization method incorporating the concept of the phase field method so that clear boundaries between the solid and fluid domains are expressed in the optimal configurations. To define the topology optimization problem for a fluid regime, the expressions of the primary and adjoint problems are formulated concretely, to minimize the total potential energy of fluids. Moreover, to

ensure the intended design outflow rate at a designated outlet, the optimization problem includes an outflow rate inequality constraint. To deal with the flow rate constraint, we propose a simple way to determine the Lagrange multiplier, which need not to be obtained by additional calculations during the optimization process. Following the concept of the standard adjoint variable method, a stable optimization process that satisfies the outflow rate inequality constraint is achieved. Two numerical examples, one for two-terminal and the other for multi-terminal flow, are provided to demonstrate the usefulness of the proposed level set-based topology optimization method.

In Chapter 3, we propose an optimal design method for plate-type microchannel reactor manifolds, based on the topology optimization method considering the flow rate constraints constructed in Chapter 2. Here, we implement a flow rate inequality constraint, which constrains the flow rate deviation in each target microchannel to achieve an acceptable degree of flow uniformity. We provide the validity of our proposed optimization method applying the manifold design problems for Z- and U-type microchannel reactors as numerical examples.

In Chapter 4, we propose a level set-based topology optimization method for duct flow problems considering turbulent flow without using the Brinkman penalization approach. We apply a RANS model based on the high-Reynolds-number treatment and include the wall function in the optimization problem, and introduce two-equation turbulence models, k-ϵ and k-ω, in this thesis. In the proposed topology optimization process, owing to the introduction of a LSF, we precisely and explicitly impose a no-slip boundary condition along the fluid-solid interface in the fixed design domain, using the IBM, a much different approach than the previous Brinkman penalization method in which the fluid-solid interface is expressed as a porosity. Finally, we present numerical examples to verify the utility of our proposed optimization method.

The last Chapter of this thesis provides a general conclusion.

Chapter 2

Topology optimization for laminar flow considering outflow rate constraints

2.1 Introduction

The aim of this Chapter is to construct the level set-based topology optimization method considering out flow rate inequality constraints to minimize the total potential energy of the laminar flows.

Historically, fluidic devices such as switches, amplifiers, and oscillators, have an advantage, compared with electronic devices, in terms of maintenance-free operation and operating life. Therefore, prior to the great progress in electronic technologies that has occurred during the past several decades, the structure and function of fluidic devices were the subject of extensive research. In particular, the structures of these fluidic devices are often composed of complicated flow channel layouts. Recently, fluidic devices are again attracting significant attention, stimulated by progress in the development of MEMS technologies.

In this Chapter, to develop an energy-efficient structure for a MEMS-scale fluidic device, we apply a topology optimization method to an optimal design problem for a steady state incompressible viscous flow field. We also introduce a level set-based topology optimization

method incorporating the concept of the phase field method for the topology optimization so that clear boundaries between the solid and fluid domains are expressed in the optimal configurations. To define the topology optimization problem for a fluid regime, the expressions of the primary and adjoint problems are formulated concretely, to minimize the total potential energy of fluids. Moreover, to ensure the intended design outflow rate at a designated outlet, the optimization problem includes an outflow rate inequality constraint. Following the concept of the standard adjoint variable method, a stable optimization process that satisfies the outflow rate inequality constraint is achieved. Two numerical examples, one for two-terminal and the other for multi-terminal flow, are provided to demonstrate the usefulness of the proposed level set-based topology optimization method.

2.2 Topology optimization method

Topology optimization methods [12] can be employed as an alternative to size and shape optimization methods, and offer superior flexibility for the creation of innovative structural configurations of the microchannel reactors because changes in both the shape and the topology of the target structure can be allowed. Currently, topology optimization methods are widely applied to a variety of structural optimization problems such as stiffness maximization problems [72, 3], vibration problems [21, 45], optimum design problems for compliant mechanisms [65, 50], and thermal problems [15, 47].

The basic concept of topology optimization is the extension of a design domain to a fixed design domain and the replacement of a structural optimization problem with a material distribution problem, using a characteristic function. The density approach, also called the solid isotropic material with penalization (SIMP) method [13], is widely used for solving topology optimization problems. The basic idea of the density approach is to introduce a fictitious isotropic material whose elasticity tensor is assumed to be a function of penalized material density. However, in the density approach, the existence of intermediate material

density, the so-called grayscales, are essentially allowed in the fixed design domain. From an engineering standpoint, since the grayscales which can be regarded as a porous material in the physical sense are difficult to manufacture and may be infeasible, it is necessary to introduce a filtering technique, e.g., [66], to remove the grayscales.

Level set method for structural optimization [77, 3] is an another popular approach in the field of structural optimization, since Osher and Sethian [52] proposed a basic methodology for tracking fronts and free boundaries. In this method, since the structural boundaries are represented as the iso-surface of a scalar function called level set function, the design domain is essentially grayscale-free. However, conventional level set-based approaches are classified as shape optimization methods because their basic idea is that an optimal configuration is obtained by moving the structural boundaries, which are expressed using the iso-surface of level set function and are evolved by solving a Hamilton-Jacobi equation. In particular, Otomori et al. [54] mentioned that when an advection equation is used for updating the level set function, the generation of new hole boundaries can occur when the boundary of an existing hole is pinched off during advection, and this situation can easily occur in three-dimensional problems. As a result, the obtained optimal configurations are dependent on the initial configuration settings. To overcome this dependency and allow explicit creation of new holes inside the fixed design domain during the optimization process, Allaire et al. [2] proposed a methodology based on the concept of the bubble method [27] incorporating topological derivatives [68]. Yamada et al. [81] have recently proposed a level set-based approach that uses a topological derivative and a reaction-diffusion equation, whereas the conventional level set-based approach uses a shape derivative and the advection equation for evolving the level set function. The advantage of Yamada et al.'s method is that not only the topological changes are allowed during the optimization process but also it is unnecessary to conduct a reinitialization treatment, which is typically required conventional approaches to ensure accuracy when solving the Hamilton-Jacobi equation.

In this thesis, we construct the topology optimization method for fluid problems based on the level set-based boundary expression proposed by Yamada et al. [81].

2.3 Level set-based topology optimization method

Here, we introduce the level-set based topology optimization method used in this thesis. The basic concept in topology optimization is composed of the definition of the fixed design domain D and the introduction of the characteristic function $\chi_\Omega(\boldsymbol{x})$ as described below.

$$\chi_\Omega(\boldsymbol{x}) = \begin{cases} 1 & \text{if} \quad \boldsymbol{x} \in \Omega \\ 0 & \text{if} \quad \boldsymbol{x} \in D \setminus \Omega \end{cases} \tag{2.1}$$

where $\boldsymbol{x}$ is the position of the arbitrary nodal point in the fixed design domain D. The introduction of the characteristic function $\chi_\Omega(\boldsymbol{x})$ means that the optimization problem is replaced as the material distribution problem in the fixed design D which includes the domain Ω to be optimal domain. However, as long as using this definition of the characteristic function above, the optimization problem could be ill-posed problem, because the characteristic function $\chi_\Omega(\boldsymbol{x})$ is allowed to be a discontinuous value wherever in Ω. In order to overcome this problem, some kind of regularization method should be introduced. In this thesis, the regularization method based on the concept of phase field method is introduced. At first of it, as shown in Fig. 2.1, the level-set functional is defined below.

$$\begin{cases} 0 < \phi(\boldsymbol{x}) \leq 1 & \text{for} \quad \forall \boldsymbol{x} \in \Omega \setminus \partial\Omega \\ \phi(\boldsymbol{x}) = 0 & \text{for} \quad \forall \boldsymbol{x} \in \partial\Omega \\ -1 \leq \phi(\boldsymbol{x}) < 0 & \text{for} \quad \forall \boldsymbol{x} \in D \setminus \Omega \end{cases} \tag{2.2}$$

Then, the characteristic function $\chi_\Omega(\phi)$ is re-defined regarding it as the level-set functional,

$$\chi_\phi(\phi) = \begin{cases} 1 & \text{if} \quad \phi \geq 0 \\ 0 & \text{if} \quad \phi < 0 \end{cases} \tag{2.3}$$

By introduction of this definition, the arbitrary topology in the fixed design domain D can be represented by the level-set functional.

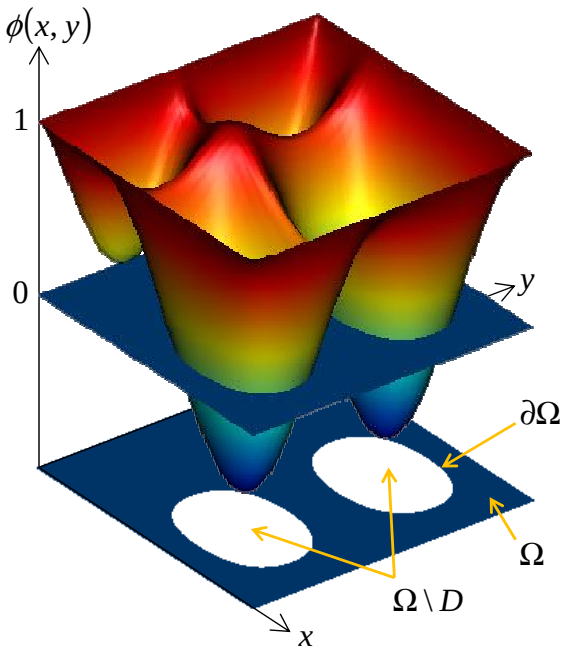

Fig. 2.1 Fixed design domain D and level set function ϕ

By using above shape representation method in level-set functional, the optimization problem can be represented by using the objective functional J and the constraint functional G like below.

$$\inf_{\phi} \qquad J(\Omega(\phi)) = \int_D j(\boldsymbol{x})\chi_\phi \mathrm{d}D \tag{2.4}$$

$$\text{subject to} \quad G(\Omega(\phi)) = \int_D g(\boldsymbol{x})\chi_\phi \mathrm{d}D - G_{\max} \leq 0 \tag{2.5}$$

where $G_{\max}$ is the upper limit of $\int_D g(\boldsymbol{x})\chi_\phi \mathrm{d}D$.

The level set function that satisfies the Karush-Kuhn-Tucker (KKT) conditions is a candidate solution for the optimal configuration. However, since it is not easy to find such solutions directly, we introduce a fictitious time, t, and then update the level set function ϕ using a convergence calculation of a time evolution equation. Since the level set function ϕ is assumed to be driven in proportion to the gradient of the augmented objective functional, the following time evolution equation can be derived [81]:

$$\frac{\partial \phi}{\partial t} = -K\bar{J}', \tag{2.6}$$

where $K > 0$ is a positive coefficient, and $\bar{J}'$ represents the gradient of the augmented objective functional $\bar{J}$, which is defined as follows.

$$\bar{J} = J + \lambda G, \tag{2.7}$$

where λ is a Lagrange undetermined multiplier.

Next, since the smoothness of the level set function, updated using Eq. (2.6), may not be preserved during the optimization process, a regularization term is introduced to the right-hand side of Eq. (2.6), as follows, to regularize of the optimization problem.

$$\frac{\partial \phi}{\partial t} = -K\left(\bar{J}' - \tau\nabla^2\phi\right). \tag{2.8}$$

Since the regularization term in the above equation is expressed as a diffusion term, $\nabla^2\phi$, Eq. (2.8) is a reaction-diffusion equation, and this term ensures the smoothness of the level set function in this method. Furthermore, since the degree of diffusivity can be controlled by setting the regularization parameter τ to a particular value, the geometric complexity of the obtained configuration can be qualitatively controlled. In this thesis, the distribution

of the level set function in the fixed design domain can be obtained by solving the above reaction diffusion equation. Due to introduction of this kind of regularization method, we can get the optimal configuration without grayscales in contrast with the conventional topology optimization method using the variable as the regularized density. Comprehensive literature concerning structural topology optimization based on level set methods is reviewed in [22].

2.4 Topology optimization of fluid problem

2.4.1 Governing equations

The time-independent behavior of the fluid can be described using the steady-state incompressible Navier-Stokes and continuity equations, as follows.

$$(\boldsymbol{u}\cdot\nabla)\,\boldsymbol{u}+\nabla p-\frac{1}{\mathrm{Re}}\nabla^2\boldsymbol{u}-\boldsymbol{f}=0 \tag{2.9}$$

$$-\nabla\cdot\boldsymbol{u}=0, \tag{2.10}$$

where $\boldsymbol{u}$ is velocity vector of the fluid, p is the pressure, and all variables in Eqs. (2.9) and (2.10) are normalized using the characteristic length L as the channel inlet length, the characteristic flow velocity U as the mean velocity at the channel inlet, the reference pressure p_0 at the channel outlet, and the fluid density ρ, as follows.

$$\boldsymbol{u}^*=\frac{\boldsymbol{u}}{U},\quad p^*=\frac{p-p_0}{\rho U^2},\quad \boldsymbol{x}^*=\frac{x}{L} \tag{2.11}$$

And in this thesis, the normalized variables are simply represented by $\boldsymbol{u}$, p instead of $\boldsymbol{u}^*$, p^*. Furthermore, in Eq (2.9), $\boldsymbol{f}$ is the source term and Re is the Reynolds number which is

defined as,

$$\mathrm{Re} = \frac{\rho L U}{\mu}, \tag{2.12}$$

where μ is a coefficient of molecular viscosity.

Regarding as boundary conditions, the prescribed flow inlet velocity at inlet boundary, Γ_{in}, and a no-slip condition at wall boundary, Γ_{wall}, as the Dirichlet condition, and the Neumann condition for pressure at outlet boundary, Γ_{out}, are assumed in this thesis:

$$\boldsymbol{u} = \boldsymbol{u}_{\mathrm{in}} \qquad \text{on } \Gamma_{\mathrm{in}} \tag{2.13}$$

$$\left[-p\mathbf{I} + \frac{1}{\mathrm{Re}}\left\{\nabla\boldsymbol{u} + (\nabla\boldsymbol{u})^{\mathrm{T}}\right\}\right]\cdot\boldsymbol{n} = \mathbf{0} \qquad \text{on } \Gamma_{\mathrm{out}} \tag{2.14}$$

$$\boldsymbol{u} = \mathbf{0} \qquad \text{on } \Gamma_{\mathrm{wall}} \tag{2.15}$$

where $\mathbf{I}$ is the identity matrix.

2.4.2 Expression of fluid and solid domains

Although, governing equations are defined only within the fluid domain Ω, the topology optimization is considered within the set of the fixed design domain D in which the shape of object can be deformed freely, combining the fluid domain Ω and the solid domain $D\backslash\Omega$.

Generally in topology optimization of fluids, to permit the changing of the topology of fluid domain Ω in the fixed design domain D, a source term $\boldsymbol{f}$ in Eq. (2.9) is assumed base on Darcy law, which is expressed as a body force $\boldsymbol{f}$ resisting flows [**?**]. Then,

$$\boldsymbol{f} = -\alpha\boldsymbol{u} \tag{2.16}$$

$$\alpha = (\alpha_{\mathrm{min}} - \alpha_{\mathrm{max}})\chi_{\phi} + \alpha_{\mathrm{max}}, \tag{2.17}$$

here, $\alpha_{\min}$ and $\alpha_{\max}$ are the impermeability coefficient in the fluid and solid domain, respectively.

Through the impermeability α, the fluid velocity $\boldsymbol{u}$ and the fluid pressure p depend on the level set function $\phi(\boldsymbol{x})$, which is defined as the design variable. Furthermore, the Navier-Stokes equation defined in the fluid domain Ω is extended to the fixed design domain D because of the α introduction. When the value $\chi_\phi = 1$ in the fluid domain, $\alpha_{\min}$ should be set as the small value so as to $\boldsymbol{f} = -\alpha_{\min}\,\boldsymbol{u}$ becomes the extremely small value. On the other hand, in the solid domain, identically, $\alpha_{\max}$ should be set as the large value so as to let the body force $\boldsymbol{f}$ be large compared with the value of the other terms in Eq. (2.9).

2.4.3 Objective functional

Objective functional J in this study represents the total potential energy of the fluid in the device, defined as the sum of the dissipated power and the work done by an external force, as formulated below [14].

$$J\left(\boldsymbol{u},\chi_\phi\right) := \int_D \frac{1}{2\mathrm{Re}}\left\{\nabla\boldsymbol{u} + (\nabla\boldsymbol{u})^{\mathrm{T}}\right\} : \left\{\nabla\boldsymbol{u} + (\nabla\boldsymbol{u})^{\mathrm{T}}\right\} \mathrm{d}D - \int_D \boldsymbol{f}\cdot\boldsymbol{u}\,\mathrm{d}D, \tag{2.18}$$

where $\{\nabla\boldsymbol{u} + (\nabla\boldsymbol{u})^{\mathrm{T}}\}$ and $\nabla\boldsymbol{u}$ are the shear strain rate tensor and the velocity gradient tensor, respectively, and ' : ' expresses a tensor product. Under this formulation, when the flow field is specified using a fixed velocity at the inlet boundary that is subject to a Dirichlet boundary condition, minimization of the dissipated power is equivalent to minimization of the pressure drop across the flow field [14, 51, 20].

2.4.4 Outflow rate constraint

In general fluidic device such as the microchannels, a flow rate that is evenly distributed among the channels is a design priority. To achieve an designated flow rate distribution among

the channels, constraint functional $G^n(\boldsymbol{u})$ of out flow rate ratio on the outlet boundaries Γ^n_{out} $(1 \leq n \leq N)$ can be defined as follows, using the out flow rate ratio r_n $(0 \leq r_n \leq 1)$ between the inflow rate Q_{in} and the flow rate at each of the outlets, under flow at a prescribed Reynolds number:

$$G^n(\boldsymbol{u}) = \left(\int_{\Gamma^n_{\text{out}}} \boldsymbol{n} \cdot \boldsymbol{u} \mathrm{d}\Gamma - r_n Q_{\text{in}} \right)^2 \leq \mathrm{R} \tag{2.19}$$

where $\boldsymbol{n}$ is the outward normal unit vector.

The error tolerance R in Eq (2.19) denotes the deviation in flow rate among the outlets. In this thesis, the error tolerance is set with $\mathrm{R} = 1.0 \times 10^{-4}$.

2.4.5 Sensitivity analysis

The optimization problem for minimizing the total potential energy under the outflow rate inequality constraint is now formulated as

$$\inf_{\phi} \quad J\left(\boldsymbol{u}, \chi_\phi\right) \tag{2.20}$$

$$\text{subject to} \quad G_1\left(\chi_\phi\right) \leq 0 \tag{2.21}$$

$$G_2^n(\boldsymbol{u}) \leq \mathrm{R}, \tag{2.22}$$

where the fluid velocity $\boldsymbol{u}$ satisfies the Navier-Stokes equation, Eq. (2.9), and continuity equation, Eq. (2.10), operating under the boundary conditions formulated in Eqs. (2.13)–(2.15). G_1 is the fluid volume constraint functional, with $G_1 = \int_{\Omega_{\text{d}}} \chi_\phi \mathrm{d}D - V_{\max}$, $V_{\max}$ representing the upper limit of the fluid region in the design domain, and G_2^n is the outflow rate constraint functional defined in Eq. (2.19).

Based on the Lagrange multiplier method, the Lagrangian $\mathcal{L}$ can be defined as

$$\mathcal{L} = J\left(\boldsymbol{u}, \chi_\phi\right) + \lambda_1 G_1\left(\chi_\phi\right) + \sum_{i=1}^{n} \lambda_2^i G_2^i(\boldsymbol{u}), \tag{2.23}$$

where λ_1 and λ_2^i $(i = 1, \cdots, n)$ are the Lagrange multipliers. We now assume that the level set function is sufficiently smooth. An optimal configuration candidate then satisfies the following KKT conditions:

$$\mathcal{L}' \geq 0, \quad \text{if } \phi = -1, \tag{2.24}$$

$$\mathcal{L}' = 0, \quad \text{if } -1 < \phi < 1, \tag{2.25}$$

$$\mathcal{L}' \leq 0, \quad \text{if } \phi = 1, \tag{2.26}$$

$$\lambda_1 G_1 = 0, \tag{2.27}$$

$$\lambda_1 \geq 0, \tag{2.28}$$

$$G_1 \leq 0, \tag{2.29}$$

$$\lambda_2^i G_2^i = 0, \tag{2.30}$$

$$\lambda_2^i \geq 0, \tag{2.31}$$

$$G_2^i \leq 0, \tag{2.32}$$

where $\mathcal{L}'$ represents the gradient of $\mathcal{L}$ with respect to the design variable.

A key component of topology optimization is the use of the adjoint variable method for derivation of the design sensitivity. To do this, we introduce an augmented objective functional $\bar{J}$, with

$$\bar{J} = J\left(\boldsymbol{u}, \chi_\phi\right) + A\left(\boldsymbol{u}, \tilde{\boldsymbol{u}}, p, \chi_\phi\right) + B(\boldsymbol{u}, \tilde{p}) + \lambda_1 G_1\left(\chi_\phi\right) + \sum_{i=1}^{n} \lambda_2^i G_2^i(\boldsymbol{u}), \tag{2.33}$$

where $\tilde{\boldsymbol{u}}$ and $\tilde{p}$ are arbitrary functions and the terms A and B represent the weak form of the Navier-Stokes equation, Eq. (2.9), and continuity equation, Eq. (2.10), respectively, described as bellow.

$$A := \int_D \left\{ (\boldsymbol{u} \cdot \nabla)\boldsymbol{u} + \nabla p - \frac{1}{\mathrm{Re}} \nabla^2 \boldsymbol{u} - \boldsymbol{f} \right\} \tilde{\boldsymbol{u}} \mathrm{d}D \tag{2.34}$$

$$B := -\int_D \nabla \cdot \boldsymbol{u} \tilde{p} \mathrm{d}D \tag{2.35}$$

where $(\boldsymbol{u}, p) \in \mathrm{U} \times \mathrm{P}$ and $(\tilde{\boldsymbol{u}}, \tilde{p}) \in \mathrm{U}_0 \times \mathrm{P}$ are defined as the functional space as bellow.

$$\mathrm{U} = \left\{ \tilde{\boldsymbol{u}} \in H^1(D) \,|\, \tilde{\boldsymbol{u}} = \boldsymbol{u}_{\mathrm{in}} \ \text{ on } \ \Gamma_{\mathrm{in}} \right\} \tag{2.36}$$

$$\mathrm{U}_0 = \left\{ \tilde{\boldsymbol{u}} \in H^1(D) \,|\, \tilde{\boldsymbol{u}} = 0 \ \text{ on } \ \Gamma_{\mathrm{in}} \right\} \tag{2.37}$$

$$\mathrm{P} = \left\{ \tilde{p} \in L^2(D) \,|\, \int_D \tilde{p} \mathrm{d}D = 0 \ \text{ in } \ D \right\} \tag{2.38}$$

where $H^1(D)$ and $L^2(D)$ are Sobolev and Lubegue space, respectively.

Next, the global variation of the state variables for the augmented objective functional is derived.

$$\begin{aligned}
\left\langle \frac{d\bar{J}_R}{d\phi}, \delta\phi \right\rangle = & \left\langle \frac{dJ_R}{d\phi}, \delta\phi \right\rangle + \left\langle \frac{dA}{d\phi}, \delta\phi \right\rangle + \left\langle \frac{dB}{d\phi}, \delta\phi \right\rangle + \lambda_1 \left\langle \frac{dG_1}{d\phi}, \delta\phi \right\rangle + \sum_{i=1}^{n} \lambda_2^i \left\langle \frac{dG_2^i}{d\phi}, \delta\phi \right\rangle \\
= & \left\langle \frac{\partial J_R}{\partial \boldsymbol{u}}, \delta\boldsymbol{u} \right\rangle + \left\langle \frac{\partial J_R}{\partial \phi}, \delta\phi \right\rangle + \left\langle \frac{\partial A}{\partial \boldsymbol{u}}, \delta\boldsymbol{u} \right\rangle + \left\langle \frac{\partial A}{\partial p}, \delta p \right\rangle + \left\langle \frac{\partial A}{\partial (\nabla \boldsymbol{u})}, \delta(\nabla \boldsymbol{u}) \right\rangle \\
& + \left\langle \frac{\partial A}{\partial \phi}, \delta\phi \right\rangle + \left\langle \frac{\partial B}{\partial \boldsymbol{u}}, \delta\boldsymbol{u} \right\rangle + \left\langle \frac{\partial B}{\partial \phi}, \delta\phi \right\rangle + \lambda_1 \left\langle \frac{\partial G_1}{\partial \phi}, \delta\phi \right\rangle + \sum_{i=1}^{n} \lambda_2^i \left\langle \frac{\partial G_2^i}{\partial \boldsymbol{u}}, \delta\boldsymbol{u} \right\rangle
\end{aligned} \tag{2.39}$$

where $\langle \cdot, \cdot \rangle$ denotes the Freche derivative. Here, the term including the derivative of flow velocity $\boldsymbol{u}$ and pressure p are vanished by solving the adjoint equations. By using the Gauss's divergence theorem and partial integration considering the boundary conditions, the above

equations can be transformed into,

$$
\begin{aligned}
&\left\langle \frac{\partial J_R}{\partial \boldsymbol{u}}, \delta \boldsymbol{u} \right\rangle + \left\langle \frac{\partial A}{\partial \boldsymbol{u}}, \delta \boldsymbol{u} \right\rangle + \left\langle \frac{\partial A}{\partial p}, \delta p \right\rangle + \left\langle \frac{\partial A}{\partial (\nabla \boldsymbol{u})}, \delta (\nabla \boldsymbol{u}) \right\rangle + \left\langle \frac{\partial B}{\partial \boldsymbol{u}}, \delta \boldsymbol{u} \right\rangle + \left\langle \frac{\partial B}{\partial \phi}, \delta \phi \right\rangle + \sum_{i=1}^{n} \lambda_2^i \left\langle \frac{\partial G_2^i}{\partial \boldsymbol{u}}, \delta \boldsymbol{u} \right\rangle \\
&= \int_D \left(\frac{1}{\mathrm{Re}} \nabla^2 \boldsymbol{u} + 2\alpha \boldsymbol{u} - \nabla \cdot \frac{2}{\mathrm{Re}} \nabla \boldsymbol{u} - \frac{1}{\mathrm{Re}} \nabla^2 \boldsymbol{v} - (\boldsymbol{u} \cdot \nabla) \boldsymbol{v} + (\nabla \boldsymbol{u}) \cdot \boldsymbol{v} + \alpha \boldsymbol{v} + \nabla q \right) \delta \boldsymbol{u} \mathrm{d}D \\
&+ \int_D (-\nabla \cdot \boldsymbol{v}) \delta p \mathrm{d}D \\
&+ \int_{\Gamma_\mathrm{N}} \left\{ \frac{2}{\mathrm{Re}} \nabla \boldsymbol{u} \cdot \boldsymbol{n} - q \cdot \boldsymbol{n} + \frac{1}{\mathrm{Re}} \nabla \boldsymbol{v} \cdot \boldsymbol{n} + (\boldsymbol{u} \cdot \boldsymbol{n}) \cdot \boldsymbol{v} + \sum_{i=1}^{n} \lambda_2^i \frac{2}{r_i Q_\mathrm{in}} \left(\frac{Q_\mathrm{out}^i}{r_i Q_\mathrm{in}} - 1 \right) \cdot \boldsymbol{n} \right\} \delta \boldsymbol{u} \mathrm{d}\Gamma \\
&+ \int_{\Gamma_\mathrm{D}} (\boldsymbol{v} \cdot \boldsymbol{n}) \delta p \mathrm{d}\Gamma
\end{aligned} \tag{2.40}
$$

where Γ_D and Γ_N are the Dirichlet and Neumann boundaries, respectively, and the outflow rate $\int_{\Gamma_\mathrm{out}^n} \boldsymbol{n} \cdot \boldsymbol{u} \mathrm{d}\Gamma$ on the boundary Γ_out^i is denoted as Q_out^i.

Here, the arbitrary Lagrange multipliers $\boldsymbol{v}$, q are obtained by solving the adjoint equations with the adjoint boundary conditions, which satisfy the integrand equally zero, as follows.

$$
-\frac{1}{\mathrm{Re}} \nabla^2 \boldsymbol{v} - (\boldsymbol{u} \cdot \nabla) \boldsymbol{v} + (\nabla \boldsymbol{u}) \cdot \boldsymbol{v} + \nabla q = -\alpha \boldsymbol{v} - \left(\frac{1}{\mathrm{Re}} \nabla^2 \boldsymbol{u} + 2\alpha \boldsymbol{u} - \nabla \cdot \frac{2}{\mathrm{Re}} \nabla \boldsymbol{u} \right) \quad \text{in} \quad D \tag{2.41}
$$

$$
-\nabla \cdot \boldsymbol{v} = 0 \quad \text{in} \quad D \tag{2.42}
$$

$$
\boldsymbol{v} = 0 \quad \text{on} \quad \Gamma_\mathrm{D} \tag{2.43}
$$

$$
\left(-q\boldsymbol{I} + \frac{1}{\mathrm{Re}} \nabla \boldsymbol{v} \right) \cdot \boldsymbol{n} = -(\boldsymbol{u} \cdot \boldsymbol{n}) \cdot \boldsymbol{v} - \frac{2}{\mathrm{Re}} \nabla \boldsymbol{u} \cdot \boldsymbol{n} - \sum_{i=1}^{n} \lambda_2^i \frac{2}{r_i Q_\mathrm{in}} \left(\frac{Q_\mathrm{out}^i}{r_i Q_\mathrm{in}} - 1 \right) \cdot \boldsymbol{n} \quad \text{on} \quad \Gamma_\mathrm{N}^i \tag{2.44}
$$

Consequently, the sensitivity can be derived as follows.

$$
\bar{J}' = (\alpha_\mathrm{min} - \alpha_\mathrm{max}) \left(|\boldsymbol{u}|^2 + \boldsymbol{v} \cdot \boldsymbol{u} \right) + \lambda_1. \tag{2.45}
$$

In Appendix A, the derivation of the adjoint equations are presented for general description of the objective functional in detail. Furthermore, the specific adjoint equations for several kind of the objective functionals are introduced in Appendix B.

2.4.6 Determination of the Lagrange multiplier corresponding to the flow rate inequality constraint

We note that the Lagrange multiplier, λ_2^n in Eq. (2.44), which is present due to the introduction of the flow rate inequality constraint, must be obtained beforehand in order to solve the adjoint equations.

To impose the flow rate inequality constraint, Liu et al. [44] employed an augmented Lagrangian method [34, 62] with a penalty function, but their approach requires an additional calculation to determine the Lagrange multiplier. Furthermore, in conventional augmented Lagrangian methods, the arbitrary coefficient setting of the penalty function may lead to numerical oscillations when the constraint functional value approaches the threshold between active or inactive conditions. In this thesis, we propose a simple method for determining the value of the Lagrange multiplier with respect to the flow rate inequality constraint, as described below.

As shown in Fig. 2.2, when the flow rate constraint Eq. (2.19) is inactive, $\lambda_2^n = 0$. On the other hand, when this constraint is active, λ_2^n is defined so that it assumes a value that depends on the relative error between the prescribed flow rate and the actual flow rate at each optimization iteration, by introducing a coefficient, C_1, in the following exponential function:

$$\lambda_2^n = C_1 \bar{\lambda}_2^n, \tag{2.46}$$

where C_1 and $\bar{\lambda}_2^n$ are defined, respectively, as

$$C_1 = \exp\left\{\left(\frac{Q_{\mathrm{e}}^n}{r_n Q_{\mathrm{in}}} - 1\right)^2 + a_n\right\}^{b_n} > 0, \tag{2.47}$$

$$\bar{\lambda}_2^n = \frac{\int_{\Gamma_{\mathrm{out}}^n} \left|\dfrac{\partial G_2^n}{\partial \boldsymbol{u}}\right| \mathrm{d}D}{\int_{\Gamma_{\mathrm{out}}^n} \mathrm{d}D} \geq 0, \tag{2.48}$$

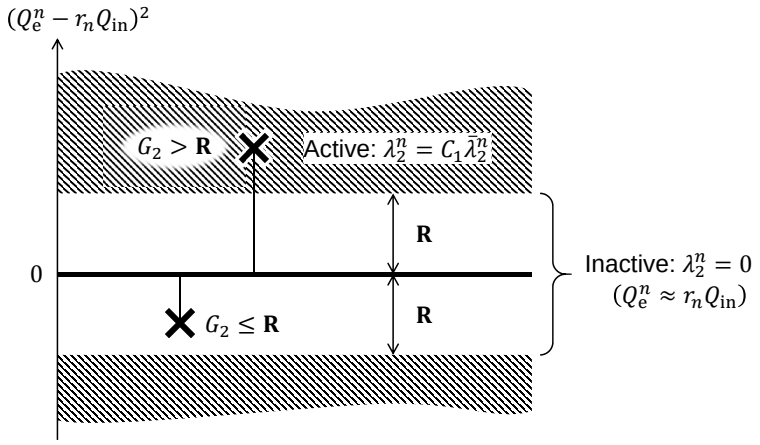

Fig. 2.2 Schematic diagram of the Lagrange multiplier λ_2^n.

where a_n and b_n are arbitrary parameters that influence the shape of the exponential function. Furthermore, because the obtained values of λ_2^n in Eq. (2.46) are always positive, our proposed method for determining λ_2^n is consistent with one of the KKT conditions in Eq. (2.31). Here, the values of arbitrary parameters a and b are set so that the order of the last term of the right-hand side in Eq. (2.44) is the same as that of the other terms, by estimating its approximate order using the initial result obtained by calculating the Navier-Stokes equations without the imposition of the flow rate inequality constraint. Therefore, when the flow rate inequality constraint is active, the last term of the right-hand side in Eq. (2.44) assumes a large absolute value.

From the standpoint of numerical stability, the introduction of the exponential function (Fig. 2.3) suppresses numerical oscillations, so that fluctuations in the value of lambda are sufficiently reduced, depending on the set values of a and b. When the relative error approaches a sufficiently small value, the value of coefficient C_1 becomes small, which provides numerical stability near the activity threshold of the flow rate inequality constraint.

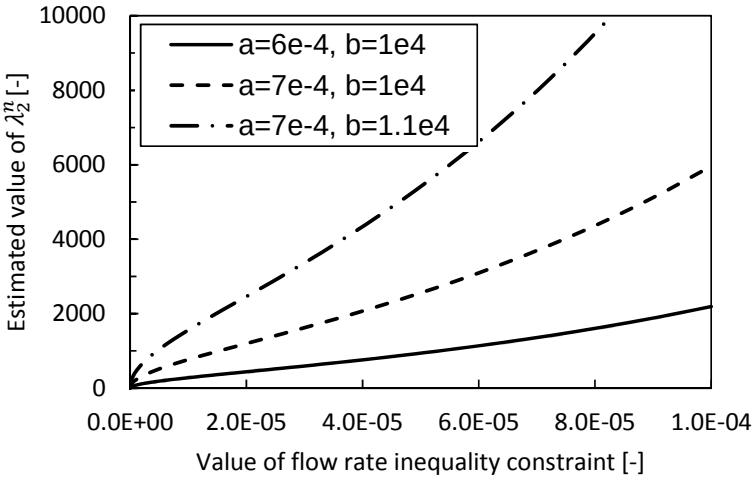

Fig. 2.3 Lagrange multiplier λ_2^n versus flow rate inequality constraint for different values of a and b.

2.4.7 Numerical implementation

Optimization algorithm

In practice, the characteristic function χ_ϕ is replaced with a smoothed Heaviside function, $\chi_\phi(\phi) \approx H(\phi)$, to improve the stability of the numerical computation, as follows:

$$H(\phi) = \begin{cases} 0 & (-1 \le \phi(\boldsymbol{x}) < w) \\ \left\{ \dfrac{1}{2} + \dfrac{\phi}{w}\left[\dfrac{15}{16} - \dfrac{\phi^2}{w^2}\left(\dfrac{5}{8} - \dfrac{3}{16}\dfrac{\phi^2}{w^2} \right) \right] \right\} & (-w \le \phi(\boldsymbol{x}) \le w) \\ 1 & (w < \phi(\boldsymbol{x}) \le 1), \end{cases} \tag{2.49}$$

where w represents a parameter used for setting the transition width of the smoothed Heaviside function.

Figure 2.4 shows the optimization algorithm applied in this study. The procedure is as follows.

(1) The initial distribution of the level set function is defined with $\phi = 1$ in the fixed design domain D, so that it is filled with fluid.

(2) The governing equations of the fluid problem are solved using FEM analysis and the distributions of velocity $\boldsymbol{u}$ and pressure p are obtained, as are the values of the objective functional J and constraint functionals G_1 and G_2.

(3) If the criteria of the objective and constraint functionals are satisfied, the optimization is finished and an optimal configuration is obtained; otherwise, the adjoint problem is solved.

(4) The design sensitivity is calculated using the solution of the governing equations and adjoint equations. The level set function is then updated by calculating the reaction diffusion equation, using FEM analysis, after calculating the design sensitivity.

In this thesis, the volume constraint and flow rate inequality constraints are checked at every iteration using Eq. (2.19), and if they are sufficiently converged, the following stopping criterion is evaluated. The optimization procedure is repeated until the value of objective functional satisfies this stopping criterion.

$$\left| \frac{J_{t+1} - J_t}{J_t} \right| < \epsilon, \tag{2.50}$$

where index t represents the time interval for iteration of the optimization procedure. We implement this criterion with $\epsilon = 1 \times 10^{-4}$.

Numerical method for the time evolution equation

First, the equation below can be obtained by discretizing Eq. (2.8) with respect to time.

$$\frac{\phi(t + \Delta t) - \phi(t)}{\Delta t} = -K\left(\bar{J}' - \tau \nabla^2 \phi(t + \Delta t)\right), \tag{2.51}$$

where Δt represents the time increment.

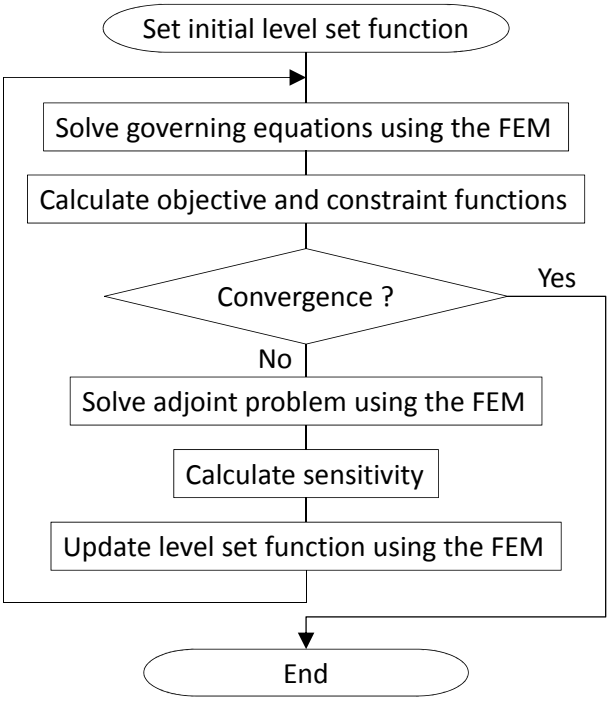

Fig. 2.4 Flowchart of the optimization procedure.

Next, the above equation is expressed in weak form as follows, to discretize the space prior to performing the FEM analysis.

$$\begin{aligned}&\int_D \frac{\phi(t+\Delta t)}{\Delta t}\tilde{\phi}\,\mathrm{d}D + \int_D \nabla^T \phi(t+\Delta t)\left(\tau K \nabla\tilde{\phi}\right)\mathrm{d}D \\ &\quad = \int_D \left(-K\phi(t)\,\bar{J}' + \frac{\phi(t)}{\Delta t}\right)\tilde{\phi}\,\mathrm{d}D \quad \text{for } \phi, \forall\tilde{\phi} \in \tilde{\Phi}\end{aligned} \tag{2.52}$$

The level set function $\phi(t+\Delta t)$ can be obtained by solving Eq. (2.52). $\tilde{\Phi}$ represents a functional space defined as

$$\tilde{\Phi} = \left\{\phi \in H^1(D) | \phi = 0 \ \text{ on } \partial D\right\}, \tag{2.53}$$

where ∂D is boundary where the Dirichlet boundary condition is applied.

Concerning the volume constraint G_1, the Lagrange multiplier λ_1 is set as zero when it is inactive, and when it is active, the following condition is satisfied,

$$\delta G_1 = 0. \tag{2.54}$$

By substituting Eq. (2.54) into Eq. (2.8), the Lagrange multiplier can be estimated as

$$\lambda_1 = -\frac{\int_D \left(\bar{J}' + \tau \nabla^2 \phi\right) dD}{\int_D dD}. \tag{2.55}$$

Here, the Lagrange multiplier λ_1 is updated using the following exponential function,

$$\bar{\lambda}_1 = \lambda_1 \exp(G_1). \tag{2.56}$$

2.5 Numerical examples

In this section, the proposed level set-based topology optimization method for the minimization of the total potential energy of steady-state incompressible viscous flow considering the outflow rate inequality constraint for an internal channel design problem is applied in two numerical examples. Throughout the following numerical examples, the flow distribution $\boldsymbol{u}_{\text{in}}$ at Γ_{in} is assumed to be a developed flow distribution in a channel within Cartesian coordinates $s \in [-L/2, L/2]$, as represented below.

$$\boldsymbol{u}_{\text{in}} \cdot \boldsymbol{n} = -\bar{g}\left\{1 - \left(\frac{2s}{L}\right)^2\right\}, \tag{2.57}$$

where $\bar{g}$ is the maximum magnitude of the velocity at the center of the flow inlet Γ_{in}, whose length is symbolically represented as L.

The fixed design domain is discretized with quadrilateral quadratic elements for $\boldsymbol{u}$ and $\boldsymbol{v}$, and quadrilateral linear elements for p and q. The initial distribution of ϕ is set as 1 for

the entire fixed design domain in all numerical examples, so that the fixed design domain is filled with fluid for the initial configuration in the optimization problems.

2.5.1 Example 1: two-terminal flow problem

In Example 1, we verify that the proposed outflow rate inequality constraint functions appropriately and the difference of the optimal channel design if outflow rate inequality constraint is applied or not.

Figure. 2.5 shows the design settings of two-terminal flow problem. The fixed design domain D has a flow inlet boundary Γ_{in} and two outlets boundaries Γ^1_{out} and Γ^2_{out}. The following parameters are set: regularization parameter $\tau = 5.0 \times 10^{-3}$, transition width of the approximate Heaviside function $w = 0.8$, the impermeability coefficient in the fluid $\alpha_{\min} = 0$ and solid domain $\alpha_{\max} = 1.0 \times 10^4$, and the upper limit of the fluid region $V_{\max} = 0.5 \int_\Omega \chi_\phi \, \mathrm{d}\Omega$. The maximum magnitude of the velocity at the center of the flow inlet is defined as $\bar{g} = 1.0$, and the flow field is defined as the laminar flow with the Reynolds number Re = 10 based on the characteristic flow velocity as the averaged inlet flow velocity and the characteristic length as the inlet boundary length. The number of elements of the fixed design domain D is $35 \times 25 = 875$.

Figure. 2.6 shows the optimal channel design without considering the outflow rate inequality constraint. In this numerical example, the objective functional is sum of the viscous energy dissipation of fluid and the power of resistance. Therefore, the flow resistance becomes small, when the length of interface between fluid and solid region is shorter and the channel configuration is rectilinear. Consequently, the rectilinear optimal channel configuration is obtained. In this numerical example, it seems that the channel is connected only to the outlet boundary Γ^1_{out} so as to decrease the flow resistance. From this result, it can be concluded that the flow channel configuration connected to both outlet boundaries Γ^1_{out} and Γ^2_{out} could not be obtained only considering the volume constraint G_1.

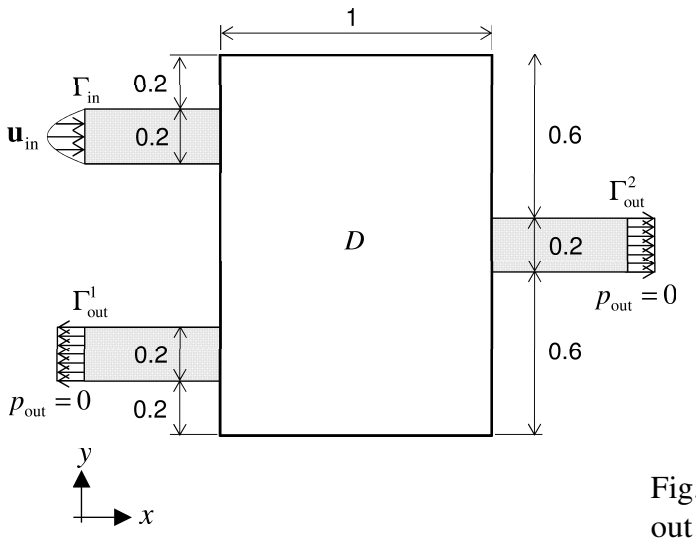

Fig. 2.5 Design settings of two-terminal flow problem

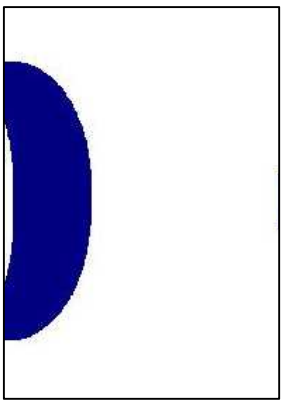

Fig. 2.6 Optimized flow channel layout (Re = 10) (blue, fluid domain; white, solid domain)

For the comparison, we address the optimization problem considering the outflow rate inequality condition G_2 on each outlet boundaries in addition to the fluid volume constraint G_1. Firstly, the optimal channel configuration under the prescribed outflow rate $r_1 = 0.3$ in Re = 10 is shown in Fig. 2.7. The parameters are set as $(a_{1,2}, b_{1,2}) = (0.3, 0.8)$. As shown in Fig. 2.7, the optimal channel is connected from the inlet boundary to both outlet boundaries owing to the outflow rate inequality constraint G_2. The convergence histories of the optimization calculation is shown in Fig. 2.8. While the outflow rate greatly changed at the early stage of the optimization with the drastic changing of the objective functional, both of the outflow rate and the objective functional sufficiently converged and the outflow rate satisfied the specific outflow rate constraint at the end of the optimization steps. The variety of the optimal channel configuration under the prescribed outflow rate $r_1 = 0.4, 0.5, 0.6, 0.7$ are shown in Fig. 2.9 Additionally, the value of the outflow rate on each outlet boundaries Q^n_{out}, the volume constraint functional G_1, the residual R_1 of the outflow rate constraint on the outlet boundary Γ^1_{out} and the objective functional J are indicated in Table 2.1 for every outflow rate inequality conditions. The following parameters are set: $(a_{1,2}, b_{1,2}) = (0.1, 2.0)$ for

$r_1 = 0.4$, $(a_{1,2}, b_{1,2}) = (0.3, 5.0)$ for $r_1 = 0.5$, $(a_{1,2}, b_{1,2}) = (0.1, 2.0)$ for $r_1 = 0.6$, and $(a_1, b_1) = (0.2, 5.0)$ and $(a_2, b_2) = (0.2, 8.0)$ for $r_1 = 0.7$. As shown in Fig. 2.9, different optimal channel configurations which have specific channel width connecting to the outlet boundaries could be obtained depending on the prescribed outflow rate r_1 settings. Furthermore, the length of interface between fluid and solid regions of the optimal configurations of $r_1 = 0.3, 0.7$ are shorter compared with the other optimal configurations. This is also confirmed that the value of the objective functional of $r_1 = 0.3, 0.7$ are small compared with that of $r_1 = 0.4, 0.5, 0.6$.

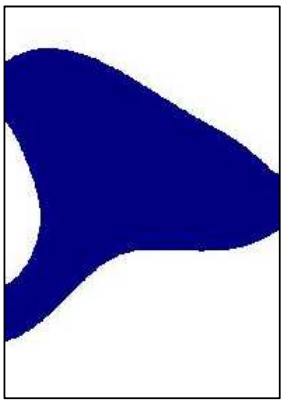

Fig. 2.7 Optimized flow channel layout (r_1=0.3, Re = 10) (blue, fluid domain; white, solid domain)

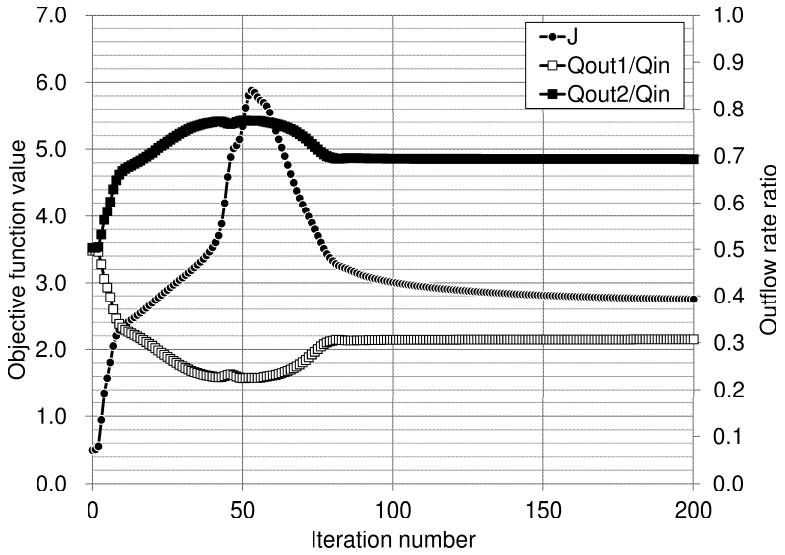

Fig. 2.8 Convergence histories of the objective function value (J) and the actual outflow rates relative to inflow rate on each outlet boundaries Γ^1_{out} and Γ^2_{out} ($Q^1_{\text{out}}/Q_{\text{in}}$, $Q^2_{\text{out}}/Q_{\text{in}}$)

Table 2.1 Computational results of two-terminal flow

r_1	Q^1_{out}	Q^2_{out}	G_1	R_1	J
0.3	0.31	0.69	0.42	4.5×10^{-4}	2.75
0.4	0.41	0.59	0.26	7.3×10^{-4}	3.88
0.5	0.51	0.49	0.26	1.4×10^{-4}	3.81
0.6	0.61	0.39	0.25	3.5×10^{-4}	4.04
0.7	0.68	0.32	0.36	1.2×10^{-3}	3.10

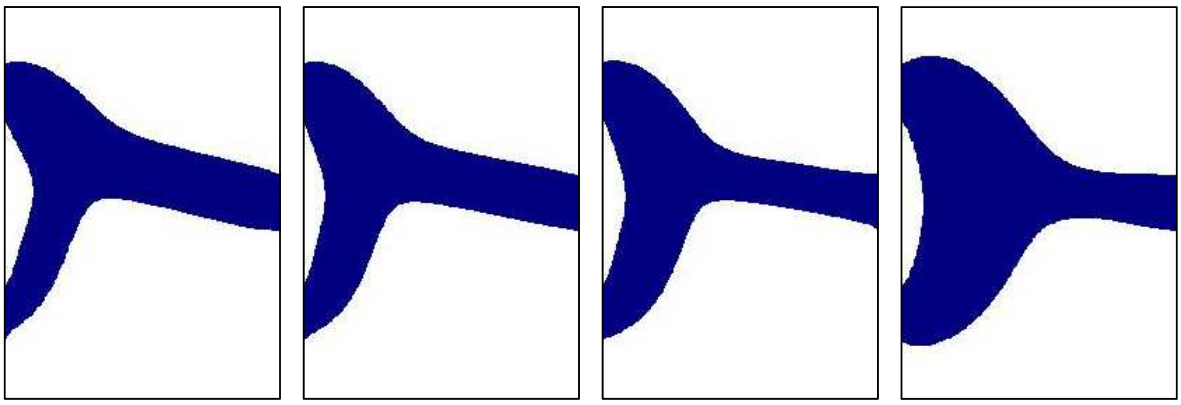

r_1 =0.4 r_1 =0.5 r_1 =0.6 r_1 =0.7

Fig. 2.9 Comparison of optimized flow channel layouts (Re = 10) (blue, fluid domain; white, solid domain)

2.5.2 Example 2: multi-terminal flow problem

In Example 2, the fixed design domain which has three inlet and outlet boundaries are addressed for the topology optimization problem as the multi-terminal flow problem. This means that the flow comes from the three inlet boundaries Γ_{in}^n $(n = 1,2,3)$ and separately exit to the three outlet boundaries Γ_{out}^n.

In this numerical example, the following parameters are set: the maximum magnitude of the velocity u_{in}^n at the center of every flow inlet boundaries $\bar{g}_n = 1.0\,(\text{Re} = 10)$, regularization parameter $\tau = 1.0\times10^{-5}$, transition width of the approximate Heaviside function $w = 0.4$, the impermeability coefficient in the fluid $\alpha_{\min} = 0$ and solid domain $\alpha_{\max} = 1.0\times10^{4}$, and the upper limit of the fluid region $V_{\max} = 0.7\int_\Omega \chi_\phi \,\mathrm{d}\Omega$. The number of elements of the fixed design domain D is $58\times60 = 3480$.

Firstly of all, the optimization problem in which the flow exits equally to the three outlet boundaries is addressed as an equally prescribed outflow rate condition ($r_n = 1/3$). The parameters are set as $(a_{1,2,3}, b_{1,2,3}) = (0.3, 4.0)$. Figure. 2.11 shows the optimal channel configuration. As shown in Figs. 2.11 and 2.12, the optimal configuration has the three separated flow channels and each flow channels are connected to the nearest outlet boundaries.

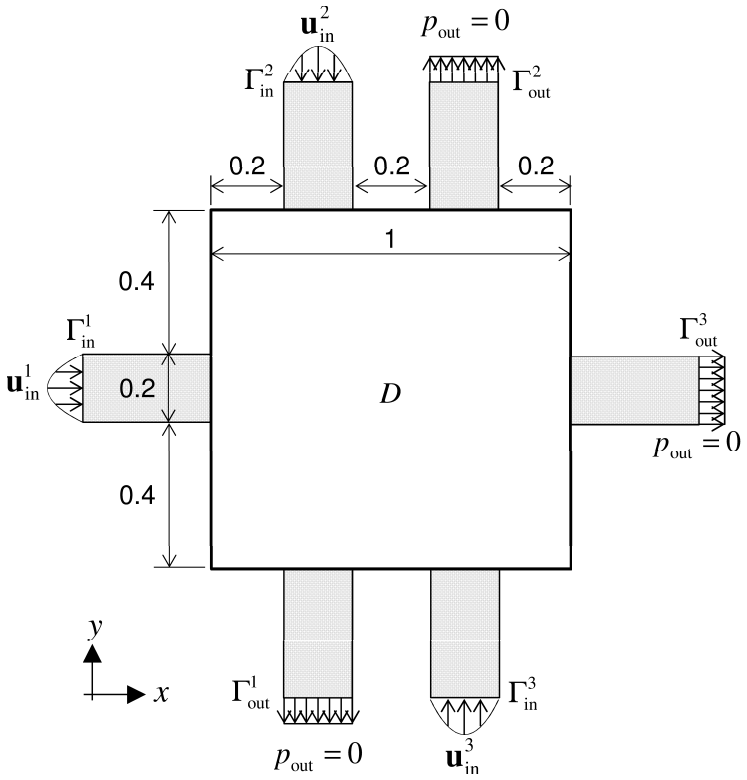

Fig. 2.10 Design settings of multi-terminal flow problem

Next, the optimization problem with the outflow rate $r_1 = 0.6$, $r_2 = 0.2$ and $r_3 = 0.2$ is addressed. The parameters are set as $(a_1, b_1) = (-3.0, 15.5)$, $(a_2, b_2) = (2.5, 0.2)$, $(a_3, b_3) = (7.0, 0.1)$. From the result of the optimization as shown in Figs. 2.13 and 2.14, the flow coming from the inlet boundaries Γ_{in}^2 and Γ_{in}^3 exits not only to the outlet boundaries Γ_{out}^2 and Γ_{out}^3 respectively, but also separates and exits to the outlet boundary Γ_{out}^1. From the Table. 2.2, it is confirmed that the prescribed outflow rate can be obtained in the optimal channel configuration with sufficiently small residual R_n between every outflow rates Q_{out}^n and the prescribed outflow rates on each outlet boundaries.

Consequently, the validity of our proposed outflow rate constraint can be confirmed for the multi-terminal flow problem.

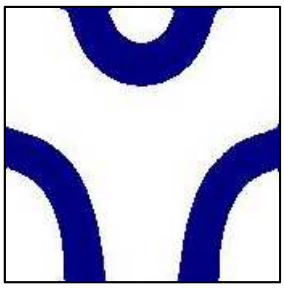

Fig. 2.11 Optimized flow channel layout ($r_1 = r_2 = r_3 = 1/3$) (blue, fluid domain; white, solid domain)

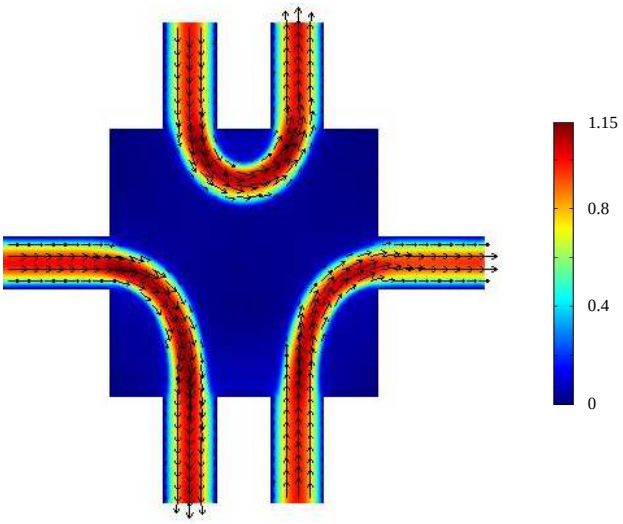

Fig. 2.12 Velocity contour distribution and velocity vector in optimized flow channel ($r_1 = r_2 = r_3 = 1/3$)

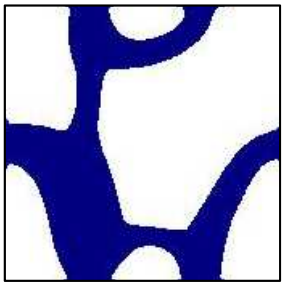

Fig. 2.13 Optimized flow channel layout ($r_1 = 0.6$, $r_2 = 0.2$, $r_3 = 0.2$) (blue, fluid domain; white, solid domain)

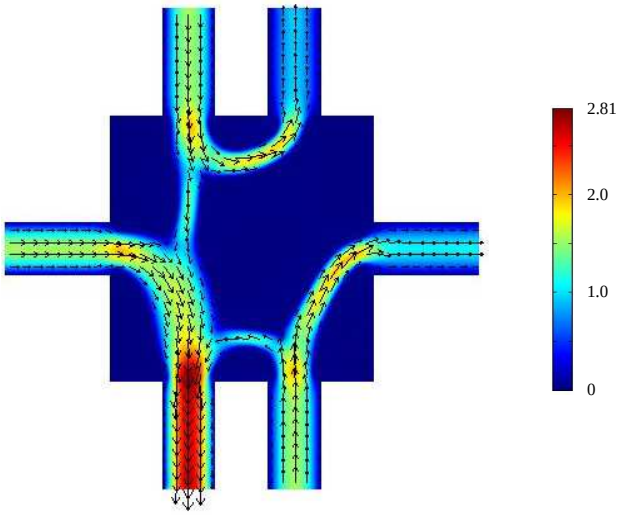

Fig. 2.14 Velocity contour distribution and velocity vector in optimized flow channel ($r_1 = 0.6$, $r_2 = 0.2$, $r_3 = 0.2$)

Table 2.2 Residual of outflow rate on each outlet boundaries in optimal configuration

R_1	R_2	R_3
2.21×10^{-3}	9.32×10^{-7}	2.02×10^{-2}

2.6 Summary

This Chapter proposed a level set-based topology optimization method considering the out flow rate inequality constraints for the design of the MEMS scale multi-terminal fluidic devices. The following results were obtained.

- Topology optimization method to an optimal design problem for a steady state incompressible viscous flow was conducted and the channel layout design optimization problem was formulated to minimize the total potential energy of fluids considering the out flow rate inequality constraint.
- A numerically stable and simple way to determine the Lagrange multiplier concerning the out flow rate inequality constraint was proposed. Following this method, the appropriate value of the Lagrange multiplier can be obtained depending on the residual between prescribed and actual out flow rate in outlets.
- Based on the adjoint variable method, sensitivity analysis for the proposed optimization problem was conducted considering the outflow rate inequality constraint.
- The validity of our proposed method was revealed in two numerical examples. Designated outflow rate in each outlets of the multi-terminal channel flows can be obtained using our proposed optimization method.

Chapter 3

Optimal manifold designs with flow uniformity in plate-type microchannel reactors

3.1 Introduction

Flow properties crucially influence the efficiency of reactions and heat exchange in most microscale and nanoscale devices incorporating microchannels, such as microreactors, microchannel heat sinks, and micromixers. In these devices, the overall flow passage is composed of a distributed array of microchannel passages whose combined flow is manifested as the throughput of the microfluidic device. In contrast to a single serpentine channel, the small volumes within such an array achieve a higher surface-to-volume ratio that provides improved reaction efficiency and heat exchange, with high heat and mass transfer rates occurring on the microchannel wall surfaces. During the past few decades, owing to progress in microfabrication techniques, this concept of flow passage design is actively utilized in the design of micro chemical plants for applications such as polymer processing and artificial biological systems.

Although several types of microfluidic devices have been proposed to realize high throughput, in principle, the flow through an array of microchannels may result in higher velocity flow in particular microchannels, which causes a large drop in pressure over the entire microfluidic device. This undesirable pressure drop, and the associated uneven flow distribution between the individual microchannels, negatively affects chemical conversion rates or the selection functions of the device. Additionally, an uneven flow distribution in a microchannel array may cause unacceptable pressure loss for the device, compared with flow distributions that are more even, although not perfectly even. Furthermore, a catalyst is often applied to the interior surface of the microchannels in microreactors, to accelerate chemical reactions that occur as liquids flow through the microchannels. In this scenario, the efficiency of the reaction rate is highly dependent on the residence time of the flow in the microchannels, and the amount of catalyst employed is determined based on this residence time, under the assumption of an equal flow rate distribution in the microchannels. Consequently, an uneven flow distribution in the microchannels reduces the efficiency of the reaction rate. Therefore, optimal designs of distributed microchannels that achieve an even flow distribution with minimal pressure losses are generally important for microchannel reactors, as a foundation for additional design objectives that aim to maximize actual reaction rates.

Flow distributions in microchannels have been studied using a variety of approaches. Concerning an analytical approach, Bajura [8] first proposed a general theoretical model for investigating the performance of single-phase flow distribution for both an intake and exhaust manifold, and extended this to include flow rates and pressure changes in Z-type and U-type manifold configurations [9]. Bassiouny and Martin [10, 11] developed an analytical method for predicting the flow and pressure distribution in U-type and Z-type heat exchangers, although the effect of wall friction in the flow headers was ignored.

On the other hand, a numerical approach can be used to examine the performance of different manifold or microchannel array geometries, to improve flow uniformity and

minimize the pressure drop in devices. Mohammadi et al. [49] investigated the flow uniformity and pressure distribution of a microchannel reactor with triangular manifolds, using computational fluid dynamics (CFD) in low Reynolds number regimes ($5 \leq \mathrm{Re} \leq 25$). They found that the structural parameters of a given manifold shape greatly influence the velocity distribution in the microchannel array. That is, there is an optimum shape that results in the most uniform flow distribution among the microchannels. They clarified that the designer must allow for some degree of nonuniformity in the flow in the manifold design, based on the intended application of the device, because there is no universal threshold value for velocity deviations within the microchannel array.

For the design of highly efficient configurations of fluidic devices, a numerical approach using structural optimization is considered most useful for exploring the most promising designs among a number of design candidates. Tonomura et al. [74] used size optimization to achieve flow uniformity among microchannels in a plate-fin microdevice. They optimized the outlet manifold shape to minimize its area and the variances of flow rate in a five-microchannel array for Re = 50, 250, and 500. In their approach, a multi-objective functional was defined using the weighted sum method. Consequently, because an appropriate weighting parameter value could not be defined beforehand, it had to be determined by comparing several optimization results obtained using different parameter values, to achieve an optimal design that had an acceptable degree of nonuniformity in the flow rate among the microchannels. A different approach for shape optimization of a microchannel manifold was presented by Pan et al. [55]. Their analytical model, and an equivalent electrical resistance model, were applied to analytically estimate the pressure drop, flow rate, and flow resistance in a microchannel manifold. Moreover, the variables in their shape optimization were expressed with two monotonic equations that defined the outline shapes of the inlet and outlet manifolds. Their results led them to conclude that the width of the individual microchannels is the dominant factor affecting the geometry of the outlet manifold. In any

case, the studies based on the optimization methods by Tonomura et al. [74] and Pan et al. [55] can be categorized as size and shape optimizations, respectively. These methods used in the above research may not always provide high performance configurations, due to the relatively small number of design variables and parameter settings employed.

In this Chapter, we propose an optimal design method for plate-type microchannel reactor manifolds. Based on the out flow rate inequality constraints constructed in Chapter 2, furthermore, we implement a flow rate inequality constraint, which constrains the flow rate deviation in each target microchannel to achieve an acceptable degree of flow uniformity.

Firstly, we introduce the basic geometry of the plate-type microchannel reactor and presents the representative Z-type and U-type manifolds that are the design objects in this thesis. Next, we formulate the topology optimization problem for minimizing the total potential energy under a flow rate inequality constraint, using a level set boundary expression, for a steady-state incompressible viscous flow field. Based on this formulation, the design sensitivity is derived using the adjoint variable method. Furthermore, the simple way to determine the Lagrange multiplier for the flow rate inequality constraint is presented. We then construct an optimization algorithm for the manifold design problems. Finally, we present design problems for Z-type and U-type manifolds for a five-microchannel reactor device, and verify the utility of the proposed optimization method through these numerical examples.

3.2 Microchannel manifold geometry

3.2.1 Plate-type manifolds

Here, we present an optimal design method applied to the inlet and outlet manifolds of a plate-type microchannel reactor that achieves specified design requirements. A representative plate-type microchannel array with inlet and outlet manifolds is shown in Fig. 3.1.

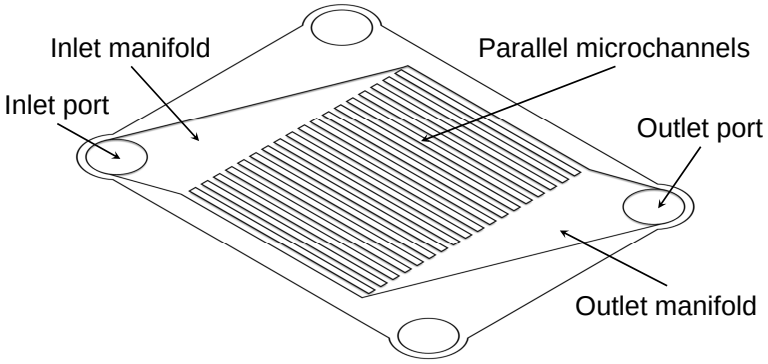

Fig. 3.1 Schematic view of microchannel array with plate-type manifolds.

The manifolds include an inlet or outlet port, the manifold area, and the connection to the array of parallel microchannels that constitute the main part of the reactor. The use of an array of parallel microchannels helps to satisfy reaction requirements that could not be achieved with a single microchannel. The basic microchannel reactor device is usually stacked in a group of 50 or more units, to maximize production throughput. To minimize the volume of grouped microchannel reactors, each reactor and its plate-type manifolds must be very thin. The reactors under investigation are thin enough that a laminar flow can be assumed, and two-dimensional numerical analysis of the flow in these manifolds is assumed to be valid. The validity of these assumptions is supported in past research concerning laminar flow regimes ($0.006 \leq \mathrm{Re} \leq 300$) [49]. In our study, we focus on the laminar flow regime in the numerical simulation of fluid flow, and the numerical study uses a two-dimensional model.

3.2.2 Classification of manifold geometry

The manifolds here can be categorized into two geometrical types, based on the directions of the inlet and outlet flows [49, 32]. As shown in Fig. 3.2(a), in the Z-type manifold, the inlet and outlet flows proceed in the same direction, whereas in the U-type manifold illustrated in

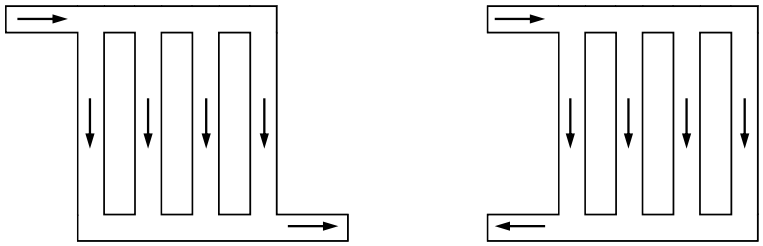

(a) Z-type (b) U-type

Fig. 3.2 Schematic flow configuration of the two manifold types.

Fig. 3.2(b), the flow is bidirectional, with the direction of the outlet flow opposite that of the inlet flow. In this study, the optimization approach is applied to both manifold types.

3.3 Formulation

3.3.1 Governing equations

We consider the two representative types of manifold described in Chap. 3.2.2, the Z- and U-type. Because the degree of uniformity in the flow of liquid within the microchannels significantly influences the reaction efficiency, we aim to ensure a sufficient degree of uniformity, i.e., to minimize deviation in the flow among the individual microchannels. The chemical reaction in the microchannels is a time-dependent phenomenon, since catalyst applied to the surface walls of the parallel microchannels is consumed during the reaction. Since the fluid that reacts with the catalyst flows steadily through the microchannels when the microreactor is operating, no flow control is applied. Therefore, we consider that flow uniformity is to be achieved with the fluid in a steady-state condition, and we assume that the fluid behavior is time-independent during the optimizations in the manifold design problems. Additionally, for simplification, reaction phenomena are not considered, since the degree of uniformity in the microchannels ensures sufficiently high reaction efficiency. Based on the above considerations, we assume a laminar flow and steady-state for the fluid, which is

described by the steady-state incompressible Navier-Stokes and continuity equations in Eqs (2.9) and (2.10). Corresponding to the boundary conditions for the microchannel reactor, generally, the flow rate through the reactor is specified so that the residence time in the microchannels can be adjusted to a designated time that achieves the desired high throughput. In the optimization problem, we define the prescribed flow velocity at inlet boundary Γ_{in} in Eq. (2.13), without loss of generality, and impose the Neumann boundary condition at outlet boundary Γ_{out} in Eq. (2.14). The boundary condition for the microchannel walls, Γ_{wall}, is defined as a no-slip condition in Eq. (2.15).

3.3.2 Definition of the objective functional

The topology optimization is considered within the fixed design domain D, in which the manifold shapes can be deformed freely, and which also includes the fluid domain Ω and the solid domain $D\backslash\Omega$. A schematic diagram of the design domain settings is shown in Fig. 3.3. As shown in Fig. 3.3, the design domain is defined as the area of the inlet and outlet manifolds, while the areas of the parallel microchannels are set as non-design domains. To obtain high reaction efficiency, the residence time of the fluid in the microchannels is estimated in advance so that the catalyst will be fully consumed during the reaction. The residence time is greatly affected by the geometry of the microchannels, but the geometrical complexity of a parallel microchannel design is constrained by requirements for easy manufacturability. Typical microchannel arrays incorporate a number of straight microchannels that have a square cross-section because this simple geometry is particularly economical for mass manufacturing [73]. This preference for geometrical simplicity, and the prevalence of parallel microchannel designs employing square cross-section microchannels, is why we set the areas of the microchannels as non-design domains in this study.

The throughput of a microchannel reactor is affected by the pressure drop between the inlet and the outlet, and by the uniformity of flow among the microchannels. Our proposed

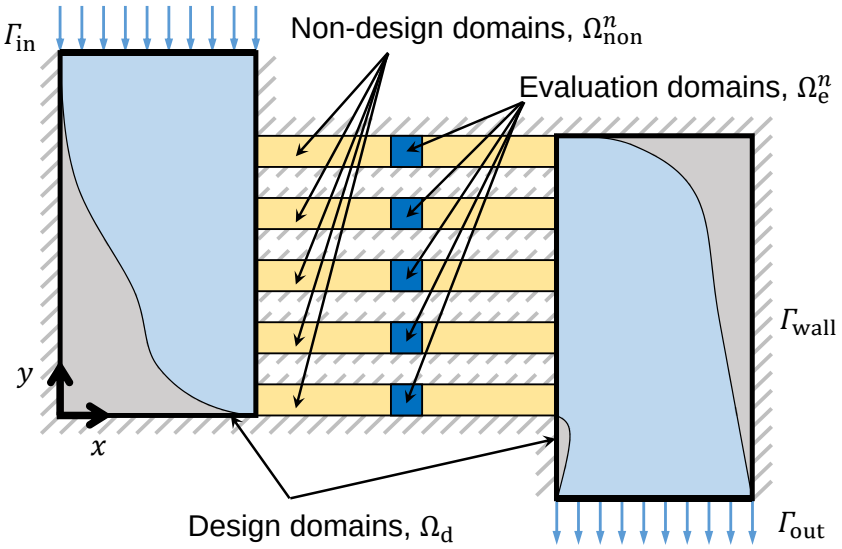

Fig. 3.3 Fixed design domain settings for the optimization problem of the manifold. The two large rectangular areas represent design domains, and the microchannels themselves are set as non-design domains. The fixed design domain D is composed of the sum of the design domains Ω^n_{d} and non-design domains Ω^n_{non}, while the evaluation domains Ω^n_{e} are dominated in Ω_{non} ($(\Omega_{\text{d}} \cup \Omega_{\text{non}}) \subseteq D$, and $\Omega_{\text{e}} \subset \Omega_{\text{non}}$).

topology optimization method aims to obtain manifold designs that achieve both a minimal pressure drop and a high degree of flow uniformity. These requirements can be accomplished using a multi-objective optimization method such as the weighted sum method, but the value of the weighting parameter that will achieve sufficient flow uniformity cannot be determined in advance. Therefore, a number of optimization calculations are typically carried out, using different values of the weighting parameter, to determine the most appropriate value. To overcome this time-consuming approach, we define the pressure drop between the inlet and outlet of a microchannel reactor as an objective functional, and obtain good flow uniformity by implementing a constraint functional in the optimization problem, details of which are provided in Sec. 3.3.3.

Objective functional J in this study represents the total potential energy of the fluid in the device, defined as the sum of the dissipated power and the work done by an external force in Eq. (2.18).

3.3.3 Introduction of flow rate inequality constraint

For both the Z-type and U-type manifolds in this research, a flow rate that is evenly distributed among the microchannels is a design priority. To achieve an even flow rate distribution among the five microchannels that are integrated with the Z-type or U-type manifold, constraint functional P^n ($n = 1,2,3,4,5$) is defined as follows, using the ratio r_n ($0 \leq r_n \leq 1$) between the inflow rate Q_{in} and the flow rate at each of the microchannels, under flow at a prescribed Reynolds number:

$$P^n(\boldsymbol{u}) = \left(\frac{\int_{\Omega_e^n} \boldsymbol{i} \cdot \boldsymbol{u} \, \mathrm{d}D}{r_n Q_{\text{in}}} - 1 \right)^2 \leq \mathrm{R}, \tag{3.1}$$

where $\boldsymbol{i} = (1,0)$ is the x-directional unit vector in an evaluation domain in each of the Ω_e^n domains shown in Fig. 3.3, and R is the prescribed error tolerance. We note that, although the number of microchannels, n, is set as five in this study, an arbitrary value of n is valid in the following discussion.

In this study, an evaluation domain is used to ascertain the flow rate in the interior of each microchannel, defined as a square domain located at the center of each microchannel (Fig. 3.3). The error tolerance R in (3.1) denotes the deviation in flow rate among the microchannels. Generally, an acceptable value for flow rate deviation depends on the type of catalyst used, since, ideally, the catalyst should be completely consumed in the catalyzed reaction that occurs in the microchannels during the designated residence time. In this research, the error tolerance is set with $\mathrm{R} = 1.0 \times 10^{-4}$.

3.3.4 Manifold design optimization problem

The optimization problem for a manifold under the flow rate inequality constraint is now formulated as

$$\inf_{\phi} \quad J\left(\boldsymbol{u},\chi_\phi\right) \tag{3.2}$$

$$\text{subject to} \quad G\left(\chi_\phi\right) \leq 0 \tag{3.3}$$

$$P^n\left(\boldsymbol{u}\right) \leq \mathrm{R}\,, \tag{3.4}$$

where the fluid velocity $\boldsymbol{u}$ satisfies the Navier-Stokes equation (2.9) and continuity equation (2.10), operating under the boundary conditions formulated in Eqs. (2.13)–(2.15). G is the fluid volume constraint functional, with $G = \int_{\Omega_\mathrm{d}} \chi_\phi \,\mathrm{d}D - V_{\max}$, $V_{\max}$ representing the upper limit of the fluid region in the design domain, and P^n is the flow rate constraint functional defined in (3.1). Based on the Lagrange multiplier method, the Lagrangian $\mathcal{L}$ can be defined as

$$\mathcal{L} = J\left(\boldsymbol{u},\chi_\phi\right) + \lambda_1 G\left(\chi_\phi\right) + \sum_{i=1}^{n} \lambda_2^i P^i\left(\boldsymbol{u}\right), \tag{3.5}$$

where λ_1 and λ_2^i $(i = 1,\cdots,n)$ are the Lagrange multipliers. We now assume that the level set function is sufficiently smooth. An optimal configuration candidate then satisfies the

following Karush-Kuhn-Tucker (KKT) conditions:

$$\mathcal{L}' \geq 0, \quad \text{if } \phi = -1, \tag{3.6}$$

$$\mathcal{L}' = 0, \quad \text{if } -1 < \phi < 1, \tag{3.7}$$

$$\mathcal{L}' \leq 0, \quad \text{if } \phi = 1, \tag{3.8}$$

$$\lambda_1 G = 0, \tag{3.9}$$

$$\lambda_1 \geq 0, \tag{3.10}$$

$$G \leq 0, \tag{3.11}$$

$$\lambda_2^i P^i = 0, \tag{3.12}$$

$$\lambda_2^i \geq 0, \tag{3.13}$$

$$P^i \leq 0, \tag{3.14}$$

where $\mathcal{L}'$ represents the gradient of $\mathcal{L}$ with respect to the design variable.

3.3.5 Sensitivity analysis based on the adjoint variable method

A key component of topology optimization is the use of the adjoint variable method for derivation of the design sensitivity. To do this, we introduce an augmented objective functional $\bar{J}$, with

$$\bar{J} = J\left(\boldsymbol{u}, \chi_\phi\right) + A\left(\boldsymbol{u}, \tilde{\boldsymbol{u}}, p, \chi_\phi\right) + B(\boldsymbol{u}, \tilde{p}) + \lambda_1 G\left(\chi_\phi\right) + \sum_{i=1}^{n} \lambda_2^i P^i(\boldsymbol{u}), \tag{3.15}$$

where $\tilde{\boldsymbol{u}}$ and $\tilde{p}$ are arbitrary functions and the terms A and B represent the weak form of the Navier-Stokes equation (2.9) and continuity equation (2.10), respectively.

Next, the global variation of the state variables for the augmented objective functional is derived. A detailed development of the continuous response using the adjoint variable method can be found in Zhou and Li [83] and Duan et al. [24]. In our present study, from

a mathematical point of view, the development is practically identical, the only difference being our inclusion of the derivatives of the flow rate inequality constraint. Consequently, the strong form of the adjoint equations and boundary conditions can be derived including the terms resulting from the derivatives of the flow rate inequality constraint, as follows:

$$
\begin{aligned}
&-\frac{1}{\mathrm{Re}}\nabla^2\boldsymbol{v}-(\boldsymbol{u}\cdot\nabla)\boldsymbol{v}+(\nabla\boldsymbol{u})\cdot\boldsymbol{v}+\nabla q+\alpha\boldsymbol{v}\\
&\quad=\frac{2}{\mathrm{Re}}\nabla^2\boldsymbol{u}-2\alpha\boldsymbol{u}-\sum_{i=1}^{n}\xi\lambda_2^i\frac{2}{r_iQ_{\mathrm{in}}}\left(\frac{Q_{\mathrm{e}}^i}{r_iQ_{\mathrm{in}}}-1\right)\cdot\boldsymbol{i}
\end{aligned}
\tag{3.16}
$$

$$
-\nabla\cdot\boldsymbol{v}=0 \tag{3.17}
$$

$$
\boldsymbol{v}=\boldsymbol{0}\ \text{ on }\Gamma_{\mathrm{D}} \tag{3.18}
$$

$$
\left(-q\boldsymbol{I}+\frac{1}{\mathrm{Re}}\nabla\boldsymbol{v}\right)\cdot\boldsymbol{n}+(\boldsymbol{u}\cdot\boldsymbol{n})\cdot\boldsymbol{v}=-\frac{2}{\mathrm{Re}}\nabla\boldsymbol{u}\cdot\boldsymbol{n}\ \text{ on }\Gamma_{\mathrm{N}}, \tag{3.19}
$$

where the adjoint variables are denoted as $\boldsymbol{v}$ and q and the flow rate at Ω_{e}^i, namely $\int_{\Omega_{\mathrm{e}}^i}\boldsymbol{i}\cdot\boldsymbol{u}\,\mathrm{d}D$, is denoted by Q_{e}^i. The parameter constant ξ is equal to 0 in $D\setminus\Omega_{\mathrm{e}}^i$ and 1 in Ω_{e}^i, while $\Gamma_{\mathrm{N}}=\Gamma_{\mathrm{out}}$ and $\Gamma_{\mathrm{D}}=\Gamma_{\mathrm{in}}\cup\Gamma_{\mathrm{wall}}$. λ_2^i denotes the Lagrange multiplier that applies in Ω_{e}^i. The adjoint equations of the optimization problem under steady-state incompressible viscous flow are expressed in (3.16) and (3.17), and they satisfy the adjoint boundary conditions expressed in (3.18) and (3.19) that impose Dirichlet and Neumann boundary conditions on Γ_{D} and Γ_{N}, respectively. Consequently, the design sensitivity of the augmented objective functional $\bar{J}'$ is given by

$$
\bar{J}'=(\alpha_{\min}-\alpha_{\max})\left(|\boldsymbol{u}|^2+\boldsymbol{v}\cdot\boldsymbol{u}\right)+\lambda_1. \tag{3.20}
$$

We note that, although the term corresponding to a flow rate inequality constraint is not explicitly included in (3.20), the design sensitivity distribution will vary depending on whether or not a flow rate inequality constraint is applied. That is, the adjoint velocity $\boldsymbol{v}$ affects the design sensitivity distribution, which differs depending on whether or not the flow

rate inequality constraint is applied in the optimization problem. This is because adjoint velocity $\boldsymbol{v}$ is obtained by solving the adjoint equations in the fixed design domain D, which is the sum of design domains Ω_{d}^n and non-design domains Ω_{non}^n. Therefore, the obtained value of $\boldsymbol{v}$ implicitly includes the effect of the flow rate inequality constraint, which is applied at $\Omega_{\mathrm{e}}^n \subset \Omega_{\mathrm{non}}^n$ (Eq. (3.16), with $\xi = 1$).

3.4 Determination of the Lagrange multiplier corresponding to the flow rate inequality constraint

We note that the Lagrange multiplier, λ_2^n in (3.16), which is present due to the introduction of the flow rate inequality constraint, must be obtained beforehand in order to solve the adjoint equations.

To impose the flow rate inequality constraint, Liu et al. [44] employed an augmented Lagrangian method [34, 62] with a penalty function, but their approach requires an additional calculation to determine the Lagrange multiplier. Furthermore, in conventional augmented Lagrangian methods, the arbitrary coefficient setting of the penalty function may lead to numerical oscillations when the constraint functional value approaches the threshold between active or inactive conditions. In this study, we propose a simple method for determining the value of the Lagrange multiplier with respect to the flow rate inequality constraint, as described below.

As shown in Fig.2.2, when the flow rate constraint (3.1) is inactive, $\lambda_2^n = 0$. On the other hand, when this constraint is active, λ_2^n is defined so that it assumes a value that depends on the relative error between the prescribed flow rate and the actual flow rate at each optimization iteration, by introducing a coefficient, C_1, in the following exponential function:

$$\lambda_2^n = C_1 \bar{\lambda}_2^n, \tag{3.21}$$

where C_1 and $\bar{\lambda}_2^n$ are defined, respectively, as

$$C_1 = \exp\left\{\left(\frac{Q_{\mathrm{e}}^n}{r_n Q_{\mathrm{in}}} - 1\right)^2 + a_n\right\}^{b_n} > 0, \tag{3.22}$$

$$\bar{\lambda}_2^n = \frac{\int_{\Omega_{\mathrm{e}}^n} \left|\dfrac{\partial P^n}{\partial \boldsymbol{u}}\right| \mathrm{d}D}{\int_{\Omega_{\mathrm{e}}^n} \mathrm{d}D} \geq 0, \tag{3.23}$$

Furthermore, because the obtained values of λ_2^n in (3.21) are always positive, our proposed method for determining λ_2^n is consistent with one of the KKT conditions in (3.13). Here, the values of arbitrary parameters a and b are set so that the order of the last term of the right-hand side in (3.16) is the same as that of the other terms, by estimating its approximate order using the initial result obtained by calculating the Navier-Stokes equations without the imposition of the flow rate inequality constraint. Therefore, when the flow rate inequality constraint is active, the last term of the right-hand side in (3.16) assumes a large absolute value in the evaluation domains Ω_{e}^n located at the centers of the microchannels. Consequently, a manifold shape can be created by fostering or inhibiting flow at the interior domains Ω_{e}^n, depending on the relative error from the prescribed flow rate at these domains.

From the standpoint of numerical stability, the introduction of the exponential function (Fig. 2.3) suppresses numerical oscillations, so that fluctuations in the value of lambda are sufficiently reduced, depending on the set values of a and b. When the relative error approaches a sufficiently small value, the value of coefficient C_1 becomes small, which provides numerical stability near the activity threshold of the flow rate inequality constraint.

3.5 Numerical implementation

3.5.1 Optimization algorithm

The optimization algorithm applied in this study follows the optimization procedure described below.

(1) The initial distribution of the level set function is defined with $\phi = 1$ in the fixed design domain D, so that it is filled with fluid.

(2) The governing equations of the fluid problem are solved using FEM analysis and the distributions of velocity $\boldsymbol{u}$ and pressure p are obtained, as are the values of the objective functional J and constraint functionals G and P.

(3) If the criteria of the objective and constraint functionals are satisfied, the optimization is finished and an optimal configuration is obtained; otherwise, the adjoint problem is solved.

(4) The design sensitivity is calculated using the solution of the governing equations and adjoint equations. The level set function is then updated by calculating the reaction diffusion equation, using FEM analysis, after calculating the design sensitivity.

In this study, the volume constraint and flow rate inequality constraints are checked at every iteration using (2.19), and if they are sufficiently converged, the following stopping criterion is evaluated. The optimization procedure is repeated until the value of objective functional satisfies this stopping criterion.

$$\left| \frac{J_{t+1} - J_t}{J_t} \right| < \epsilon, \tag{3.24}$$

where index t represents the time interval for iteration of the optimization procedure. We implement this criterion with $\epsilon = 1 \times 10^{-4}$.

3.6 Numerical examples

In this section, we present numerical examples of the topology optimization problems for Z-type and U-type manifolds. To verify that the proposed optimization method functions appropriately, we examine two-dimensional total potential energy minimization problems for steady-state incompressible viscous flow. Throughout the following numerical examples, the flow distribution $\boldsymbol{u}_{\mathrm{in}}$ at Γ_{in} is assumed to be a developed flow distribution in a channel within Cartesian coordinates $s \in [-L/2, L/2]$, as represented below.

$$\boldsymbol{u}_{\mathrm{in}} \cdot \boldsymbol{n} = -\bar{g}\left\{1 - \left(\frac{2s}{L}\right)^2\right\}, \tag{3.25}$$

where $\bar{g}$ is the maximum magnitude of the velocity at the center of the flow inlet Γ_{in}, whose length is symbolically represented as L.

The fixed design domain D is discretized with quadrilateral quadratic elements for $\boldsymbol{u}$ and $\boldsymbol{v}$, and quadrilateral linear elements for p and q. The initial distribution of ϕ is set as 1 for the entire fixed design domain in all numerical examples, so that the fixed design domain is filled with fluid for the initial configuration in the optimization problems.

3.6.1 Topology optimization of Z-type manifold

The design settings for the Z-type manifold optimization problem are shown in Fig. 3.4. The design domain Ω_{d} includes the areas of the inlet and outlet manifolds. The area of the microchannel array is treated as a non-design domain Ω_{non} because the shape of the microchannel array is specified and must remain constant, to preserve the accuracy of the estimated residence time of the fluid undergoing the catalyzed reaction in the microchannels. The five microchannels are numbered in order from No. 1, which is farthest from the inlet, to No. 5, which is nearest the inlet (Fig. 3.4). In the fixed design domain, the inlet and outlet boundaries are denoted Γ_{in} and Γ_{out}, respectively. The following parameters are set:

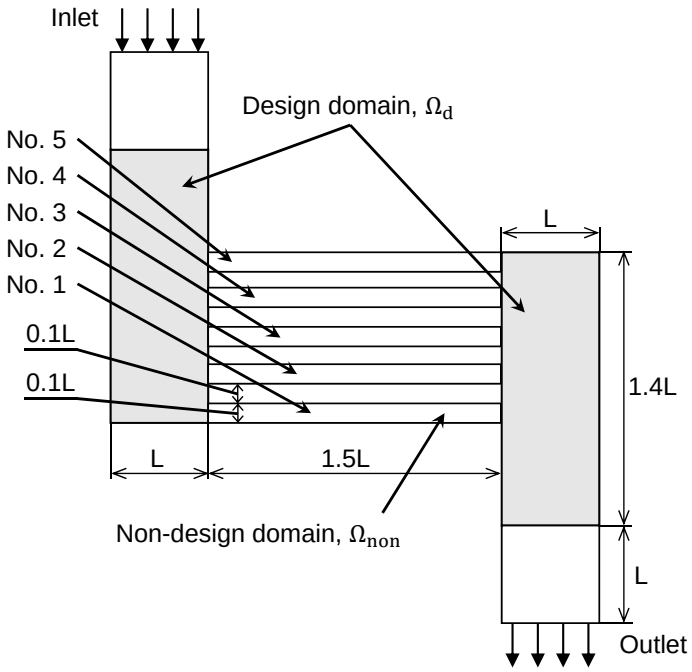

Fig. 3.4 Design settings for Z-type manifold optimization problem.

regularization parameter $\tau = 1.0 \times 10^{-4}$, and transition width of the approximate Heaviside function $w = 1.0 \times 10^{-3}$. The number of elements of the design domain is 10000.

Optimization without a flow rate inequality constraint

First, only the fluid volume constraint functional G is considered in the optimization. The Reynolds number Re is set to four different values: 10, 100, 250, and 500.

Figure 3.5 illustrates the flow rate distribution among the five microchannels of the initial Z-type manifold for the four cases using different Reynolds numbers, and we see that the unevenness of the flow distribution across the array of microchannels increases as the Reynolds number is increased. In particular, when Re = 10, the lowest setting, the deviation in flow rate between the first and fifth microchannels is relatively small compared with that between the other microchannels. On the other hand, when Re $\geq$ 100, the flow rate of the third microchannel, located at the center of the array, generally has the smallest deviation, but the flow rate deviation for the other microchannels becomes larger for microchannels located

further away from the center, and this tendency is exacerbated as the Reynolds number is increased. This tendency, in which the nonuniformity of the flow among the microchannels is affected by the Reynolds number, is in agreement with previous observations [74, 49]

Figure 3.6 shows optimal configurations obtained for the four cases using different Re values, with the flow passage domains illustrated in dark blue. The upper limit of the fluid region in all cases is set so that $V_{\max}/V_{\mathrm{d}} = 0.9$, while $V_{\mathrm{d}} := \int_{\Omega_{\mathrm{d}}} \mathrm{d}D$ represents the volume of the design domain. The objective functional values for the results shown in (a), (b), (c), and (d) of Fig. 3.6 are provided in Table 3.1. The value of the objective functional decreases as the Reynolds number is increased. We note that, in general, the total potential energy becomes higher as the Reynolds number is increased. The opposite tendency seen in the optimization results, in which the value of the objective functional decreases as the Reynolds number is increased, is caused by the formulation of the objective functional in (2.18), where the Reynolds number is expressed as a reciprocal. These optimal configurations indicate that the different Re values applied in the optimizations affect the profiles of the inlet and outlet manifolds. As Re is increased, the inlet manifold shape becomes narrower toward the bottom, near the microchannels farthest from the inlet, and the shape of the outlet manifold becomes correspondingly wider in this area.

The flow rate distributions for the five microchannels operating with the different Z-shape manifold optimal configurations are illustrated in Fig. 3.7. In the contrast to the initial design in which the fluid is fulfilled, the tendency of the deviation of the flow rate in each microchannels is different in the optimal design. For the different Reynolds numbers applied, the deviation in flow at the outer microchannel of the optimal design becomes smaller than that of the initial design, with the growth of the deviation at the second to fourth microchannels near by the central in array.

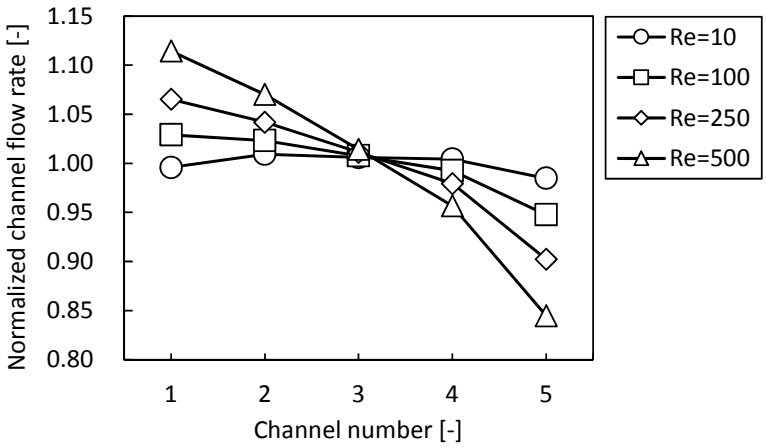

Fig. 3.5 Flow rate distribution among microchannels for initial design of Z-type manifold under four different Reynolds numbers. Normalized channel flow rate is defined as $Q_{\mathrm{e}}^{n}/(r_n Q_{\mathrm{in}})$, where Q_{e}^{n} and $r_n Q_{\mathrm{in}}$ are the actual and target flow rates in microchannel No. n, respectively.

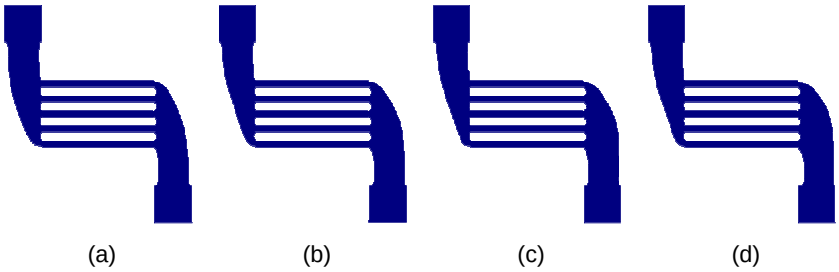

Fig. 3.6 Optimal flow configurations of Z-type manifold without flow rate inequality constraint (volume constraint: $V_{\max}/V_{\mathrm{d}} = 0.9$ in all cases: (a) Re = 10; (b) Re = 100; (c) Re = 250; (d) Re = 500).

Table 3.1 Objective functional values of the Z-type manifold optimal configurations for four different Reynolds numbers.

Re	10	100	250	500
J	17.9	2.3	1.1	0.7

Optimization with a flow rate inequality constraint

Next, we consider an optimization problem that includes flow rate inequality constraint P in addition to the fluid volume constraint G. Figure 3.8 shows a comparison of the optimal

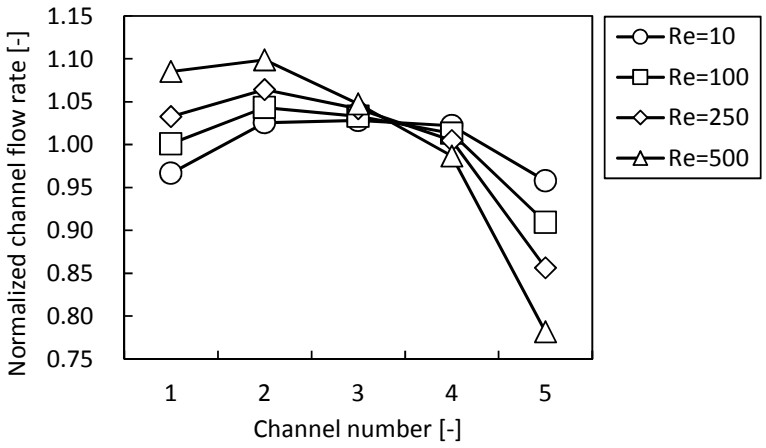

Fig. 3.7 Flow rate distribution among microchannels for four different Reynolds numbers using optimal designs of Z-type manifold obtained without a flow rate inequality constraint. Normalized channel flow rate is defined as $Q_{\mathrm{e}}^{n}/(r_n Q_{\mathrm{in}})$, where Q_{e}^{n} and $r_n Q_{\mathrm{in}}$ are the actual and target flow rates in microchannel No. n, respectively.

configurations obtained for Re = 10 and Re = 100 with the flow rate inequality constraint applied, and not applied. In both optimizations with the flow rate inequality constraint applied, the ratio of the flow rate Q_{e}^{n} with respect to the inflow rate Q_{in} was fixed, with $r_n = 0.2$ in Ω_{e}^{n} (which means that the fluid must be uniformly distributed to each microchannel). The parameters were set as follows for two cases: $(a_n, b_n) = (7.0\times10^{-4}, 1.0\times10^{4})$; the prescribed error tolerance R = 1.0×10^{-4}, and $V_{\max}/V_{\mathrm{d}} = 0.9$.

As Fig. 3.8 illustrates, at first glance, the basic outlines of the inlet and outlet manifolds appear quite similar, regardless of whether or not the flow rate inequality constraint is applied. However, the detailed shapes where the inlet and outlet manifolds join each microchannel, shown in the magnified portions of Fig. 3.8, show notable corresponding differences, with and without the use of the flow rate inequality constraint. Specifically, the shapes where the inlet and outlet manifolds meet each microchannel are essentially symmetrical and round in the optimal configurations obtained without a flow rate inequality constraint, but when a flow rate inequality constraint is included in the optimization, these shapes become asymmetric between the inlet and outlet manifolds, and reveal individual features depending on which

Table 3.2 Tolerance values for the flow rate inequality constraint in Ω_e in Z-type manifold optimal configurations.

Tolerance	R_1	R_2	R_3	R_4	R_5
Re = 10	2.3×10^{-5}	1.3×10^{-5}	1.4×10^{-5}	1.1×10^{-5}	3.4×10^{-5}
Re = 100	7.5×10^{-6}	1.5×10^{-5}	3.0×10^{-6}	1.7×10^{-6}	9.3×10^{-5}

microchannel they are joined to. We surmise that the asymmetry in these shapes beneficially affects the pressure distribution in the inlet and outlet manifold areas so that an even flow rate distribution among the microchannels is favored.

Figures 3.9 and 3.10 provide graphical comparisons of the flow rate distributions among the five microchannels for the initial configuration and the results obtained with and without a flow rate inequality constraint, for Re = 10 and Re = 100, respectively. The use of the flow rate inequality constraint in the optimization dramatically reduces the flow rate deviation among the microchannels for both Re values. Moreover, the error tolerance values set for the flow rate inequality constraint in inner domain Ω_e^n, denoted R_n in Table 3.2 and applied in the optimizations with Re = 10 and Re = 100, remain within the prescribed tolerances in these two cases.

Furthermore, as shown in Fig. 3.11, while the actual error tolerance of the flow rate inequality constraint P oscillates during the initial 100 iterations, sufficient convergence, below $P < 1.0\times10^{-4}$, is obtained later on. As shown in the convergence history of the objective functional for the case where Re = 10 (Fig. 3.12), the value of the objective functional changes greatly during the early optimization steps, due to rapid alterations in the level set function distribution, but the objective functional is sufficiently converged after approximately 600 iterations. This allows us to confirm that the proposed flow rate inequality constraint works as intended.

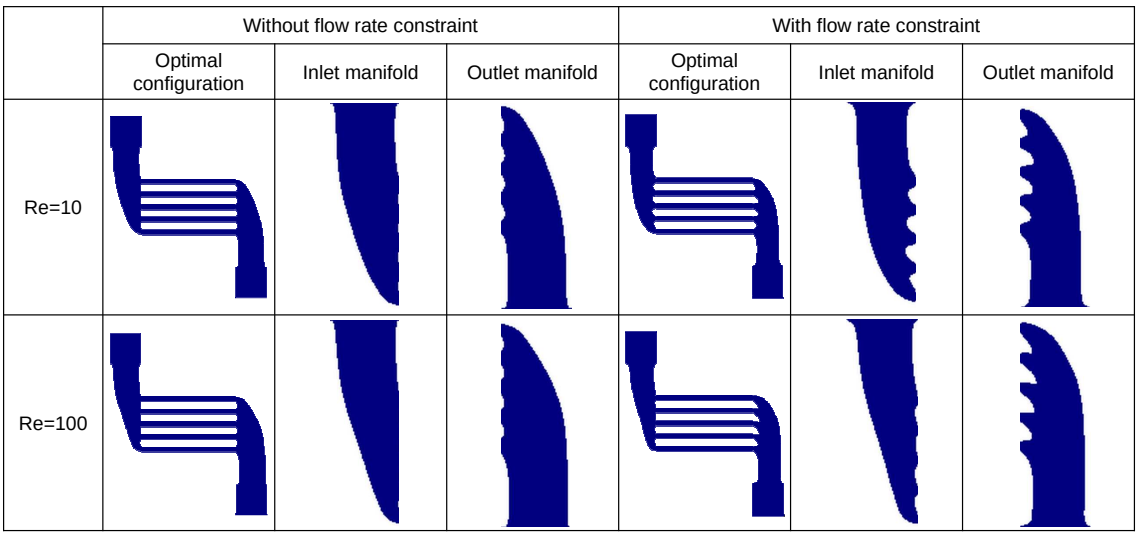

Fig. 3.8 Optimal flow configurations of Z-type manifold with and without flow rate inequality constraint and Re = 10 and 100.

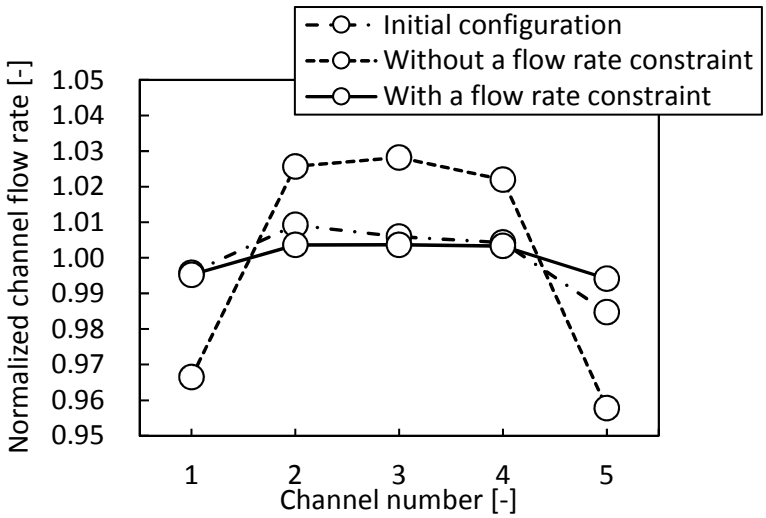

Fig. 3.9 Flow rate distributions among microchannels for Z-type manifold optimal configurations with Re = 10. Normalized channel flow rate is defined as $Q_{\mathrm{e}}^{n}/(r_n Q_{\mathrm{in}})$, where Q_{e}^{n} and $r_n Q_{\mathrm{in}}$ are the actual and target flow rates in microchannel No. n, respectively.

As described in [49], the design engineer must define an acceptable degree of nonuniformity among the microchannels depending on the device's design priority, for example, minimization of the pressure drop, or maximization of the flow uniformity among the microchannels. Based on the dissipated power values we obtained, which can be regarded as the

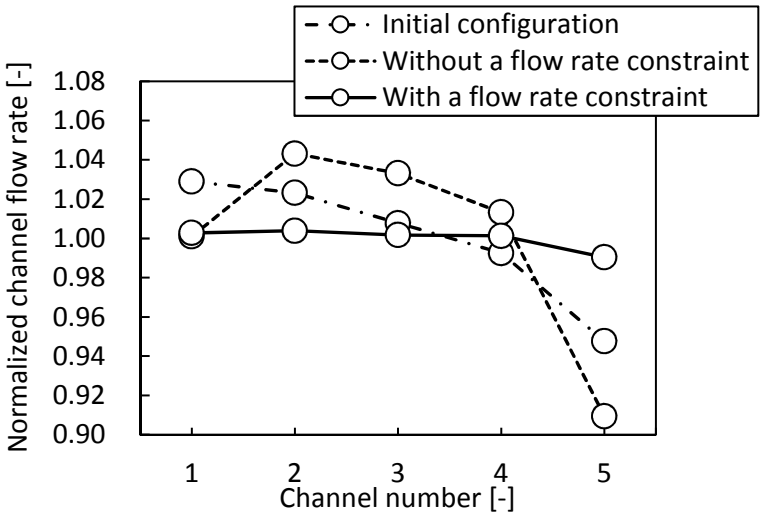

Fig. 3.10 Flow rate distributions among microchannels for Z-type manifold optimal configurations with Re = 100. Normalized channel flow rate is defined as $Q_{\mathrm{e}}^{n}/(r_n Q_{\mathrm{in}})$, where Q_{e}^{n} and $r_n Q_{\mathrm{in}}$ are the actual and target flow rates in microchannel No. n, respectively.

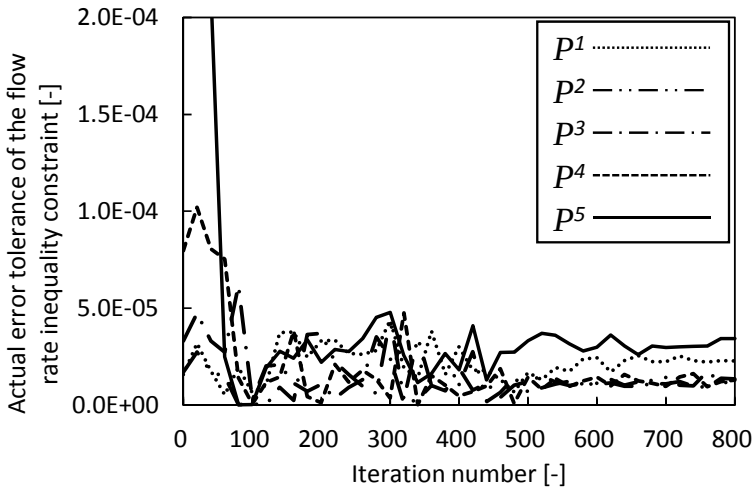

Fig. 3.11 Actual error tolerance in flow rate inequality constraint for Z-type manifold microchannels when Re = 10.

pressure drop in these optimization problems, we also find that some degree of pressure drop must be accepted to achieve the desired degree of flow uniformity. This can be appreciated by comparing the results of optimizations with and without a flow rate inequality constraint applied (Table. 3.3). Our results indicate that there is a trade-off relationship between pressure drop and flow uniformity. In previous optimization methods using a multi-objective

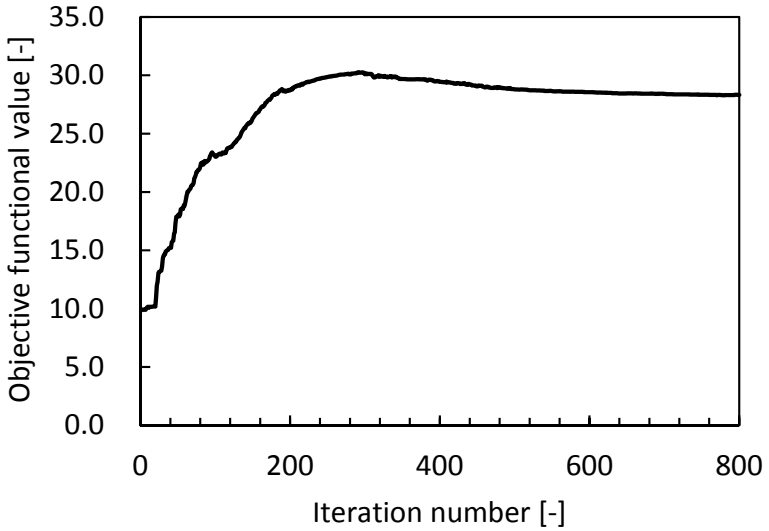

Fig. 3.12 Convergence history of objective functional for Z-type manifold when Re = 10.

Table 3.3 The dissipated power values for Z-type manifold optimizations. *P* represents the flow rate inequality constraint.

Re	Initial design	Optimal design without *P*	Optimal design with *P*
10	10.9	17.9	28.3
100	1.5	2.3	4.1

functional, this trade-off relationship inhibits obtaining inlet and outlet manifold designs that have acceptable flow uniformity unless a number of optimization results are compared ([74]). The optimization method proposed here, however, can obtain optimal designs that have minimal pressure drop and excellent uniformity of flow across the microchannel array, without using trial and error calculations.

3.6.2 Topology optimization of U-type manifold

In this section, we apply the proposed method to the U-type manifold optimization problem diagrammed in Fig. 3.13. The design domain Ω_d again only includes the areas of the inlet and outlet manifolds; the area occupied by the microchannel array is treated as a non-design

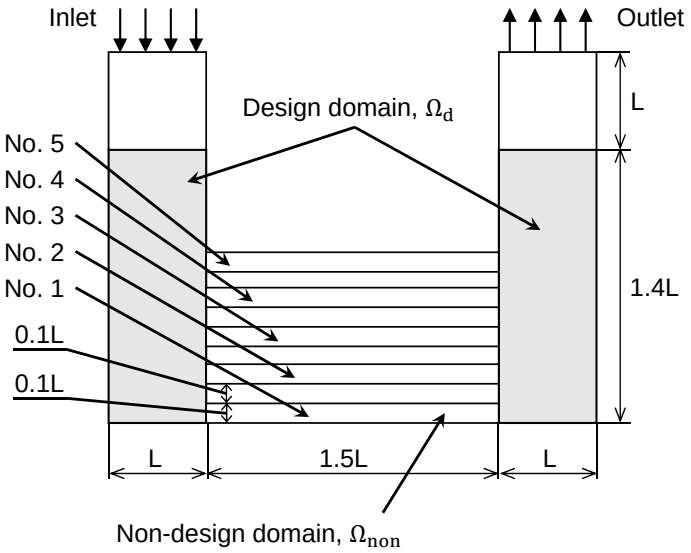

Fig. 3.13 Design settings for U-type manifold optimization problem.

domain, just as for the optimization problem described in Sec. 3.6.1. The five microchannels are numbered from No. 1, the farthest from the inlet, to No. 5 nearest the inlet (Fig. 3.13). In the fixed design domain, the inlet and outlet boundaries are denoted Γ_{in} and Γ_{out}, respectively. The flow rate is prescribed as $r_n = 0.2$ in Ω_{e}^n to ensure an equal flow distribution among all microchannels and the parameters are set as follows: $\tau = 1.0 \times 10^{-4}$; $w = 1.0 \times 10^{-3}$; and $V_{\max}/V_{\text{d}} = 0.9$. The number of elements of the design domain is 6060.

Figure 3.14 shows the two optimal configurations obtained without applying a flow rate inequality constraint; optimal configurations that reflect the use of a flow rate inequality constraint are shown in Fig. 3.15 and Fig. 3.16 for Re = 10 and Re = 100, respectively. In this optimization problem, the parameters are set so that $(a_n, b_n) = (8.0 \times 10^{-3}, 8.0 \times 10^{2})$ for Re = 10 and $(a_n, b_n) = (6.0 \times 10^{-3}, 8.0 \times 10^{2})$ for Re = 100. Based on the results shown in Figs. 3.14, 3.15, and 3.16, the outlines of the inlet and outlet manifold appear essentially the same regardless of whether a flow rate inequality constraint is applied in the optimization or not. On the other hand, these optimal configurations reveal distinct differences in the shape of the inlet and outlet areas adjoining the microchannels. In the U-type manifold design problem, these differences are especially noticeable in the outlet manifolds when a flow rate

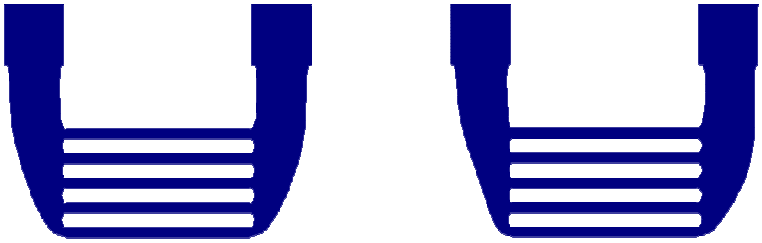

(a) (b)

Fig. 3.14 Optimal flow configurations of U-type manifolds without a flow rate inequality constraint (volume constraint $V_{\max}/V_{\mathrm{d}} = 0.9$ in both cases: (a) Re = 10; (b) Re = 100).

inequality constraint is active, where the areas closest to the microchannel outlets appear steeply inclined and horn-shaped, in contrast to the same areas in the optimization results without a flow rate inequality constraint, which are uniform and unremarkable.

Figures 3.17 and 3.18 illustrate flow rate distributions among the microchannels for the initial configuration and results with and without the flow rate inequality constraint, for Re = 10 and Re = 100, respectively. The results here mirror those for the Z-type manifold discussed in Sec. 3.6.1, in that flow rate deviations among the microchannels in the U-type manifold under Re = 10 and Re = 100 are reduced in both optimal configurations when the flow rate inequality constraint is applied. The data provided in Table 3.4 indicate that the error tolerance values for the flow rate inequality constraint are sufficiently small in both the Re = 10 and Re = 100 cases. Moreover, the dissipated power values obtained in the optimization problems and listed in Table 3.5 indicate that there is also a trade-off relationship between pressure drop and flow uniformity for the U-type manifold, the same as for the Z-type manifold discussed in Sec. 3.6.1. However, the proposed optimization method obtains appropriate designs for the U-type inlet and outlet manifolds of the microchannel reactor, so that excellent flow uniformity among the microchannels and minimal pressure drop are achieved.

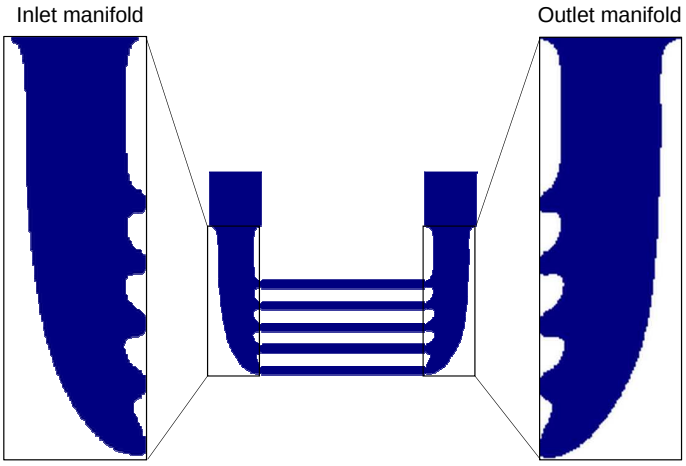

Fig. 3.15 Optimal flow configuration of U-type manifold with a flow rate inequality constraint and Re = 10.

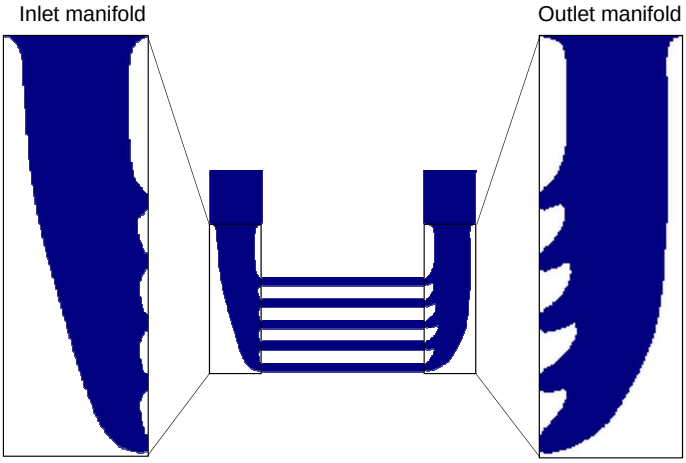

Fig. 3.16 Optimal flow configuration of U-type manifold with a flow rate inequality constraint and Re = 100.

Table 3.4 Tolerance values for the flow rate inequality constraint in Ω_e in U-type manifold optimal configurations.

$R_n(\times 10^{-4})$	R_1	R_2	R_3	R_4	R_5
Re = 10	2.6×10^{-4}	1.8×10^{-5}	2.1×10^{-5}	3.2×10^{-5}	1.0×10^{-4}
Re = 100	1.2×10^{-4}	3.5×10^{-7}	6.0×10^{-6}	1.4×10^{-5}	2.9×10^{-5}

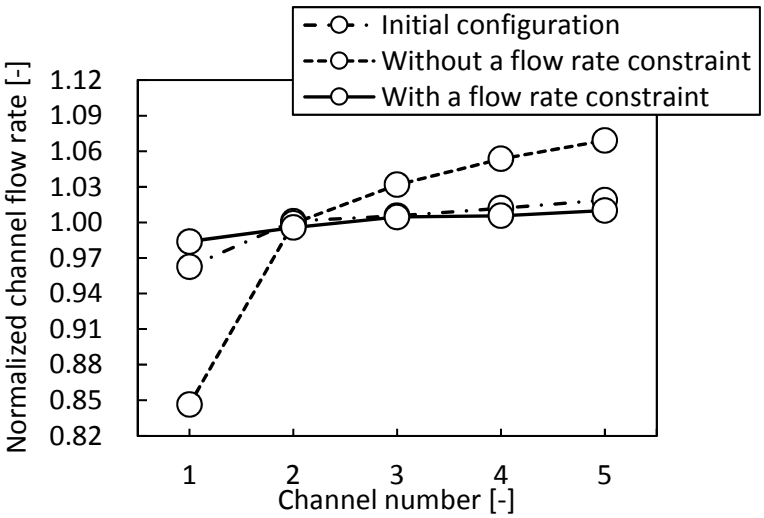

Fig. 3.17 Flow rate distributions among microchannels for U-type manifold optimal configurations with Re = 10. Normalized channel flow rate is defined as $Q_{\mathrm{e}}^{n}/(r_n Q_{\mathrm{in}})$, where Q_{e}^{n} and $r_n Q_{\mathrm{in}}$ are the actual and target flow rates in microchannel No. n, respectively.

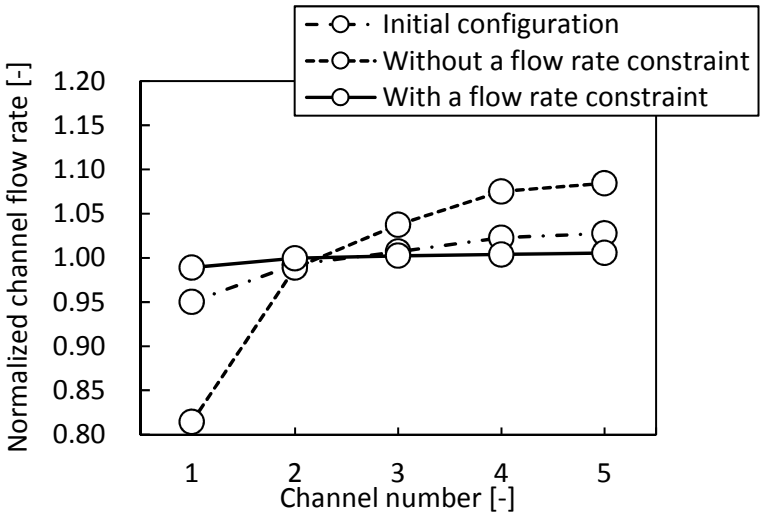

Fig. 3.18 Flow rate distributions among microchannels for U-type manifold optimal configurations with Re = 100. Normalized channel flow rate is defined as $Q_{\mathrm{e}}^{n}/(r_n Q_{\mathrm{in}})$, where Q_{e}^{n} and $r_n Q_{\mathrm{in}}$ are the actual and target flow rates in microchannel No. n, respectively.

3.7 Summary

In this Chapter, we applied our proposed topology optimization method with flow rate inequality constraint to a design for plate-type microchannel reactor manifolds, using a level

Table 3.5 The dissipated power values for U-type manifold optimizations. *P* represents the flow rate inequality constraint.

Re	Initial design	Optimal design without *P*	Optimal design with *P*
10	11.5	17.6	36.1
100	1.5	2.3	4.9

set-based topology optimization method, targeting flow uniformity. The method provides representative designs for Z-type and U-type manifolds that ensure sufficient flow uniformity among a five-microchannel array while minimizing pressure drop in the device. We obtained the following results.

- Optimization problems were formulated for Z-type and U-type manifold designs. Governing equations and boundary conditions for the adjoint field under a flow rate inequality constraint were formulated. The objective functional was defined as the total potential energy, which is equivalent to the pressure drop in the device.

- The topology optimization algorithm was constructed using a simplified method for determining the Lagrange multipliers, which were introduced to the adjoint equation due to the use of the flow rate inequality constraint. The values of the Lagrange multipliers were determined according to the relative errors between the prescribed flow rate and the actual flow rate for each of the five microchannels, using an exponential function. This implementation enables the creation of flow channel shapes in the manifolds that foster or inhibit flow at designated microchannels.

- Two numerical examples were examined for the Z-type and U-type manifold designs and the utility of the proposed optimization method was confirmed in both sets of problems. The proposed method successfully obtained appropriate optimal configurations

for manifold designs that achieve a prescribed flow rate equally distributed among a group of microchannels, and is applicable for different Reynolds number flows.

Chapter 4

Topology optimization for turbulent flow using an immersed boundary method

4.1 Introduction

The aim of this Chapter is to suggest the new topology optimization method for fluid problems especially focused on turbulent flow regime.

In conventional topology optimization approaches for fluid problems, employing the so-called Brinkman penalization method, the fixed design domain is assumed to be a porous medium by introducing the Darcy force term as an external source term in the Navier-Stokes equation, where the local porosities are considered as design variables.

When considering turbulent flow using CFD, several approaches are available for solving the equation for the eddy viscosity using so-called turbulence models, i.e., direct numerical simulation (DNS), large-eddy simulation (LES) [67], detached eddy simulation (DES) [69] and RANS simulation. The S-A turbulence model applied in previous studies concerning topology optimization problems [57, 38, 82] is an example of a one-equation RANS turbulence model typically used in external flow analyses, such as for aerodynamic problems. A particular turbulence model is selected for the numerical objective based on the trade-off

relationship between numerical accuracy and the computation time required for the numerical analysis.

Under turbulent flow, the flow velocity profile in the region near the wall can be categorized into three separate regions in increasing order of distance from the wall: a viscous sublayer, a logarithmic layer, and a defect layer. Within the boundary layer, the flow profile changes drastically, especially under turbulent flow as compared with laminar flow. For numerical simulation of turbulent flow, where the flow velocity changes radically in the vicinity of the wall, a precise solution of the flow in the boundary layer depends on the generation of a very small and dense numerical mesh. In general, $Re^{1.8}$ cell counts are needed to provide sufficient resolution in the boundary layer. LES or RANS turbulence models with low-Reynolds-number treatment are generally used to simulate turbulent flow when using a dense boundary layer mesh, but the time required for solving the governing equations becomes a critical issue in optimization processes. In particular, when combining CFD analysis with the topology optimization in a fluid problem, this usage leads to a drastic increase in the overall number of cells, since the numerical mesh in the fixed design domain basically consists of a fixed Cartesian grid, especially when using a topology optimization approach. Additionally, the numerical simulation of the turbulent flow must be iteratively calculated until the objective functional converges.

As an alternative to LES or RANS with low-Reynolds-number treatment, numerical cell counts near the wall can be reduced in RANS models based on a high-Reynolds-number treatment by introducing the wall function, which is based on empirical laws, to express and interpolate the velocity profile near the wall. To calculate the interpolation function, the distance from the wall, which is expressed as a fluid-solid interface in the topology optimization approach, must be obtained. Consequently, if the wall function can be introduced in the calculation of the governing equation, a coarser grid can be used near the

wall, which decreases the numerical cell counts in the topology optimization for turbulent flow.

Papoutsis-Kiachagias et al. [57] addressed a topology optimization problem under incompressible laminar and turbulent ducted flows, especially for manifold designs, and also extended their proposed method to a heat transfer problem. In their approach, based on the Brinkman penalization method, new porosity-dependent terms were added to the main governing equations of the heat transfer and turbulence models. Kontoleontos et al. [38] extended a heat transfer problem and imposed constraints on the outlet flow direction, rates and mean outlet temperatures. In their design sensitivity analysis, the adjoint to the Spalart-Allmaras (S-A) turbulence model equation is taken into account for a continuous adjoint approach, and the local porosities as design variables are updated depending on the design sensitivity, using the steepest descent method. Yoon [82] explored topology optimization for turbulent flow using the S-A model and revealed the importance of eddy viscosity effects upon the optimal designs of several ducted flows. In this approach, the wall equation represented by the Eikonal equation was considered to calculate the distance value from the closet wall. Dilgen et al. [23] proposed the topology optimization method for turbulent flow considering one- and two-equation turbulence models without any simplifying assumptions in the sensitivity analysis. They revealed that the frozen turbulence assumption was lack of accuracy compared with their exact difference of the sensitivity. All of these previous topology optimization approaches for turbulent flows used the Brinkman penalization method, so the effect of the no-slip boundary condition at the fluid-solid interface was implicitly considered.

When calculating the turbulent flows accurately, the imposition of the wall function is often introduce to interpolate the velocity and pressure profile near the wall with moderate grid size. However, as long as using the Brinkman penalization method, the fluid-solid interface lacks clear boundaries so that the wall function can not be introduced in the

optimization process. Also, the no-slip boundary condition can not be explicitly applied to the fluid-solid interface because the porous medium by nature has an indistinct interface. Consequently, the fluid velocity and pressure distribution near the fluid-solid interface of the obtained optimized design is passively determined depending on the initial settings of an artificial numerical coefficient of the Darcy force term, where larger inverse permeability coefficient values can cause precipitous changes in flow velocity and pressure near the fluid-solid interface. This passive determination of the velocity and pressure distribution may cause unrealistic profiles of the velocity and pressure. The inaccuracy of fluid behavior treatments near the wall may therefore lead to unrealistic optimal designs, especially when dealing with topology optimization problems under turbulent flow.

In this Chapter, we introduce the IBM proposed in [59, 58] to enforces the no-slip boundary condition by adding a body force to the Navier-Stokes equation as a reaction force from an object. In particular, the IBM in a discrete forcing approach proposed in [28] is widely used, and several extensions of this method have been proposed [29, 76, 64, 25, 78]. In this method, the body force is introduced after the governing equations are discretized, which allows the no-slip boundary condition to be imposed more directly than in a continuous forcing approach in which the body force is incorporated into the governing equations before discretization. Several other IBM approaches are clearly reviewed and categorized in [48]. Furthermore, to express the clear fluid-solid interface during the topology optimization, we apply the level-set based boundary expressions for precise evaluation of the fluid behavior near the wall under turbulent flow.

In pioneering research in topology optimization for turbulent flow using the IBM, Sarstedt et al. [63] proposed a topology optimization method based on local optimality criteria using k-ϵ and k-ω SST turbulence models. In their optimization approach, local optimality criteria are used to deal with the minimization of the pressure loss under a specific volume constraint. They also used the IBM in a discrete forcing approach with direct imposition of boundary

conditions for the representation of the fluid-solid interface and showed that arbitrary velocity profiles in the fixed design domain obtained with the IBM were in better agreement with profiles obtained when using a body-fitted mesh than when the IBM is not used, although the Brinkman penalization method is used. Agreement was ensured even in $Re = 2500$ turbulent flow, whereas differences increase with higher Re values unless the IBM is used.

In this Chapter, we propose a level set-based topology optimization method for fluid flows under the turbulent regimes without using the Brinkman penalization approach. We apply a RANS model based on the high-Reynolds-number treatment and include the wall function in the optimization problem, and introduce two-equation turbulence models, k-ϵ and k-ω, in this thesis. We note that, among various turbulence models, the RANS-based numerical simulation is one of the most commonly used approaches in different kinds of fluid optimization problems, because it provides reasonable numerical simulation accuracy with a relatively low computational requirement, compared with other approaches such as LES and DES. We implement the no-slip boundary condition explicitly, using the IBM, on the fluid-solid interface of newly created holes during the topology optimization process and introduce the IBM of the discrete forcing approach, with direct imposition of boundary conditions [46, 35, 75, 48]. Furthermore, owing to the introduction of a LSF for the expression of the fluid-solid interface, the calculation of distances from the wall required for wall function calculations is thereby facilitated.

4.2 Governing equation

4.2.1 Reynolds-averaged Navier-Stokes equations

For incompressible turbulent flow, all state variables have two components: a time-averaged component, and a fluctuating component. In case of the velocity vector, u_i has $\bar{u}_i$ as the time-averaged component and u_i' as the fluctuating component, with $u_i = \bar{u}_i + u_i'$. The

Reynolds-averaged Navier-Stokes (RANS) and continuity equations can now be written as

$$F_i^u := u_j \frac{\partial u_i}{\partial x_j} + \frac{\partial p}{\partial x_i} - \frac{\partial}{\partial x_j}\left\{(\nu + \nu_t)\left(\frac{\partial u_i}{\partial x_j} + \frac{\partial u_j}{\partial x_i}\right)\right\} = 0,\ i = 1,2,(3,) \tag{4.1}$$

$$F^p := \frac{\partial u_i}{\partial x_i} = 0\,, \tag{4.2}$$

where u_i is the velocity vector component of the fluid, p is the static pressure, ν is the constant bulk kinematic viscosity, and ν_t is the turbulent kinematic viscosity. Note that the mean flow is assumed to obey a steady state condition in this study.

4.2.2 Turbulence model

In this study, widely used two-equation RANS turbulence models for the eddy-viscosity model, k-ϵ and k-ω, are introduced in the topology optimization problem to express the turbulent viscosity. The characteristics of the two turbulence models are as follows. In general, the k-ϵ turbulence model most popular due to its numerical stability and relatively low computational requirements, although analysis accuracy tends to decrease when considering separation or swirl flow. The k-ω turbulence model provides better analysis accuracy of separation flow than does the k-ϵ turbulence model, and flow near the wall can be solved with better numerical stability.

k-ϵ turbulence model

For the k-ϵ turbulence model [42], the turbulence state variables k and ϵ, the turbulent kinetic energy and energy dissipation, respectively, are defined in the following governing equations:

$$F^k|_\epsilon := u_j \frac{\partial k}{\partial x_j} - \frac{\partial}{\partial x_j}\left\{\left(\nu + \frac{\nu_t}{Pr_k}\right)\frac{\partial k}{\partial x_j}\right\} - P_k + \epsilon = 0 \tag{4.3}$$

$$F^\epsilon := u_j \frac{\partial \epsilon}{\partial x_j} - \frac{\partial}{\partial x_j}\left\{\left(\nu + \frac{\nu_t}{Pr_\epsilon}\right)\frac{\partial \epsilon}{\partial x_j}\right\} - C_1 P_k \frac{\epsilon}{k} + C_2 \frac{\epsilon^2}{k} = 0, \tag{4.4}$$

where the production term P_k, meaning the production of k, is defined as

$$P_k = \tau_{ij}\frac{\partial u_i}{\partial x_j} = \nu_t\left(\frac{\partial u_i}{\partial x_j} + \frac{\partial u_j}{\partial x_i}\right)\frac{\partial u_i}{\partial x_j}. \tag{4.5}$$

Here, the turbulent kinematic viscosity coefficient ν_t and the empirical constants are

$$\nu_t = C_\mu\frac{k^2}{\epsilon},\ C_\mu = 0.09,\ C_1 = 1.44,\ C_2 = 1.92,\ Pr_k = 1.0,\ Pr_\epsilon = 1.3, \tag{4.6}$$

where Pr_k and Pr_ϵ are turbulent Prandtl numbers.

k-ω turbulence model

For the standard k-ω turbulence model [79], the turbulent kinetic energy k and the specific dissipation rate ω can be obtained by solving the following PDEs:

$$F^k|_\omega := u_j\frac{\partial k}{\partial x_j} - \frac{\partial}{\partial x_j}\left\{(\nu + \sigma_k\nu_t)\frac{\partial k}{\partial x_j}\right\} - P_k + \beta^* k\omega = 0 \tag{4.7}$$

$$F^\omega := u_j\frac{\partial \omega}{\partial x_j} - \frac{\partial}{\partial x_j}\left\{(\nu + \sigma_\omega\nu_t)\frac{\partial \omega}{\partial x_j}\right\} - \alpha P_k\frac{\omega}{k} + \beta\omega^2 = 0. \tag{4.8}$$

Here, the turbulent kinematic viscosity coefficient ν_t and the empirical constants are

$$\begin{aligned}
&\nu_t = \frac{k}{\omega},\ \alpha = \frac{13}{25},\ \beta = \beta_0 f_\beta,\ \beta^* = \beta_0^* f_{\beta^*},\ \sigma_k = 0.5,\ \sigma_\omega = 0.5,\\
&\beta_0 = \frac{9}{125},\ \beta_0^* = 0.09,\ f_\beta = \frac{1+70\chi_\omega}{1+80\chi_\omega},\ \chi_\omega = \left|\frac{\Omega_{ij}\Omega_{jk}S_{ki}}{(\beta_0^*\omega)^3}\right|,\\
&f_{\beta^*} = \begin{cases} 1 & (\chi_k \le 0) \\ \dfrac{1+680\chi_k^2}{1+80\chi_k^2} & (\chi_k > 0) \end{cases},\ \chi_k = \frac{1}{\omega^3}\frac{\partial k}{\partial x_j}\frac{\partial \omega}{\partial x_j},
\end{aligned} \tag{4.9}$$

where the mean rate-of-rotation tensor Ω_{ij} and the mean rate-of-strain tensor S_{ij} are expressed as

$$\Omega_{ij} = \frac{1}{2}\left(\frac{\partial u_i}{\partial x_j} - \frac{\partial u_j}{\partial x_i}\right),\ S_{ij} = \frac{1}{2}\left(\frac{\partial u_i}{\partial x_j} + \frac{\partial u_j}{\partial x_i}\right). \tag{4.10}$$

Note that the relation between the energy dissipation ϵ and the specific dissipation ω is defined such that

$$\epsilon = \beta^* \omega k. \tag{4.11}$$

4.2.3 Wall function

In the numerical simulation of the turbulent flow, precise solutions of the boundary layer flow where the flow velocity changes drastically near the wall depend on the generation of a dense numerical mesh. To prevent an increase in the overall cell counts, a wall function is introduced [36], as typically used in the CFD field. In the standard wall function, the fluid velocity profile is determined using a specific interpolation function based on the distance of points from the wall, within the viscous sublayer and the logarithmic layer, the so-called High-Reynolds-Number treatment, which reduces the cell counts near the wall.

In our study, Spalding's law of the wall [70] is applied using one of the well-known wall functions as a unified wall function:

$$y^+ = u^+ + \frac{1}{E}\left\{e^{\kappa u^+} - 1 - \kappa u^+ - \frac{1}{2}\left(\kappa u^+\right)^2 - \frac{1}{6}\left(\kappa u^+\right)^3\right\}, \tag{4.12}$$

where the Karman constant $\kappa = 0.42$, another constant $E = 9.1$, and $y^+ = y_0 u_\tau/\nu$ and $u^+ = \bar{u}_0/u_\tau$ represent the non-dimensional distance from the wall and the non-dimensional velocity, respectively. $u_\tau = \sqrt{\tau_w/\rho}$ represents the friction velocity, τ_w the wall shear stress, y_0 denotes the distance from the wall, and $\bar{u}_0$ denotes the mean flow velocity.

Additionally, by calculating the friction velocity u_τ using Spalding's law of the wall, the turbulent viscosity near the wall, $\nu_{t_{\text{wall}}}$, can be calculated as follows:

$$\nu_{t_{\text{wall}}} = \frac{u_\tau^2}{\left|\dfrac{\partial \boldsymbol{u}}{\partial \boldsymbol{n}}\right|} - \nu. \tag{4.13}$$

Note that the friction velocity u_τ is obtained using an iterative calculation based on the Newton-Raphson method.

4.3 Sensitivity analysis based on the adjoint method

In this section, we formulate the topology optimization problem for incompressible turbulent flow. Additionally, corresponding to the sensitivity analysis, we introduce the topological derivative of the Navier-Stokes equations as proposed in [4].

4.3.1 Topology optimization problem for incompressible turbulent flow

In this study, we focus on the total pressure drop of a fluid in internal flow as an objective functional. The total pressure drop is formulated as

$$J := -\int_{\partial D} \left\{ \left(p + \frac{1}{2}\boldsymbol{u}\cdot\boldsymbol{u} \right) \boldsymbol{u}\cdot\boldsymbol{n} \right\} \mathrm{d}D. \tag{4.14}$$

Consequently, when governing equations Eqs. (4.1)–(4.4) and Eqs. (4.7) and (4.8) are satisfied under specific boundary conditions, the topology optimization problem to minimize the total pressure drop under incompressible turbulent flow can be formulated as follows:

$$\inf_{\phi} \quad J\left(\boldsymbol{u}, \chi_\phi\right) \tag{4.15}$$

$$\text{subject to} \quad V\left(\chi_\phi\right) \leq 0, \tag{4.16}$$

where V is the fluid volume constraint functional, with $V = \int_D \chi_\phi \, \mathrm{d}D - V_{\max}$, and $V_{\max}$ represents the upper limit of the fluid region in the design domain.

Next, based on Lagrange's method of undetermined multipliers, the above constrained optimization problem is replaced with an unconstrained problem, with Lagrangian $\bar{J}$ defined as

$$\bar{J} = J\left(\boldsymbol{u}, \chi_\phi\right) + \lambda V\left(\chi_\phi\right), \tag{4.17}$$

where λ is the Lagrange multiplier.

In our study, the "frozen turbulence" hypothesis [26] is assumed for the state variables in the employed turbulence models k, ϵ and ω. This means that the turbulent state variables are independent of the design variable χ_ϕ and can be regarded as constants, which allows the derivation with respect to the turbulent variables to be ignored in the design sensitivity analysis [53].

4.3.2 Topological derivatives

Here, we propose an explicit method for imposing the no-slip boundary condition on the fluid-solid interface in the topology optimization for the fluid problem. To impose this condition during the topology optimization, we use the topological derivative as the design sensitivity, as explained below. The topological derivative is defined as the change in a cost function given an infinitesimally small perturbation. The topological derivative is expressed as the following limit:

$$d_\tau \bar{J}(\Omega)(\boldsymbol{x}) := \lim_{r \to 0} \frac{\bar{J}(\Omega \backslash B(\boldsymbol{x}, r)) - \bar{J}(\Omega)}{\mathrm{meas}(\Omega \backslash B(\boldsymbol{x}, r)) - \mathrm{meas}(\Omega)}, \tag{4.18}$$

where $B(\boldsymbol{x}, r)$ indicates a small obstacle of radius r located at some certain point $\boldsymbol{x}$. The concept of the topological derivative is illustrated in Fig.4.1, where the fluid inlet, outlet

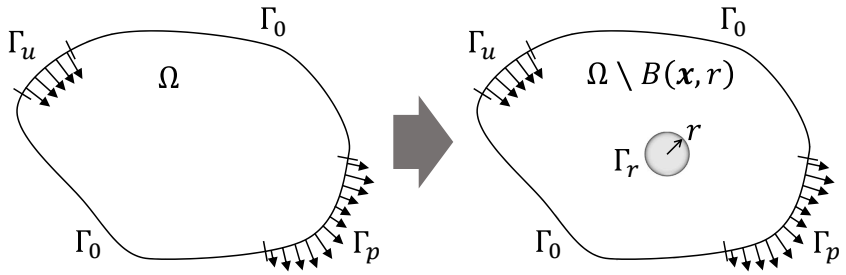

Fig. 4.1 Schematic representation of the topological derivative concept

and wall boundaries are represented as Γ_u, Γ_p and Γ_0 respectively. The boundary of a newly created small obstacle $B(\boldsymbol{x}, r)$ with radius r is represented as Γ_r.

For topology optimization of fluid problems, a small perturbation implies that a small obstacle is created in the fluid domain within the fixed design domain. Based on a previous study [5], the effect of imposing a no-slip boundary condition along boundary Γ_r of a newly created obstacle B can be taken into account by using the topological derivative. Having introduced the topological derivative, a method for explicitly imposing the no-slip boundary condition can be implemented. To accomplish this, we present a method for using the IBM with the LSF, as will be explained in Sec.4.4.

Based on the asymptotic analysis presented in a previous study [4], the topological derivative in two-dimensional problems can be developed as [19]:

$$d_\tau \bar{J}(\Omega)(\boldsymbol{x}) = 4\pi\eta \boldsymbol{u} \cdot \boldsymbol{v} + d_\tau J(\Omega)(\boldsymbol{x}) - \lambda d_\tau V(\Omega)(\boldsymbol{x}), \tag{4.19}$$

where $\boldsymbol{v}$ is the adjoint variable of $\boldsymbol{u}$, obtained by solving the adjoint equation as follows:

$$F_i^v := -u_j\frac{\partial v_i}{\partial x_j} + v_j\frac{\partial u_j}{\partial x_j} + \frac{\partial q}{\partial x_i} - \frac{\partial}{\partial x_j}\left\{(\nu+\nu_t)\left(\frac{\partial v_i}{\partial x_j}+\frac{\partial v_j}{\partial x_i}\right)\right\} = 0 \tag{4.20}$$

$$F^q := \frac{\partial v_i}{\partial x_i} = 0 \tag{4.21}$$

$$v_i u_j n_j + (\nu+\nu_t)\left(\frac{\partial v_i}{\partial x_j}+\frac{\partial v_j}{\partial x_i}\right)n_j - q n_i + \frac{\partial j_{\Gamma,k}}{\partial u_i}n_k = 0 \qquad on \quad \Gamma_{\text{out}} \tag{4.22}$$

$$v_j n_j = -\frac{\partial j_{\Gamma,i}}{\partial p}n_i \qquad on \quad \Gamma_{\text{in}} \cup \Gamma_{\text{wall}}, \tag{4.23}$$

where q is the adjoint variable of p. The development of the above adjoint equation is presented in detail in [53].

Based on the asymptotic expansion, $d_\tau J(\Omega)(\boldsymbol{x})$, which is the derivative of the objective functional J with respect to the design variable, is expressed as

$$J(\phi+\psi(\boldsymbol{x},r)) - J(\phi) = f(r)d_\tau J(\Omega)(\boldsymbol{x}) + o(f(r)), \tag{4.24}$$

where $f(r)$ is a positive function whose value approaches zero as r approaches zero:

$$\lim_{r\to 0} f(r) = 0\,. \tag{4.25}$$

According to [4], $f(r)$ can be formulated as

$$f(r) = -\frac{1}{\ln r}. \tag{4.26}$$

Consequently, $d_\tau J(\Omega)(\boldsymbol{x})$ can be obtained as

$$d_\tau J(\Omega)(\boldsymbol{x}) = 0. \tag{4.27}$$

The derivative of the volume constraint functional V can be also expressed as

$$d_\tau V(\Omega)(\boldsymbol{x}) = -\pi. \tag{4.28}$$

Finally, we obtain the topological derivative for the optimization problem as follows:

$$d_\tau \bar{J}(\Omega)(\boldsymbol{x}) = \bar{J}' = 4\pi\rho\eta\boldsymbol{u}\cdot\boldsymbol{v} + \pi\lambda, \tag{4.29}$$

where the value of λ is set as zero when the volume constraint V is inactive. When V is active, the value of λ is decided based on Eq.(2.8) [41], as follows:

$$\lambda = -\frac{\int_D \left(\bar{J}' + \tau\nabla^2\phi\right) dD}{\int_D dD}, \tag{4.30}$$

where the Lagrange multiplier λ is updated using the following exponential function,

$$\bar{\lambda} = \lambda \exp(V). \tag{4.31}$$

The relative error of the fluid volume constraint approaches a sufficiently small value, the value of $\bar{\lambda}$ gradually becomes small.

4.4 Immersed boundary method for near wall treatment

We now develop the level set-based topology optimization method to enable the precise evaluation of the fluid behavior near the wall, especially focusing on steady state incompressible turbulent flow. Under turbulent flow, the flow treatment near the wall becomes critical, compared with the treatment under a laminar flow condition, because the two flow profiles are radically different, as shown in Fig.4.2. The difference between the profiles indicates that accurate estimations of the shear stress are increasingly difficult as the wall is approached in

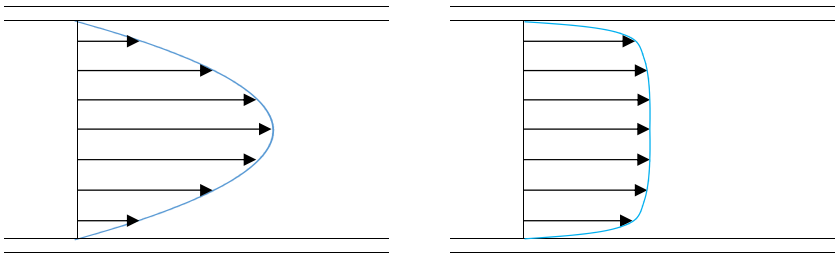

Fig. 4.2 Schematic representation of velocity profiles under laminar and turbulent ducted flows.

turbulent flow. The low accuracy of shear stress estimations eventually causes unavoidable mis-evaluations to appear in the optimal configuration resulting from an optimization.

4.4.1 Conventional IBM approaches for imposition of solid-fluid interface boundary conditions

To implement the no-slip boundary condition along the fluid-solid interface, almost all previous studies of topology optimization for fluid problems use the Brinkman penalization method, an IBM, where the fixed design domain is assumed to be a porous medium and is expressed by introducing the Darcy force term as the source term in the Navier-Stokes equation, as follows:

$$F_i^u := u_j \frac{\partial u_i}{\partial x_j} + \frac{\partial p}{\partial x_i} - \frac{\partial}{\partial x_j}\left\{(\nu + \nu_t)\left(\frac{\partial u_i}{\partial x_j} + \frac{\partial u_j}{\partial x_i}\right)\right\} + \alpha u_i = 0\,. \tag{4.32}$$

Here, the last term of left-hand side in Eq.(4.32) is the Darcy force term, and α represents the impermeability coefficient.

In the fluid domain, the Darcy force term αu_i becomes zero when $\alpha = 0$, at which point the Darcy force term can be eliminated and the Navier-Stokes equation returns to its original form. On the other hand, the value set for α in the solid domain must be carefully considered. For numerical reasons, α cannot be set to an infinite value in the solid domain, so a reasonable

value needs to be preassigned. However, the most effective value of α in the solid domain will depend on the particular design problem. Another factor is that if the value of α is set too high, numerical errors will occur as calculation output oscillates wildly during the optimization procedure [43]. On the other hand, if the value of α is set too low in the solid domain, the flow may penetrate into the solid domain [39, 7, 40]. We therefore note that the above approaches, based on the Brinkman penalization method, do not strictly ensure that a no-slip boundary condition will be imposed on the solid-fluid interface, due to the use of an arbitrary value of α.

In contrast to the above approaches, Challis and Guest presented a topology optimization method for Stokes flow that includes an explicitly enforced no-slip boundary condition during the optimization process [18]. They introduced the topological derivative as the design sensitivity and solved the Hamilton-Jacobi equation every five iterations, to evolve the level set function during the topology optimization. In a topology optimization problem for Navier-Stokes flow, Deng et al. [19] showed that the topological derivative can be considered as a weighted sum in the Hamilton-Jacobi equation for the evolution of the level set function. In their method, a reasonable weighting value for the topological derivative was determined after numerical examination prior to the optimization. This problematic need to set the values of certain parameters by hand also appears in [17, 33, 6]

4.4.2 Ghost-cell-based IBM incorporated with the level set function

As mentioned in Sec. 4.3.2, in our approach, the ghost-cell-based IBM (GCIBM) is applied during the optimization process to introduce the no-slip boundary condition explicitly along the fluid-solid interface expressed by the zero iso-surface of the LSF.

In the GCIBM, the boundary condition on the immersed boundary (IB) is enforced using ghost cells. For the computational cells along the IB, ghost cells are defined as being located in the solid domain, while cells in the fluid domain are defined as IB cells. This means that

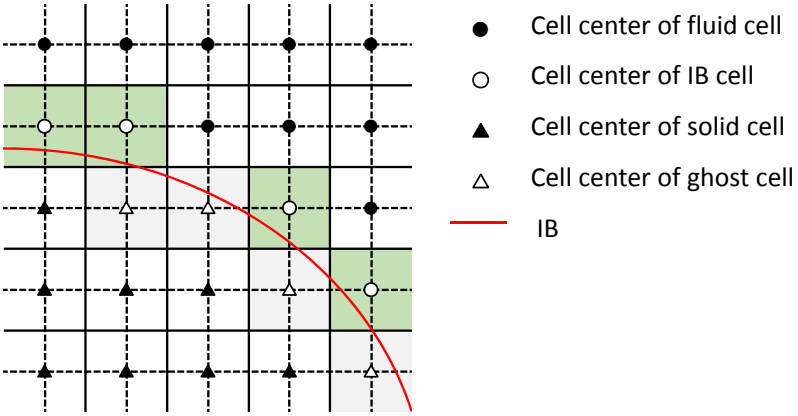

Fig. 4.3 Schematic representation of ghost cells and immersed boundary (IB) cells in computational domain.

the cell center of a ghost cell is considered to lie in the solid domain, while that of an IB cell lies in the fluid domain. A schematic representation of the cell locations and relationships is illustrated in Fig.4.3.

We now address the explicit imposition of the no-slip boundary condition with respect to the flow velocity u_i and pressure p using the GCIBM. The basic concept of the GCIBM is that the state variables of u_i and p for an IB cell whose center is located at $\boldsymbol{x}_{\mathrm{ib}}$ adjacent to the IB line, regarded as the zero iso-contour of the LSF, are interpolated depending on the no-slip boundary condition applied to the zero iso-contour of the LSF, based on the distance between $\boldsymbol{x}_{\mathrm{ib}}$ and the zero iso-contour of the LSF.

Now, due to the use of the LSF, an arbitrary point $\boldsymbol{x}_{\mathrm{zlsf}}$ on the zero iso-contour of the LSF located orthogonally in relation to an IB cell with center $\boldsymbol{x}_{\mathrm{ib}}$ can be easily determined using the following relation:

$$\boldsymbol{x}_{\mathrm{zlsf}} = \boldsymbol{x}_{\mathrm{ib}} - \frac{\nabla\phi(\boldsymbol{x}_{\mathrm{ib}})}{|\nabla\phi(\boldsymbol{x}_{\mathrm{ib}})|^2}\phi(\boldsymbol{x}_{\mathrm{ib}}). \tag{4.33}$$

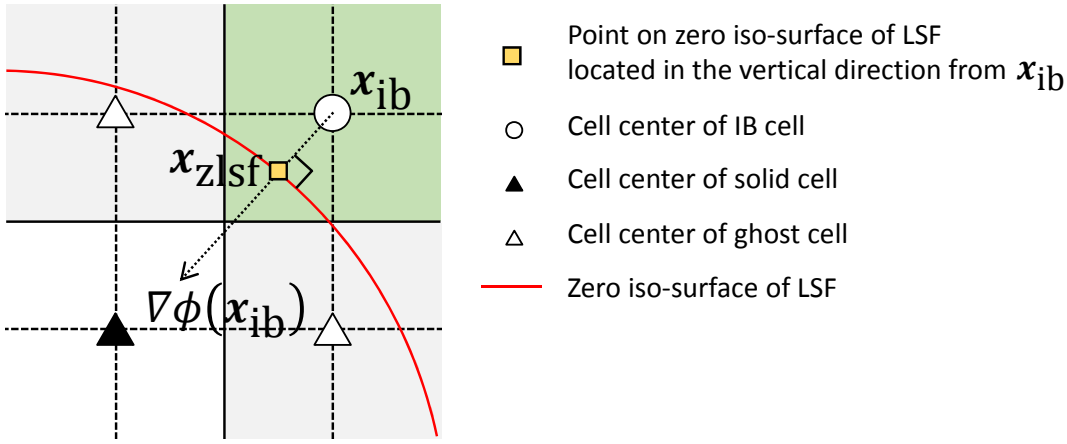

Fig. 4.4 Schematic representation of an arbitrary point on the zero iso-surface of the LSF located orthogonally from an IB cell.

A schematic representation showing this relationship in the region near the solid-fluid interface is given in Fig.4.4.

Finally, the velocity and pressure can be interpolated by the second order differentiable function, so that the state variables Ψ of an IB cell with center $\boldsymbol{x}_{\mathrm{ib}}$ assuming the imposition of Dirichlet and Neumann boundary conditions can be determined as follows, using an interpolation second-order polynomial based on the distance between $\boldsymbol{x}_{\mathrm{zlsf}}$ and $\boldsymbol{x}_{\mathrm{ib}}$.

- Dirichlet boundary condition

$$\Psi(\boldsymbol{x}_{\mathrm{ib}}) = \Psi(\boldsymbol{x}_{\mathrm{zlsf}}) + E_0 + \boldsymbol{E}_1\boldsymbol{X} + \boldsymbol{X}^T\boldsymbol{E}_2\boldsymbol{X} \tag{4.34}$$

- Neumann boundary condition

$$\Psi(\boldsymbol{x}_{\mathrm{ib}}) = F_0 + \boldsymbol{F}_1\boldsymbol{x}'_{\mathrm{zlsf}} + \left(\boldsymbol{x}'_{\mathrm{zlsf}}\right)^T\boldsymbol{F}_2\boldsymbol{x}'_{\mathrm{zlsf}} \tag{4.35}$$

Where scalars E_0, F_0, vectors $\boldsymbol{E}_1$, $\boldsymbol{F}_1$ and tensors $\boldsymbol{E}_2$, $\boldsymbol{F}_2$ are determined by the least square method. $\boldsymbol{X} = \boldsymbol{x}_{\mathrm{ib}} - \boldsymbol{x}_{\mathrm{zlsf}}$, and $\boldsymbol{x}^{'}_{\mathrm{zlsf}}$ denotes the point lying on the zero iso-contour of the LSF in the coordinate system in which the orthogonal vector is considered as the basis vector (yellow square in Fig.4.4).

Here, the velocity and pressure of an IB cell with center $\boldsymbol{x}_{\mathrm{ib}}$ assuming the imposition of Dirichlet boundary condition for the velocity and Neumann boundary condition for the pressure can be determined as follows.

- Dirichlet boundary condition for the velocity

$$\boldsymbol{u}(\boldsymbol{X}_{\mathrm{ib}}) = \boldsymbol{E}_1 \boldsymbol{X}_{\mathrm{ib}} + \boldsymbol{X}_{\mathrm{ib}}^T \boldsymbol{E}_2 \boldsymbol{X}_{\mathrm{ib}} \tag{4.36}$$

- Neumann boundary condition for the pressure

$$p(\boldsymbol{x}_{\mathrm{ib}}) = F_0 + \boldsymbol{F}_1 \boldsymbol{x}^{'}_{\mathrm{zlsf}} + \left(\boldsymbol{x}^{'}_{\mathrm{zlsf}}\right)^T \boldsymbol{F}_2 \boldsymbol{x}^{'}_{\mathrm{zlsf}} \tag{4.37}$$

A schematic representation of the imposition of both Dirichlet and Neumann boundary conditions are illustrated in Fig.4.5.

4.5 Numerical implementation

4.5.1 Optimization algorithm

Fig.4.6 shows the optimization algorithm applied in this study. The procedure is as follows.

(1) The initial distribution of the LSF is defined with $\phi = 1$ in the fixed design domain D, so that it is filled with fluid.

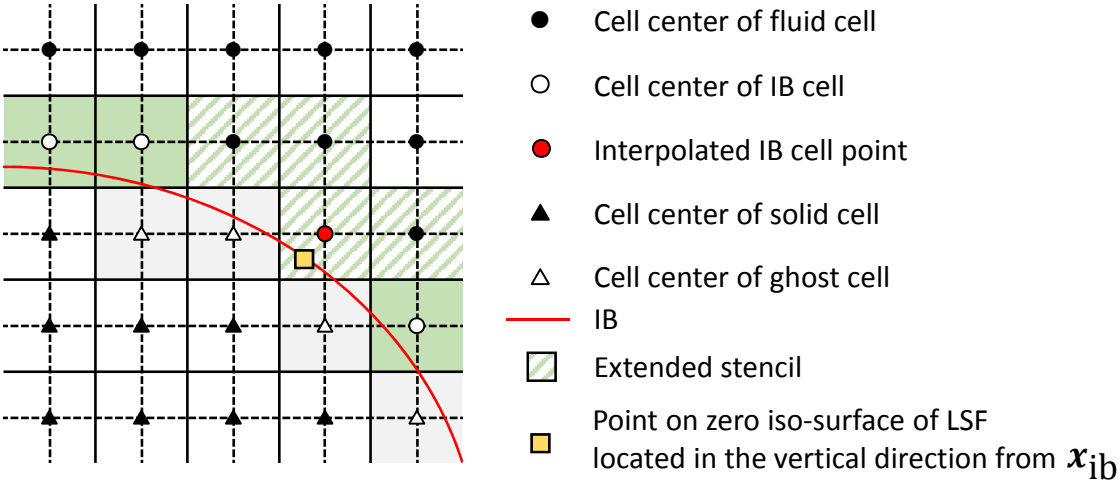

Fig. 4.5 The schematic of the imposition of Dirichlet and Neumann boundary conditions on IB cell.

(2) The governing equations of the fluid problem are solved using FVM analysis with the SIMPLE algorithm, and the distributions of velocity u_i and pressure p are obtained, as are the values of the objective functional J and constraint functional V.

(3) If the criteria of the objective and constraint functionals are satisfied, the optimization is finished and an optimal configuration is obtained; otherwise, the adjoint problem is solved.

(4) The design sensitivity is calculated using the solution of the governing equations and adjoint equations. The LSF is then updated by calculating the reaction diffusion equation, using FVM analysis.

In this paper, the optimization procedure is repeated until the value of the objective functional satisfies the following criterion:

$$\left|\frac{J_{t+1}-J_t}{J_t}\right| < \epsilon, \tag{4.38}$$

where index t represents the time interval for iteration of the optimization procedure. We implement this criterion with $\epsilon = 1 \times 10^{-4}$.

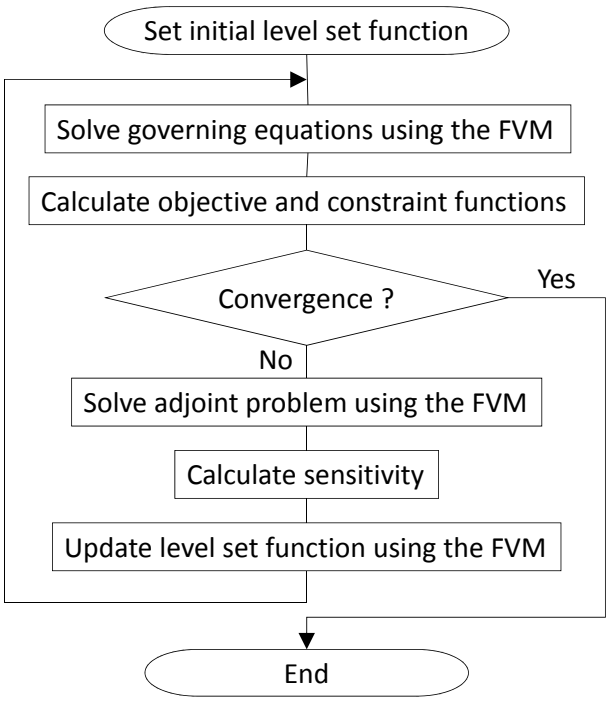

Fig. 4.6 Flowchart of the optimization procedure.

4.5.2 Numerical method for the time evolution equation

In this paper, the FVM is used for the discretization of the time evolution equation of the LSF (2.8).

First, the time evolution equation (2.8) is integrated for both sides, as follows:

$$\int_V \frac{\partial \phi}{\partial t} \mathrm{d}V = -\int_V K(\phi)\left(\bar{J}' - \tau \nabla^2 \phi\right) \mathrm{d}V. \tag{4.39}$$

Next, the following equation can be obtained by applying Gauss's divergence theorem.

$$\int_V \frac{\partial \phi}{\partial t} \mathrm{d}V = -\int_V K(\phi)\,\bar{J}'\,\mathrm{d}V - \int_S (\tau \nabla \phi) \cdot \boldsymbol{n}\,\mathrm{d}S. \tag{4.40}$$

Consequently, the level set function can be updated by solving the following equation using the implicit Euler method.

$$\left(\frac{\phi^{n+1}-\phi^{n}}{\Delta t}\right)V_c+\tau\sum_{f}\nabla\phi^{n+1}\boldsymbol{S}_f=-K(\phi)\,\bar{J}'V_c, \tag{4.41}$$

where V_c and Δt represent the control volume of the FVM and the time increment, respectively. ϕ^n and ϕ^{n+1} represent the level set function at the current and next time step. Finally, $\sum_f(\cdot)$ represents the summation of element surface component values, and $\boldsymbol{S}_f$ represents the area vector of element surfaces.

4.6 Numerical examples

In this section, we present numerical examples of topology optimization problems for turbulent flows, ducted flows in particular. To verify that the proposed optimization method functions appropriately, we examine two-dimensional total pressure drop minimization problems for steady-state incompressible turbulent flow. Throughout the following numerical examples, the flow distribution at the flow inlet boundary Γ_{in} is assumed to be a developed flow distribution in a channel within Cartesian coordinates $s\in[-L_0/2, L_0/2]$, as represented below.

$$\boldsymbol{u}=\boldsymbol{u}_{\max}\left(1-\frac{2\,s}{L_0}\right)^{(1/n)}, \tag{4.42}$$

where $\boldsymbol{u}_{\max}$ is the maximum magnitude of the velocity at the center of the flow inlet Γ_{in}, whose length is symbolically represented as L_0. n is a Re parameter set so that $n := 2log_{10}\frac{Re}{10}$. The Reynolds number is represented as $Re = U_0L_0/\nu$, where the characteristic velocity U_0 and characteristic length L_0 are defined as the averaged value of the inlet velocity and the width of the inlet, respectively.

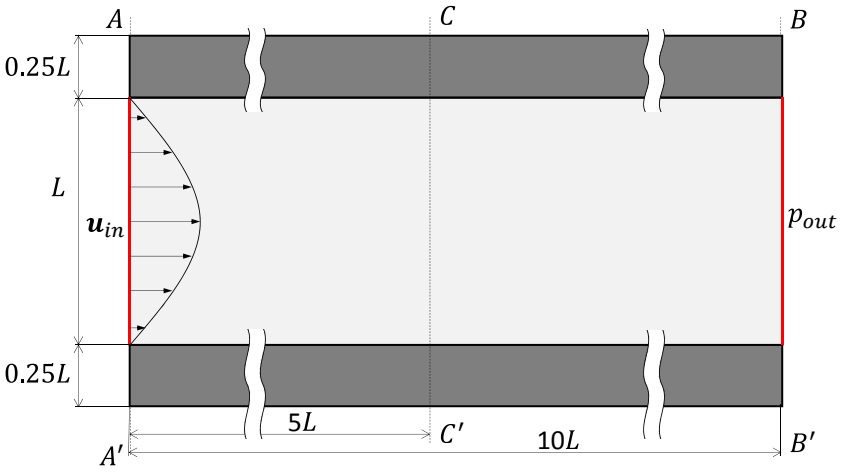

Fig. 4.7 Computational domain settings for channel flow.

The initial distribution of ϕ is set as 1 for the entire fixed design domain in all numerical examples so that the fixed design domain is filled with fluid for the initial configuration in the optimization problems.

4.6.1 Two-dimensional channel flow

To verify the operation of the proposed GCIBM before proceeding to the numerical example of the topology optimization problem, we first conduct a two-dimensional channel flow analysis (Fig.4.7) under a turbulent flow condition, using both k-ϵ and k-ω turbulence models. The Reynolds number is set as Re = 10000. The maximum magnitude of the velocity is set as $\boldsymbol{u}_{\max}$ = 1. The turbulence intensity and mixing length are specified as 5% and 0.07 at the inlet boundary, respectively. The wall is modeled as a fluid-solid interface using GCIBM and LSF. We compare flow profiles near the fluid-solid interface with those at the actual wall.

Additionally, the channel flow is calculated for two types of computational mesh distribution (structured meshes are inclined with respect to flow direction at 0 deg. and 45 deg. as shown in Fig.4.8). We aim to examine the dependency of the flow profile according to the location of the fluid-solid interface, because this interface can be located anywhere within the design domain during the topology optimization process.

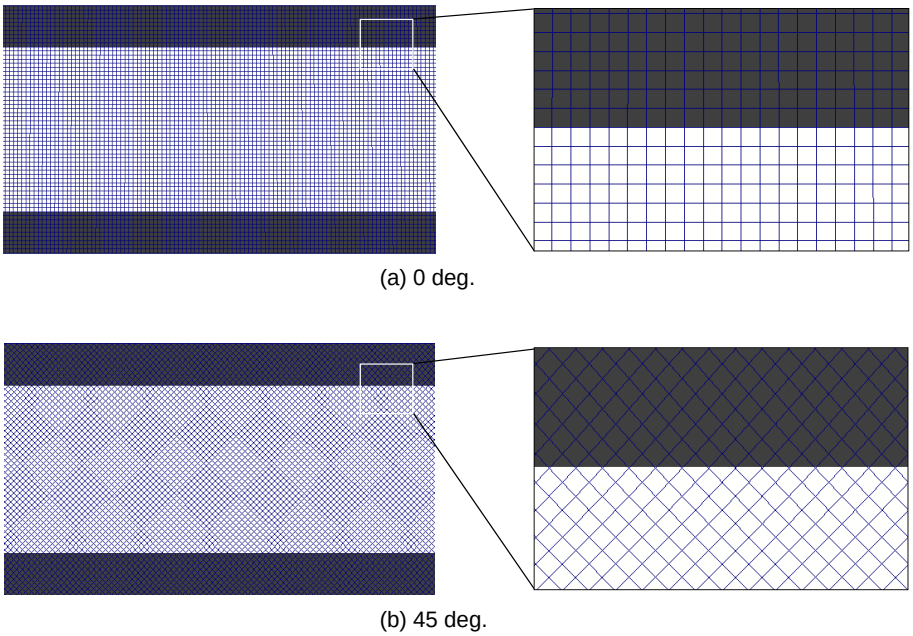

(a) 0 deg.

(b) 45 deg.

Fig. 4.8 Computational mesh distributions for channel flow. The gray and white regions mean solid and fluid regions, respectively.

Flow profile comparisons based on different computational mesh resolutions

The velocity profiles calculated for three different mesh resolutions, namely, 6000 total cells (coarse), 24000 cells (moderate) and 96000 cells (fine), are evaluated at A-A′ , B-B′ and C-C′ sections illustrated in Fig.4.7 that are the inlet and outlet boundaries, and a vertical line midway between the inlet and outlet boundaries of the total channel length, respectively.

Velocity profiles for the fluid-solid interface regions with k-ϵ and k-ω turbulence models are shown in Figs.4.9 and 4.10 for the A-A′, B-B′ and C-C′ sections, respectively. As shown in Figs.4.9 and 4.10, the inlet velocity profile (A-A′) is practically identical to the result that includes the actual wall, whereas the velocity profiles are slightly different in the downstream areas (B-B′ and C-C′) in both turbulence models for all considered computational mesh distributions. Although there are minor discrepancies near the wall region depicted in Figs.4.9 and 4.10, these become small for higher mesh resolutions.

Comparison of flow profiles for different computational mesh orientations

In this section, we examine flow profiles for two different grid orientations, shown in Fig.4.8, to validate the GCIBM for an inclined grid using k-ϵ turbulence model.

Figure 4.11 illustrates that the flow velocity profile under turbulent flow conditions using a mesh inclined at 45 deg. is practically identical to that for a non-inclined mesh, for all evaluation sections. These results allow us to conclude that the proposed GCIBM provides a valid representation of the fluid-solid interface.

4.6.2 Diffuser problem

Here, the first numerical example of a topology optimization for turbulent flow is the well-known diffuser problem for a two-dimensional case. As shown in Fig.4.12, fluid flows from an inlet at the left side and exits at an outlet at the right side, after moving through a square design domain with $L = L_0$. The inlet and outlet domains are set as non-design domains. The transition Reynolds number in ducted flow is roughly between $Re = 2300$ and 4000, so the Reynolds number is set as $Re = 5000$ and 10000 to elicit a fully turbulent flow condition in ducted flow. In this numerical example, the k-ϵ turbulence model is used. The volume constraint is set as $V_{\max} = 0.7$. We evaluated this problem using two different meshes, one consisting of a 90×90 mesh (x and y direction divisions), the other a 120×120 mesh, both providing a square design domain. The following parameters are set: maximum magnitude of the velocity $\boldsymbol{u}_{\max} = 1$, and the regularization parameter $\tau = 1 \times 10^{-2}$. The turbulence intensity and mixing length are specified as 1% and 0.0175 at the inlet boundary, respectively.

Dependency of optimal configurations on mesh resolution

To examine the dependency of optimal configurations on mesh resolution, we use 90×90 and 120×120 meshes (x and y direction divisions) with the Reynolds number set as 10000 for both cases. The convergence history of the objective functional and volume constraint

especially for a 120×120 meshes are shown in Fig.4.13. The results (Fig.4.14) indicate that practically identical configurations were obtained, hence the dependency of the optimal configurations on the mesh resolution is quite low.

The physically reasonable optimal configuration, which has a gradually convergent shape from inlet to outlet, was obtained with sufficient convergence of the objective functional and the volume constraint was satisfied. The flow velocity distribution in the design domain of a 120×120 meshes case is shown in Fig.4.15, where it can be seen that the velocity vector distributions near the wall approach zero, an accurate representation of the fluid-solid interface behavior.

Dependency of optimal configurations on Reynolds number

To test the dependency of optimal configurations on Reynolds numbers set as 5000 and 10000, we use a mesh resolution of 120×120 for both cases. Figure 4.16 indicates that the Reynolds number settings do not significantly affect the optimal configurations for these two Reynolds numbers.

Diffuser problem under developed turbulent flow condition

For the diffuser problem shown in Fig.4.12, the flow channel length is too short to develop the flow in a turbulent condition. In this section, we solve the diffuser problem by assuming a flow channel length of a design domain with $L = 4L_0$ in Fig.4.12, and discuss the turbulent kinetic energy of the obtained optimal configuration.

The velocity, static pressure and turbulent kinetic energy contours are shown for the optimal configuration in Fig.4.17. The convergence history of the objective functional and volume constraint are sufficient to obtain the results shown in Fig.4.18. The optimal configuration has a characteristic shape near the outlet such that the fluid channel shape suddenly converges at the exit. Because of this drastic change in shape near the outlet, the

turbulent kinetic energy becomes high in the area just upstream of the outlet, although the flow velocity and static pressure distribution change gradually there. This means that the flow turbulence that causes energy loss in the flow field becomes high around the outlet, whereas the pressure drop is sufficiently minimized. Therefore, we can conclude that using the total pressure drop as an objective functional will not adequately optimize the turbulence condition.

4.6.3 U-bend pipe

As described below, the flow penetration through the solid domain occurs as long as using the Brinkman penalization method [39, 7, 40]. To determine whether or not flow penetration occurs through a thin wall, we use a two-dimensional U-bend pipe problem, with the design settings shown in Fig.4.19. The flow velocity and pressure are specified as boundary conditions at the inlet and outlet boundaries, respectively, and the inlet and outlet boundaries are distinguished by a thin wall set as a non-design domain. We compare with optimal designs as getting from the topology optimization applying the GCIBM or not. In this numerical example, because the flow separation may occur on the corner of a thin wall, we apply the k-ω turbulence model which has the better accuracy in the prediction of the flow field including the flow separation. The Reynolds number is set as $Re = 10000$ for a turbulent flow regime. The volume constraint is set as $V = 0.5$, and 14080 hexahedral mesh is used in the fixed design domain. The following parameters are set: maximum magnitude of the velocity $\boldsymbol{u}_{\max} = 1$, and the regularization parameter $\tau = 1 \times 10^{-1}$. The turbulence intensity and mixing length are specified as 5% and 0.007 at the inlet boundary, respectively.

The optimization results shown in Fig.4.20 illustrate the different optimal configurations for the proposed GCIBM which is considered or not. In particular, the optimal channel configuration obtained with the GCIBM consists of almost shortest flow path from the inlet to the outlet so as to minimize the pressure loss, while the channel shape outwardly curve

through after the thin wall edge due to the inertia effect under the turbulent condition. On the other hand, the optimal flow channel given by the optimization result without GCIBM is quite different from the optimization result with GCIBM, and the fluid flows along the outer circumference of the design domain with a narrow flow channel. In addition, the objective functional value of the optimal design with the GCIBM is about 0.040, which is quite smaller than the objective functional value, 0.274, without GCIBM.

The velocity vectors and streamlines for these results are shown in Fig.4.20 and Fig.4.21, and indicate that no flow penetrations occurred across the thin wall in the optimal configuration with the GCIBM, although the flow penetration from the inlet to the outlet occurs in the optimization result without the GCIBM.

From this result, we can conclude that the proposed GCIBM is useful method for solving the topology optimization problem with the thin wall.

4.7 Summary

This Chapter presented a level set-based topology optimization method for turbulent flow using the IBM. The presented method was applied to the numerical examples to verify the utility of our proposed optimization method.

The obtained conclusion of this Chapter is as follows.

- In order to deal with the inner wall boundary conditions accurately during the topology optimization of fluid, we constructed the level-set based topology optimization method with GCIBM. In our proposed method, the inner wall boundary conditions could be imposed explicitly on the iso-contour of the LSF.

- The topological derivative was introduced as the sensitivity in the topology optimization, so that the topological change was allowed during the optimization.

- Optimization problems were formulated especially for the pressure drop minimization problem of the channel flows. Governing equations and boundary conditions under the turbulent flow with both k-ϵ and k-ω turbulence models with the wall function were formulated, and the adjoint field was constructed under the frozen turbulence assumption.

- Two numerical examples were examined in this study. The well-known diffuser problem as a numerical example was examined and the utility of the proposed optimization method was confirmed. From the other numerical example with a thin wall, we could obtain the optimal configuration without flow penetration through the thin wall for turbulent regimes. From both results, we could confirmed the utility of our proposed topology optimization method, successfully.

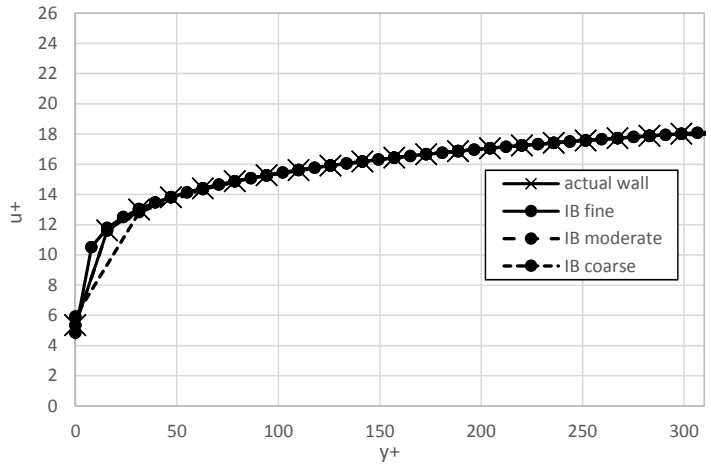

(a) A-A′

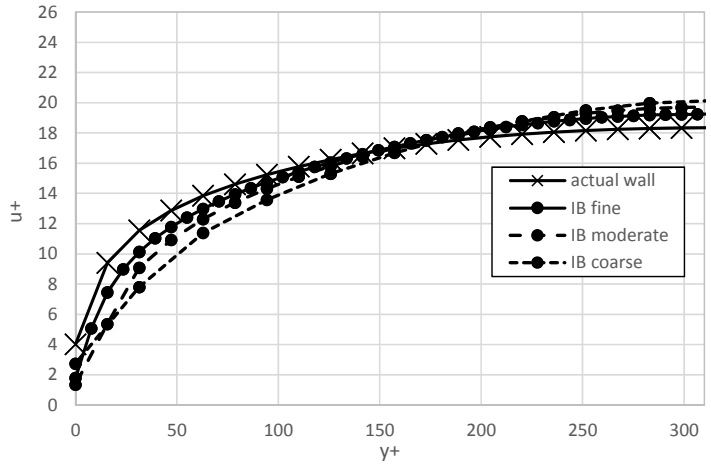

(b) B-B′

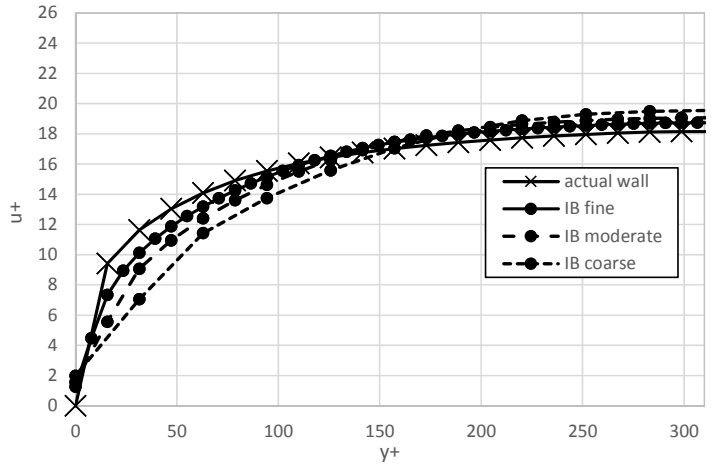

(c) C-C′

Fig. 4.9 Flow velocity profile at A-A′, B-B′ and C-C′ sections for channel flow under k-ϵ turbulence model.

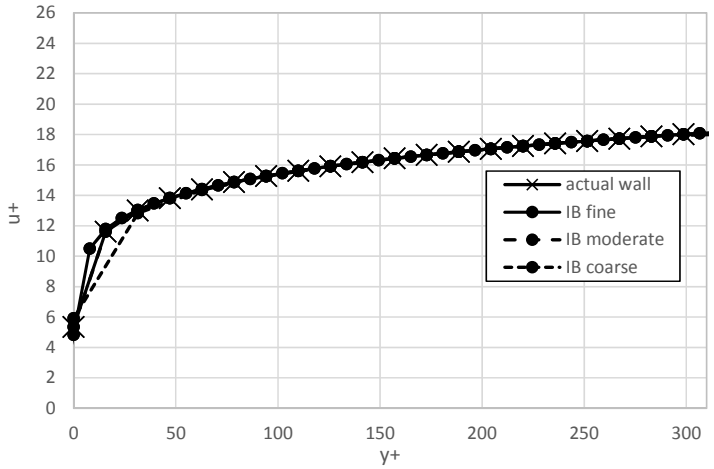

(a) A-A′

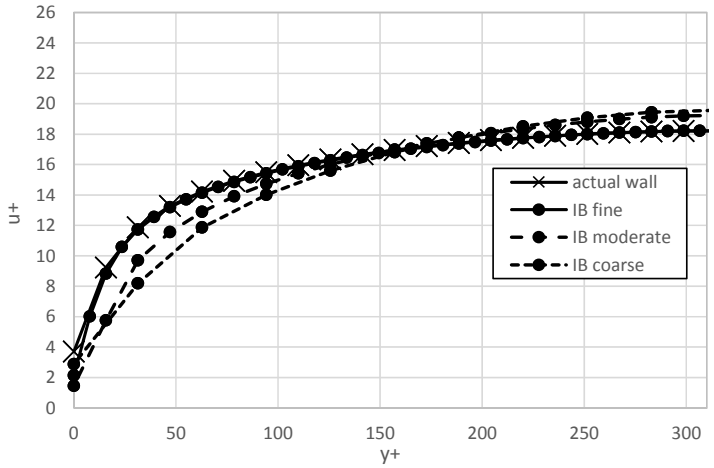

(b) B-B′

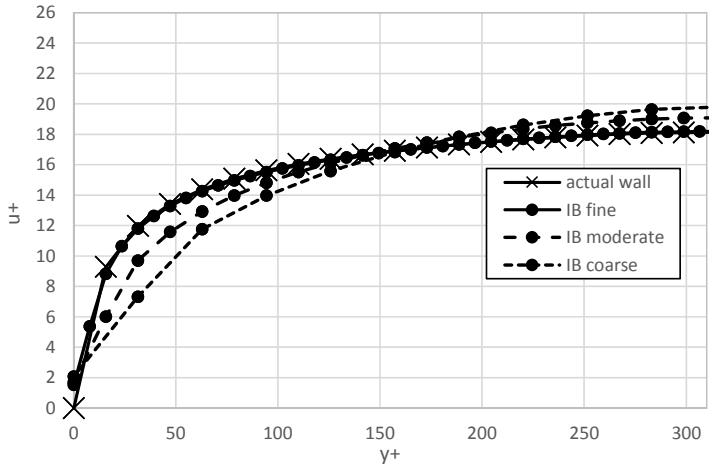

(c) C-C′

Fig. 4.10 Flow velocity profile at A-A′, B-B′ and C-C′ sections for channel flow under k-ω turbulence model.

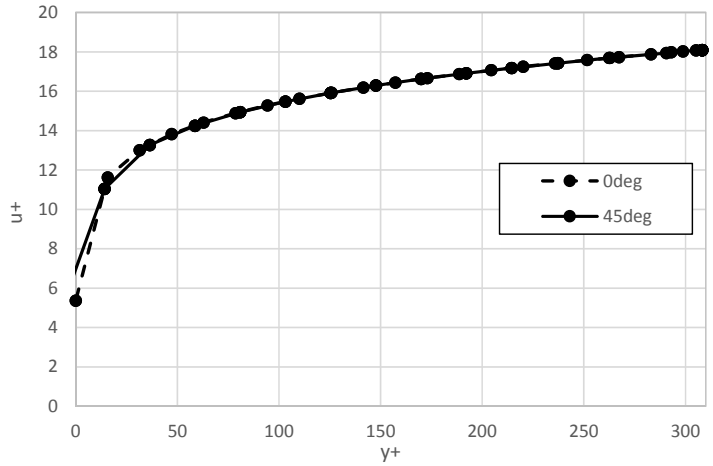

(a) A-A′

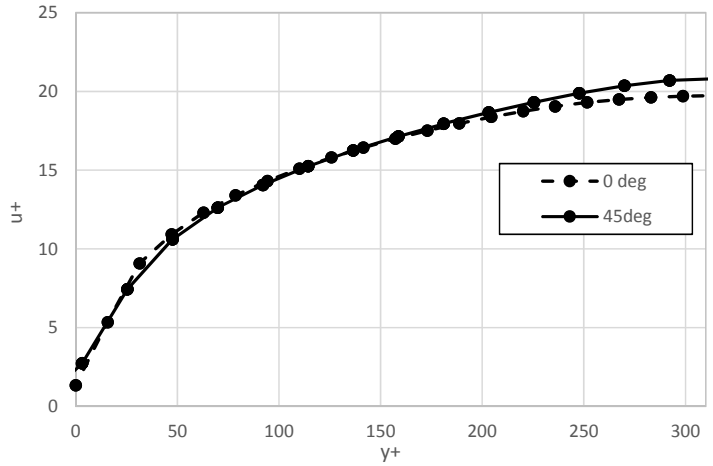

(b) B-B′

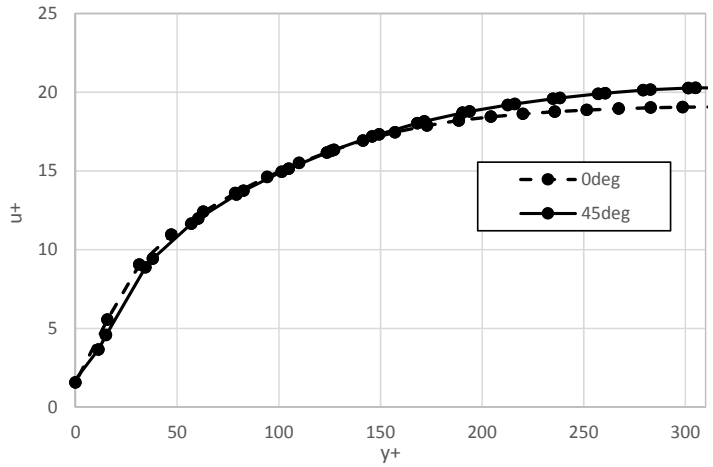

(c) C-C′

Fig. 4.11 Flow velocity profile at A-A′, B-B′ and C-C′ sections compared with inclined meshes for channel flow.

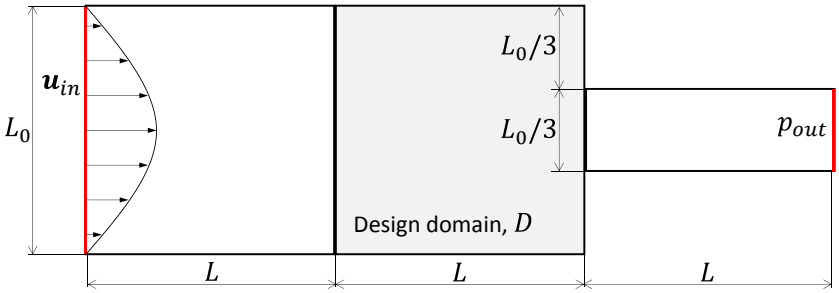

Fig. 4.12 Design settings for diffuser optimization problem.

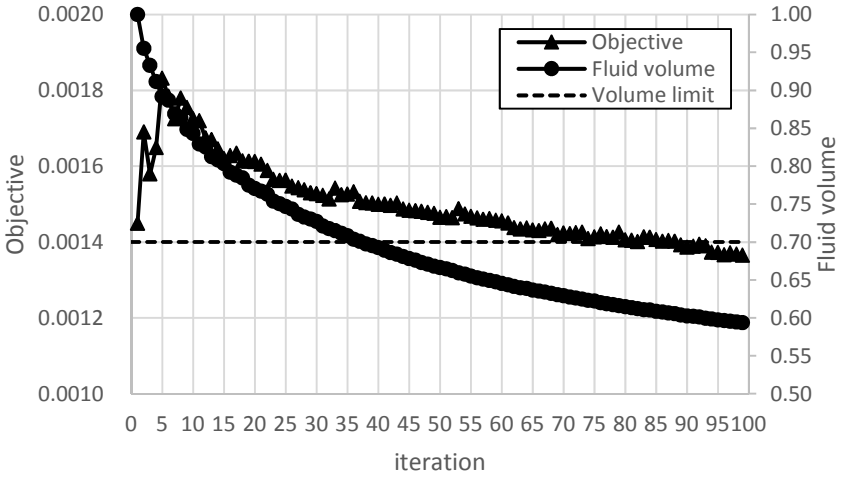

Fig. 4.13 Convergence history of objective and volume constraint functional.

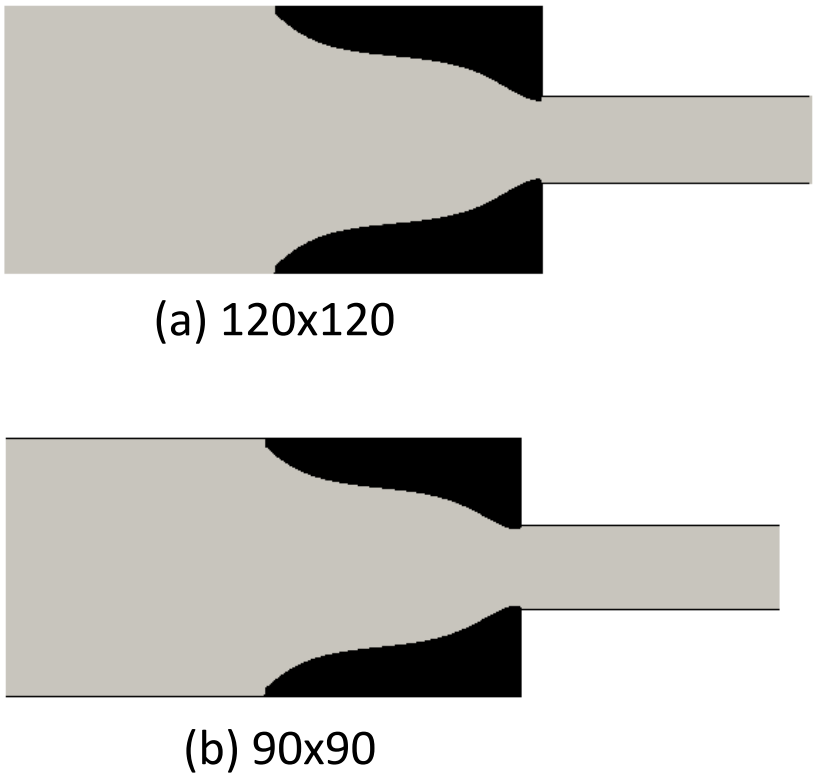

Fig. 4.14 Grid size dependency of optimal configurations.

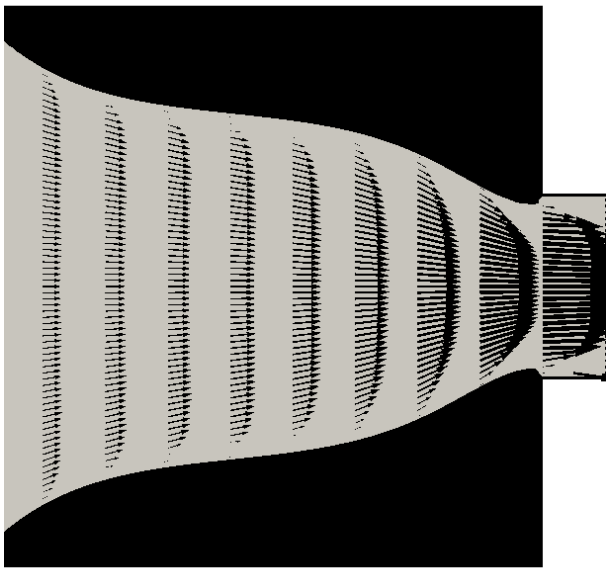

Fig. 4.15 Velocity vector distributions of optimal configuration focusing on the design domain.

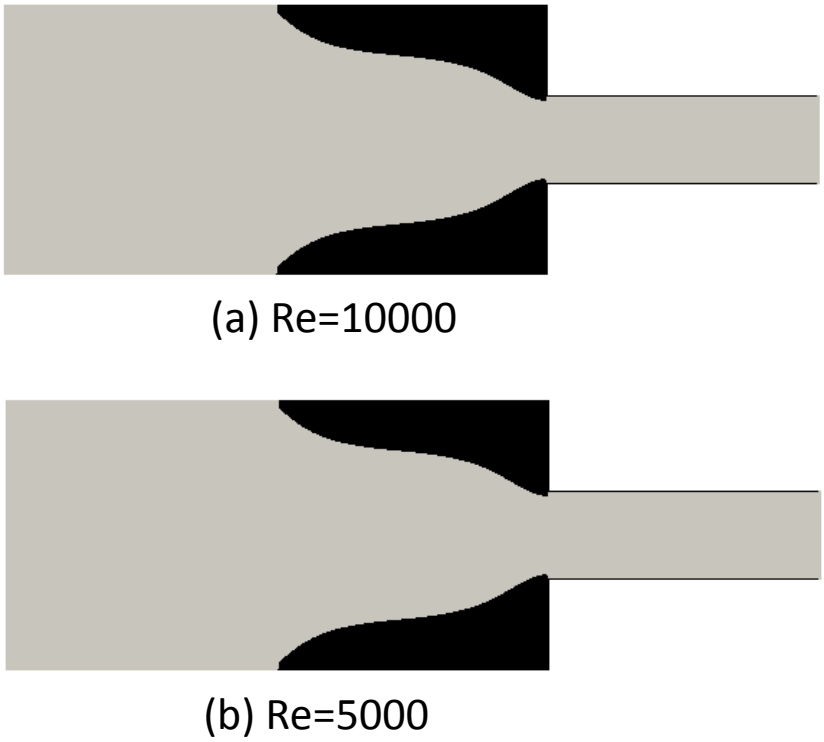

Fig. 4.16 Optimal configurations in different two Reynolds numbers (Re = 5000 and Re = 10000.

(a) Optimal configuration

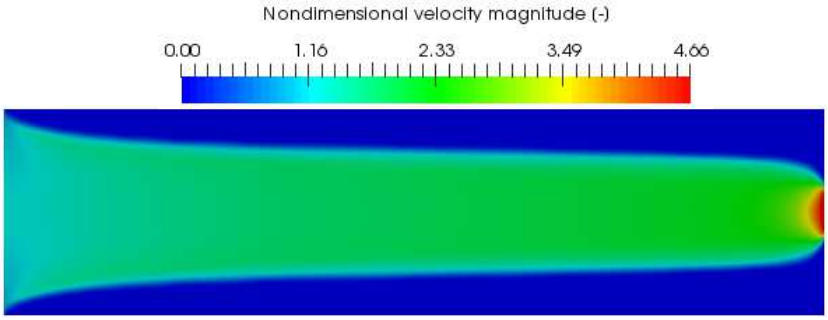

(b) Velocity magnitude

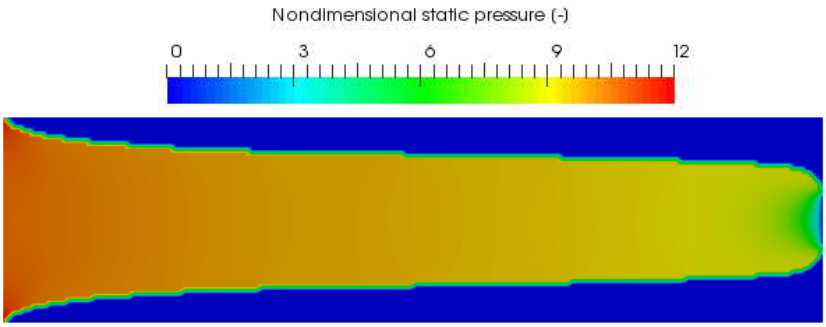

(c) Static pressure

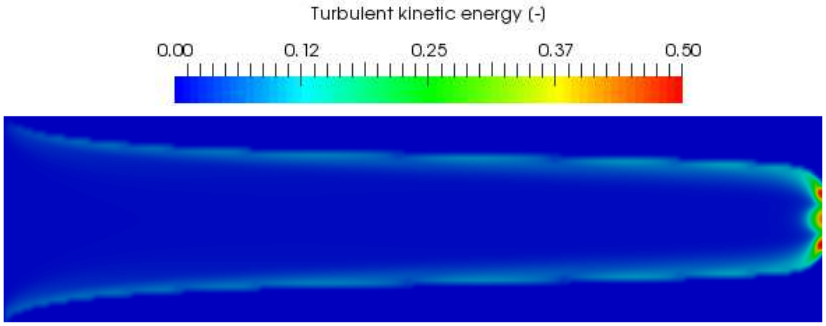

(d) Turbulent kinetic energy

Fig. 4.17 Optimization results in diffuser problem with $L = 4D$ in $Re = 10000$.

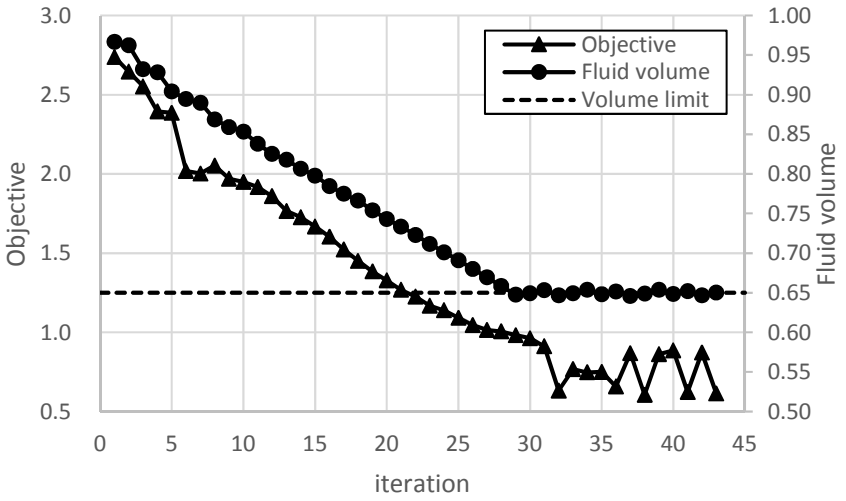

Fig. 4.18 Convergence history of objective and volume constraint functional in k-ϵ turbulence model.

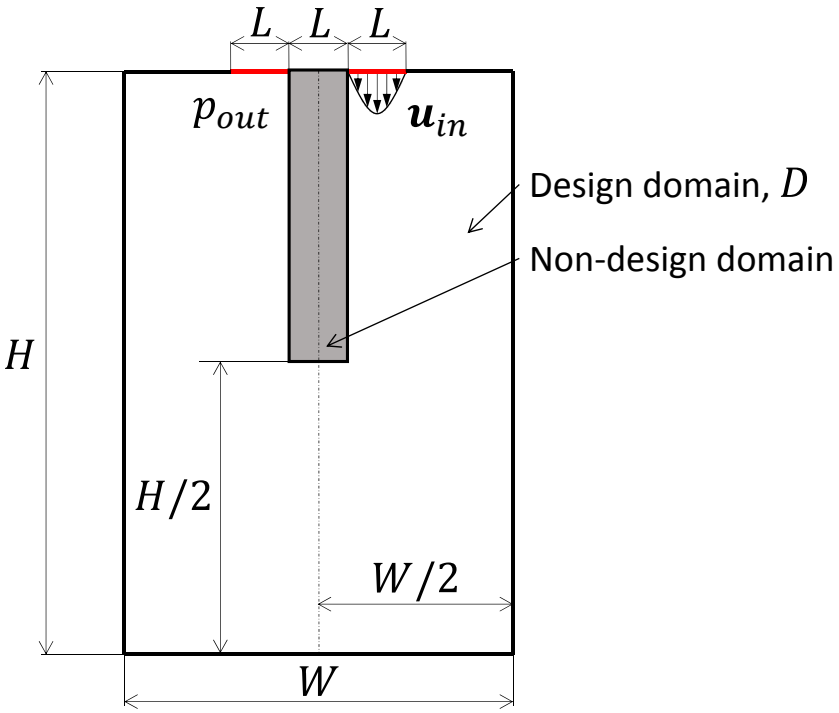

Fig. 4.19 Design settings for U-bend pipe optimization problem.

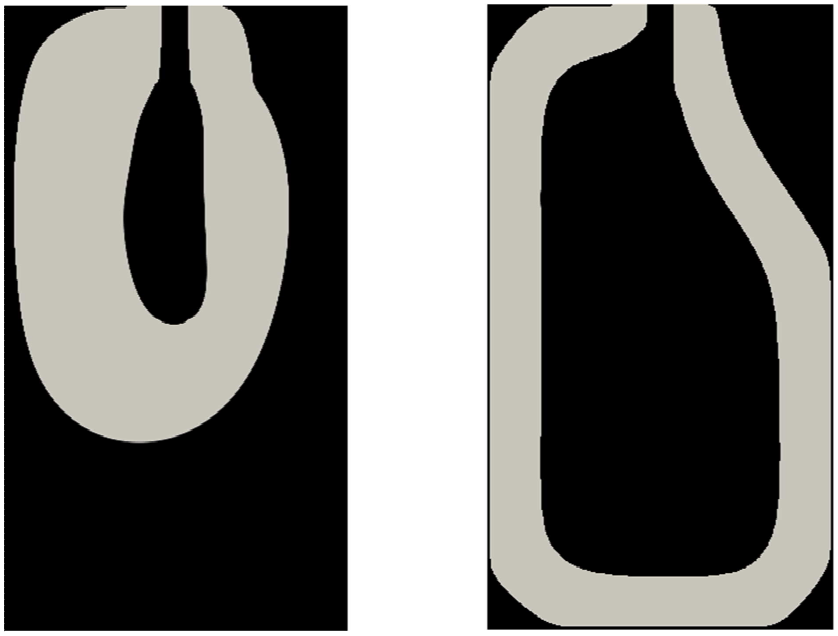

(a) GCIBM (b) Without IBM

Fig. 4.20 Optimal configuration with and without GCIBM.

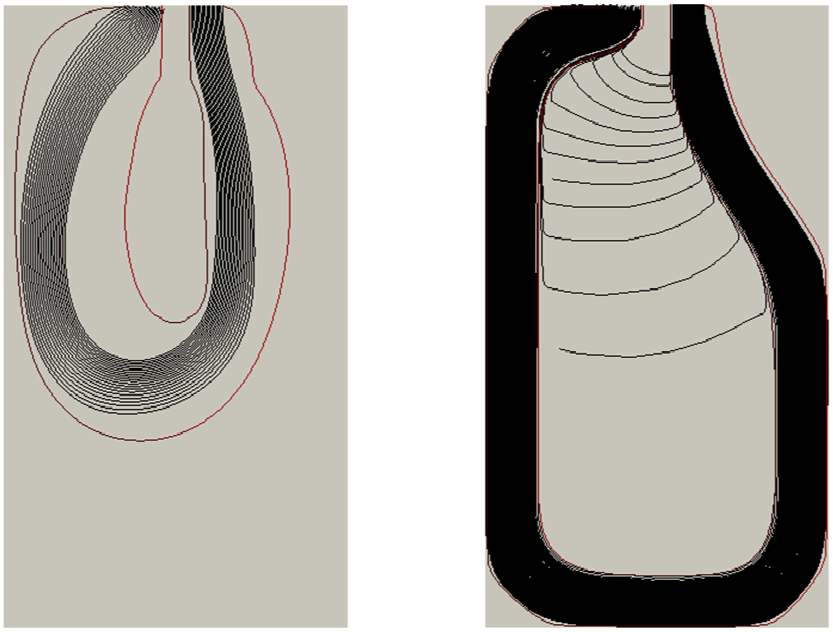

(a) GCIBM (b) Without IBM

Fig. 4.21 Stream lines in the optimal configuration with and without GCIBM.

Chapter 5

General conclusions

The objective of this thesis is to construct the fluid channel design method especially for the multi-terminal laminar flow, and also construct the channel design method for the turbulent flow fields. In Chapter 2, we construct a topology optimization method to minimize the total potential energy of fluids considering the outflow rate constraints. In Chapter 3, we apply our constructed method in Chapter 2 to the manifold design of the plate-type microchannel reactors. In Chapter 4, we focus on a turbulent flow fields, and construct the level set-based topology optimization method using the IBM. The following is a summary of achievements.

In Chapter 2, we proposed a level set-based topology optimization method considering the out flow rate inequality constraints for the design of the MEMS scale multi-terminal fluidic devices. Moreover, to ensure the intended design outflow rate at a designated outlet, the optimization problem includes an outflow rate inequality constraint. In our approach to satisfy the prescribed outflow rate at the designated outlets, we developed the numerical stable way to determine the value of the Lagrange multiplier corresponding to the outflow rate inequality constraints. When the outflow rate inequality constraint is active, the absolute value of the Lagrange multiplier is determined using the introduced exponential function depending on the relative error between the prescribed and actual outflow rate at the designated outlets. In

this way, the determined Lagrange multiplier satisfies the KKT conditions, and the numerical stability is validated successfully from multi-terminal flow problem as a numerical example.

In Chapter 3, we propose an optimal design method for plate-type microchannel reactor manifolds, based on the topology optimization method constructed in Chapter 2. Firstly, we introduced the basic geometry of the plate-type microchannel reactor and presented the representative Z-type and U-type manifolds that are the design objects of this thesis. As for the formulations, we redefined the flow rate inequality constraints for the flow thorough each microchannel, while the outflow rate inequality constraints constructed in Chapter 2 is defined at the designated outlet boundaries. Furthermore, we implemented a flow rate inequality constraint, which constrains the flow rate deviation in each target microchannel to achieve an acceptable degree of flow uniformity. After derivation of the primal and adjoint formulation considering a flow rate inequality constraints, we presented the design problems for Z-type and U-type manifolds for a five-microchannel reactor device, and verified the utility of our proposed optimization method through these numerical examples. Note that although the topological change is not generally occurred in the pressure drop minimization problems, our proposed approach can be simply expanded into complex fluid flow optimization problems, which need to be allowed the topological changes to obtain a promising optimal result.

In Chapter 4, we succeeded in developing a level set-based topology optimization method using the IBM for duct flow problem considering turbulent flow without using the Brinkman penalization approach. The optimization problem to minimize the total potential energy was formulated for the governing equation, which is a RANS with k-ϵ and k-ω turbulence models. And the governing equations are discretized using the finite volume method (FVM), which is normally used in CFD analyses rather than the FEM. In our proposed topology optimization method, a no-slip boundary condition along the fluid-solid interface can be precisely and explicitly imposed, using the GCIBM, a much different approach than the previous Brinkman penalization method in which the fluid-solid interface is expressed as a porosity. To deal

with the topological change in the optimization process, we used the topological derivative as a design sensitivity, so that the no-slip boundary condition is guaranteed to the fluid -solid interface of a newly created obstacles during the evaluation of the topological derivative in an infinitesimally small perturbation. Finally, we presented numerical examples to verify the utility of our proposed optimization method. We could obtain the optimal configurations under the turbulent flow regime up to $Re = 10000$ for duct flow problems. Furthermore, the feasible optimal configurations which has no flow penetration through the thin wall as the non design domain within the fixed design domain could be obtained from the other numerical example. From these results, we could present the validity of our proposed topology optimization method for turbulent flow.

For summary of this thesis, we succeeded in the construction of the duct flow problem in laminar and turbulent flow regimes. It can be expected that the our proposed topology optimization method considering the outflow rate inequality constraints actually applies to the multi-terminal complicated design of the micro fluidic devices. Moreover, the design method of the microchannel reactor manifolds can be utilized to maximize the throughput of the actual microchannel reactors. In the future work, we would like to extend our proposed design method of the microchannel reactors to the situation considering the actual reaction and heat generation from the chemical reaction. For the duct flow problem in turbulent flow condition, we succeeded in developing the topology optimization method using the IBM, and it should be useful for the energy efficient channel design. Regarding the topology optimization in turbulent flow, the concrete adjoint formulation without the frozen turbulence assumption is need to increase the accuracy of dealing with the turbulent flow characteristics, but if it is considered in the topology optimization process, it should be derived the topological derivative with the turbulence models. It should be my future work to be done.

Appendix A

Adjoint formulation of steady incompressible Navier-Stokes flow

In this Appendix A, we provide the details of the sensitivity analysis for the topology optimization for thermoelectric actuator designs. First, we note that the design sensitivity, $\bar{F}'$, is obtained as The topology optimization problem based on level set method for steady state incompressible Navier-Stokes flow can be expressed as follows,

$$\inf_{\phi} \quad J(\boldsymbol{u}, \nabla \boldsymbol{u}, p, \phi) \tag{A.1}$$

$$\text{subject to} \quad F_i(\boldsymbol{u}, p, \phi) = 0 \tag{A.2}$$

$$\boldsymbol{u} = \boldsymbol{u}_{in} \qquad on \quad \Gamma_u \tag{A.3}$$

$$\left(-p \cdot \boldsymbol{I} + \frac{1}{Re} \nabla \boldsymbol{u}\right) \boldsymbol{n} = p_{out} \qquad on \quad \Gamma_p \tag{A.4}$$

$$G \geq 0 \tag{A.5}$$

$$\text{for} \ \ \boldsymbol{u} \in U \ p \in Q \tag{A.6}$$

where $F_i (i = 1, 2)$ mean Navier-Stokes equation and continuity equation, which are described as

$$F_1 \equiv (\boldsymbol{u} \cdot \nabla)\boldsymbol{u} + \nabla p - \frac{1}{Re}\nabla^2 \boldsymbol{u} - \boldsymbol{f} = 0 \tag{A.7}$$

$$F_2 \equiv -\nabla \cdot \boldsymbol{u} = 0 \tag{A.8}$$

, and

$$\boldsymbol{f} = -\alpha \boldsymbol{u} \tag{A.9}$$

$$\alpha = (\alpha_{min} - \alpha_{max})\, H(\phi) + \alpha_{max} \tag{A.10}$$

is introduced as the external force source term of Navier-Stokes equation based on the Darcy law.

The objective functional J is defined as follow,

$$J = \int_\Omega j_\Omega \mathrm{d}\Omega + \int_\Gamma j_\Gamma \mathrm{d}\Gamma \tag{A.11}$$

where j_Ω and j_Γ are the functional defined in the domain Ω and on the implicit boundary Γ, respectively.

The volume constraint functional G is defined as follows,

$$G(\phi) = \int_D H(\phi)\, \mathrm{d}\Omega - V_{max} \tag{A.12}$$

while, V_{max} means the maximum volume of the fluid domain.

From the transformation,

$$\nabla \cdot (A\boldsymbol{B}) = A(\nabla \cdot \boldsymbol{B}) + \nabla A \cdot \boldsymbol{B} \tag{A.13}$$

$$\nabla \cdot \left(\tilde{C}\boldsymbol{B}\right) = \left(\nabla \cdot \tilde{C}^T\right) \cdot \boldsymbol{B} + \left(\tilde{C}^T : \nabla \boldsymbol{B}\right) \tag{A.14}$$

where A, $\boldsymbol{B}$ and $\tilde{C}$ mean scalar, vector and tensor value, respectively, the Lagrangian L can be expressed as follows by using the Lagrange undefined multipliers $\boldsymbol{v}$, q and λ.

$$\begin{aligned} L &= J + \int_D \boldsymbol{v} \cdot F_1 \mathrm{d}\Omega + \int_D q F_2 \mathrm{d}\Omega + \lambda_j G_j \\ &= J + \int_D (\boldsymbol{u} \cdot \nabla)\boldsymbol{u} \cdot \boldsymbol{v} \mathrm{d}\Omega + \int_D \nabla p \cdot \boldsymbol{v} \mathrm{d}\Omega - \frac{1}{Re}\int_D \nabla^2 \boldsymbol{u} \cdot \boldsymbol{v} \mathrm{d}\Omega + \int_D \alpha \boldsymbol{u} \cdot \boldsymbol{v} \mathrm{d}\Omega \\ &\quad - \int_D (\nabla \cdot \boldsymbol{u}) q \mathrm{d}\Omega + \lambda G(\phi) \end{aligned} \tag{A.15}$$

$$\begin{aligned} &= J + \int_D (\boldsymbol{u} \cdot \nabla)\boldsymbol{u} \cdot \boldsymbol{v} \mathrm{d}\Omega + \int_D \nabla \cdot (p\boldsymbol{v}) \mathrm{d}\Omega - \int_D p(\nabla \cdot \boldsymbol{v}) \mathrm{d}\Omega \\ &\quad - \frac{1}{Re}\int_D \nabla \cdot (\nabla \boldsymbol{u} \cdot \boldsymbol{v}) \mathrm{d}\Omega + \frac{1}{Re}\int_D \nabla \boldsymbol{u} \nabla \boldsymbol{v} \mathrm{d}\Omega + \int_D \alpha \boldsymbol{u} \cdot \boldsymbol{v} \mathrm{d}\Omega \\ &\quad - \int_D \nabla \cdot (q\boldsymbol{u}) \mathrm{d}\Omega + \int_D \nabla q \cdot \boldsymbol{u} \mathrm{d}\Omega + \lambda G(\phi) \end{aligned} \tag{A.16}$$

Based on the Gauss' divergence theorem, the following transformation is obtained.

$$\begin{aligned} L = J &+ \int_D (\boldsymbol{u} \cdot \nabla)\boldsymbol{u} \cdot \boldsymbol{v} \mathrm{d}\Omega + \int_\Gamma p\boldsymbol{v} \cdot \boldsymbol{n} \mathrm{d}\Gamma - \int_D p(\nabla \cdot \boldsymbol{v}) \mathrm{d}\Omega \\ &- \frac{1}{Re}\int_\Gamma (\nabla \boldsymbol{u} \cdot \boldsymbol{v})\boldsymbol{n} \mathrm{d}\Gamma + \frac{1}{Re}\int_D \nabla \boldsymbol{u} \nabla \boldsymbol{v} \mathrm{d}\Omega + \int_D \alpha \boldsymbol{u} \cdot \boldsymbol{v} \mathrm{d}\Omega \\ &- \int_\Gamma q\boldsymbol{u} \cdot \boldsymbol{n} \mathrm{d}\Gamma + \int_D \nabla q \cdot \boldsymbol{u} \mathrm{d}\Omega + \lambda G(\phi) \end{aligned} \tag{A.17}$$

According to the variational of L, $L+\delta L$ is expressed as follows.

$$\begin{aligned}
L+\delta L = J &+ \frac{\partial J}{\partial \phi}\cdot\delta\phi + \frac{\partial J}{\partial \boldsymbol{u}}\cdot\delta\boldsymbol{u} + \frac{\partial J}{\partial \nabla \boldsymbol{u}} : \nabla(\delta\boldsymbol{u}) + \frac{\partial J}{\partial p}\cdot\delta p \\
&+ \int_D ((\boldsymbol{u}\cdot\nabla)\boldsymbol{u} + (\delta\boldsymbol{u}\cdot\nabla)\boldsymbol{u} + (\boldsymbol{u}\cdot\nabla)\delta\boldsymbol{u})\cdot\boldsymbol{v}\mathrm{d}\Omega \\
&+ \int_\Gamma (p+\delta p)\boldsymbol{v}\cdot\boldsymbol{n}\mathrm{d}\Gamma - \int_D (p+\delta p)(\nabla\cdot\boldsymbol{v})\mathrm{d}\Omega \\
&- \frac{1}{Re}\int_\Gamma (\nabla(\delta\boldsymbol{u})\cdot\boldsymbol{v} + \nabla\boldsymbol{u}\cdot\boldsymbol{v})\boldsymbol{n}\mathrm{d}\Gamma + \frac{1}{Re}\int_D (\nabla(\delta\boldsymbol{u}) + \nabla\boldsymbol{u})\nabla\boldsymbol{v}\mathrm{d}\Omega \\
&+ \int_D \left(\alpha + \frac{\partial\alpha}{\partial\phi}\cdot\delta\phi\right)(\boldsymbol{u}+\delta\boldsymbol{u})\cdot\boldsymbol{v}\mathrm{d}\Omega \\
&- \int_\Gamma q(\boldsymbol{u}+\delta\boldsymbol{u})\cdot\boldsymbol{n}\mathrm{d}\Gamma + \int_D \nabla q\cdot(\boldsymbol{u}+\delta\boldsymbol{u})\mathrm{d}\Omega + \lambda\left(G(\phi) + \frac{\partial G}{\partial\phi}\cdot\delta\phi\right)
\end{aligned} \tag{A.18}$$

Thus, the following derivative of L subject to the levelset functional ϕ can be obtained.

$$\begin{aligned}
\delta L = &\frac{\partial J}{\partial \phi}\cdot\delta\phi + \frac{\partial J}{\partial \boldsymbol{u}}\cdot\delta\boldsymbol{u} + \frac{\partial J}{\partial \nabla \boldsymbol{u}} : \nabla(\delta\boldsymbol{u}) + \frac{\partial J}{\partial p}\cdot\delta p \\
&+ \int_D ((\delta\boldsymbol{u}\cdot\nabla)\boldsymbol{u} + (\boldsymbol{u}\cdot\nabla)\delta\boldsymbol{u})\cdot\boldsymbol{v}\mathrm{d}\Omega + \int_\Gamma \delta p\boldsymbol{v}\cdot\boldsymbol{n}\mathrm{d}\Gamma - \int_D \delta p(\nabla\cdot\boldsymbol{v})\mathrm{d}\Omega \\
&- \frac{1}{Re}\int_\Gamma (\nabla(\delta\boldsymbol{u})\cdot\boldsymbol{v})\boldsymbol{n}\mathrm{d}\Gamma + \frac{1}{Re}\int_D (\nabla(\delta\boldsymbol{u}))\nabla\boldsymbol{v}\mathrm{d}\Omega \\
&+ \int_D \left(\alpha\delta\boldsymbol{u} + \frac{\partial\alpha}{\partial\phi}\cdot\delta\phi\boldsymbol{u}\right)\cdot\boldsymbol{v}\mathrm{d}\Omega - \int_\Gamma q\delta\boldsymbol{u}\cdot\boldsymbol{n}\mathrm{d}\Gamma + \int_D \nabla q\cdot\delta\boldsymbol{u}\mathrm{d}\Omega + \lambda\left(\frac{\partial G}{\partial\phi}\cdot\delta\phi\right)
\end{aligned} \tag{A.19}$$

And the convection term can be transformed as below.

$$\begin{aligned}
&\int_D ((\delta\boldsymbol{u}\cdot\nabla)\boldsymbol{u} + (\boldsymbol{u}\cdot\nabla)\delta\boldsymbol{u})\cdot\boldsymbol{v}\mathrm{d}\Omega \\
&\quad = \int_D (\nabla\boldsymbol{u})\boldsymbol{v}\cdot\delta\boldsymbol{u}\mathrm{d}\Omega + \int_D \nabla\cdot(\boldsymbol{u}\cdot(\boldsymbol{v}\cdot\delta\boldsymbol{u}))\mathrm{d}\Omega - \int_D (\boldsymbol{u}\cdot\nabla)\boldsymbol{v}\cdot\delta\boldsymbol{u}\mathrm{d}\Omega
\end{aligned} \tag{A.20}$$

Additionally, because p can be expressed by $\nabla \boldsymbol{u}$ on Γ, the derivation of J subject to $\nabla \boldsymbol{u}$ can be transformed as below (using Eq.(A.14)).

$$\begin{aligned}\frac{\partial J}{\partial \nabla \boldsymbol{u}} : \nabla(\delta \boldsymbol{u}) &= \int_{\Omega} \left(\frac{\partial j_{\Omega}}{\partial \nabla \boldsymbol{u}} : \nabla(\delta \boldsymbol{u}) \right) \mathrm{d}\Omega \\ &= \int_{\Omega} \nabla \cdot \left(\frac{\partial j_{\Omega}}{\partial \nabla \boldsymbol{u}} \cdot \delta \boldsymbol{u} \right) \mathrm{d}\Omega - \int_{\Omega} \left(\nabla \cdot \frac{\partial j_{\Omega}}{\partial \nabla \boldsymbol{u}} \right) \cdot \delta \boldsymbol{u} \mathrm{d}\Omega \end{aligned} \tag{A.21}$$

Then, based on the partial integration approach and the Gauss' divergence theorem, the following transformation is obtained.

$$\begin{aligned}\delta L = & \frac{\partial J}{\partial \phi} \cdot \delta \phi + \frac{\partial J}{\partial \boldsymbol{u}} \cdot \delta \boldsymbol{u} + \frac{\partial J}{\partial p} \cdot \delta p + \int_{\Gamma} \left(\frac{\partial j_{\Omega}}{\partial \nabla \boldsymbol{u}} \cdot \boldsymbol{n} \right) \cdot \delta \boldsymbol{u} \mathrm{d}\Gamma - \int_{\Omega} \left(\nabla \cdot \frac{\partial j_{\Omega}}{\partial \nabla \boldsymbol{u}} \right) \cdot \delta \boldsymbol{u} \mathrm{d}\Omega \\ & + \int_{D} (\nabla \boldsymbol{u}) \boldsymbol{v} \cdot \delta \boldsymbol{u} \mathrm{d}\Omega + \int_{\Gamma} (\boldsymbol{u} \cdot \boldsymbol{n}) \boldsymbol{v} \cdot \delta \boldsymbol{u} \mathrm{d}\Gamma - \int_{D} (\boldsymbol{u} \cdot \nabla) \boldsymbol{v} \cdot \delta \boldsymbol{u} \mathrm{d}\Omega \\ & + \int_{\Gamma} \delta p \boldsymbol{v} \cdot \boldsymbol{n} \mathrm{d}\Gamma - \int_{D} \delta p (\nabla \cdot \boldsymbol{v}) \mathrm{d}\Omega \\ & - \frac{1}{Re} \int_{\Gamma} (\nabla(\delta \boldsymbol{u}) \cdot \boldsymbol{v}) \boldsymbol{n} \mathrm{d}\Gamma + \frac{1}{Re} \int_{\Gamma} \delta \boldsymbol{u} \nabla \boldsymbol{v} \cdot \boldsymbol{n} \mathrm{d}\Gamma - \frac{1}{Re} \int_{D} \delta \boldsymbol{u} \left(\nabla^2 \boldsymbol{v} \right) \mathrm{d}\Omega \\ & + \int_{D} \left(\alpha \delta \boldsymbol{u} + \frac{\partial \alpha}{\partial \phi} \cdot \delta \phi \boldsymbol{u} \right) \cdot \boldsymbol{v} \mathrm{d}\Omega - \int_{\Gamma} q \delta \boldsymbol{u} \cdot \boldsymbol{n} \mathrm{d}\Gamma + \int_{D} \nabla q \cdot \delta \boldsymbol{u} \mathrm{d}\Omega + \lambda \left(\frac{\partial G}{\partial \phi} \cdot \delta \phi \right) \end{aligned} \tag{A.22}$$

Because $\boldsymbol{u}$ and p are known on Γ_u and Γ_p, respectively, th following conditions can be expressed on the boundary.

$$\Gamma = \Gamma_u \cup \Gamma_p$$

$$\begin{cases} \delta \boldsymbol{u} = 0 & on \ \ \Gamma_u \\ \delta p = 0 & on \ \ \Gamma_p \end{cases} \tag{A.23}$$

Therefore, by inserting the above conditions, the following transformation can be obtained.

$$\begin{aligned}
\delta L = & \frac{\partial J}{\partial \phi}\cdot\delta\phi + \int_\Omega \left(\frac{\partial j_\Omega}{\partial \boldsymbol{u}}\cdot\delta\boldsymbol{u} - \left(\nabla\cdot\frac{\partial j_\Omega}{\partial \nabla\boldsymbol{u}}\right)\cdot\delta\boldsymbol{u} + \frac{\partial j_\Omega}{\partial p}\cdot\delta p\right)\mathrm{d}\Omega \\
& + \int_{\Gamma_u} \frac{\partial j_\Gamma}{\partial p}\cdot\delta p\mathrm{d}\Gamma + \int_{\Gamma_p}\left(\frac{\partial j_\Gamma}{\partial \boldsymbol{u}} + \frac{\partial j_\Omega}{\partial \nabla\boldsymbol{u}}\cdot\boldsymbol{n}\right)\cdot\delta\boldsymbol{u}\mathrm{d}\Gamma \\
& + \int_D (\nabla\boldsymbol{u})\,\boldsymbol{v}\cdot\delta\boldsymbol{u}\mathrm{d}\Omega + \int_{\Gamma_p}(\boldsymbol{u}\cdot\boldsymbol{n})\,\boldsymbol{v}\cdot\delta\boldsymbol{u}\mathrm{d}\Gamma - \int_D (\boldsymbol{u}\cdot\nabla)\,\boldsymbol{v}\cdot\delta\boldsymbol{u}\mathrm{d}\Omega \\
& + \int_{\Gamma_u}\delta p\boldsymbol{v}\cdot\boldsymbol{n}\mathrm{d}\Gamma - \int_D \delta p\,(\nabla\cdot\boldsymbol{v})\,\mathrm{d}\Omega + \frac{1}{Re}\int_{\Gamma_p}\delta\boldsymbol{u}\nabla\boldsymbol{v}\cdot\boldsymbol{n}\mathrm{d}\Gamma - \frac{1}{Re}\int_D \delta\boldsymbol{u}\left(\nabla^2\boldsymbol{v}\right)\mathrm{d}\Omega \\
& + \int_D\left(\alpha\delta\boldsymbol{u} + \frac{\partial\alpha}{\partial\phi}\cdot\delta\phi\boldsymbol{u}\right)\cdot\boldsymbol{v}\mathrm{d}\Omega - \int_{\Gamma_p} q\delta\boldsymbol{u}\cdot\boldsymbol{n}\mathrm{d}\Gamma + \int_D \nabla q\cdot\delta\boldsymbol{u}\mathrm{d}\Omega + \lambda\left(\frac{\partial G}{\partial\phi}\cdot\delta\phi\right)\Big|_\Omega \qquad \text{(A.24)} \\
= & \int_\Omega\left(\frac{\partial j_\Omega}{\partial\boldsymbol{u}} - \nabla\cdot\frac{\partial j_\Omega}{\partial\nabla\boldsymbol{u}} - \frac{1}{Re}\nabla^2\boldsymbol{v} - (\boldsymbol{u}\cdot\nabla)\,\boldsymbol{v} + (\nabla\boldsymbol{u})\cdot\boldsymbol{v} + \alpha\boldsymbol{v} + \nabla q\right)\delta\boldsymbol{u}\mathrm{d}\Omega \\
& + \int_\Omega\left(-\nabla\cdot\boldsymbol{v} + \frac{\partial j_\Omega}{\partial p}\right)\delta p\mathrm{d}\Omega + \int_{\Gamma_p}\left(\frac{\partial j_\Omega}{\partial\nabla\boldsymbol{u}}\cdot\boldsymbol{n} + \frac{\partial j_\Gamma}{\partial\boldsymbol{u}} - q\cdot\boldsymbol{n} + \frac{1}{Re}\nabla\boldsymbol{v}\cdot\boldsymbol{n} + (\boldsymbol{u}\cdot\boldsymbol{n})\cdot\boldsymbol{v}\right)\delta\boldsymbol{u}\mathrm{d}\Gamma \\
& + \int_{\Gamma_u}\left(\frac{\partial j_\Gamma}{\partial p} + \boldsymbol{v}\cdot\boldsymbol{n}\right)\delta p\mathrm{d}\Gamma + \int_D\left(\frac{\partial\alpha}{\partial\phi}\cdot\delta\phi\boldsymbol{u}\right)\cdot\boldsymbol{v}\mathrm{d}\Omega + \frac{\partial J}{\partial\phi}\cdot\delta\phi + \lambda\left(\frac{\partial G}{\partial\phi}\cdot\delta\phi\right) \qquad \text{(A.25)}
\end{aligned}$$

Thus, adjoint equation and boundary condition can be written as,

$$-\frac{1}{Re}\nabla^2\boldsymbol{v} - (\boldsymbol{u}\cdot\nabla)\,\boldsymbol{v} + (\nabla\boldsymbol{u})\cdot\boldsymbol{v} + \nabla q = -\alpha\boldsymbol{v} - \left(\frac{\partial j_\Omega}{\partial\boldsymbol{u}} - \nabla\cdot\frac{\partial j_\Omega}{\partial\nabla\boldsymbol{u}}\right) \qquad \text{(A.26)}$$

$$-\nabla\cdot\boldsymbol{v} = -\frac{\partial j_\Omega}{\partial p} \qquad \text{(A.27)}$$

$$\left(-q\cdot\boldsymbol{I} + \frac{1}{Re}\nabla\boldsymbol{v}\right)\cdot\boldsymbol{n} = -(\boldsymbol{u}\cdot\boldsymbol{n})\cdot\boldsymbol{v} - \frac{\partial j_\Gamma}{\partial\boldsymbol{u}} - \frac{\partial j_\Omega}{\partial\nabla\boldsymbol{u}}\boldsymbol{n} \qquad on \quad \Gamma_p \qquad \text{(A.28)}$$

$$\boldsymbol{v}\cdot\boldsymbol{n} = -\frac{\partial j_\Gamma}{\partial p} \qquad on \quad \Gamma_u \qquad \text{(A.29)}$$

Finally, the shape sensitivity for topology optimization problem can be obtained as,

$$\delta L = \left\{\int_D \frac{\partial j_\Omega}{\partial\phi}\mathrm{d}\Omega + \int_\Gamma \frac{\partial j_\Gamma}{\partial\phi}\mathrm{d}\Gamma + \int_D\left(\frac{\partial\alpha}{\partial\phi}\boldsymbol{u}\cdot\boldsymbol{v}\right)\mathrm{d}\Omega + \lambda\frac{\partial G}{\partial\phi}\right\}\delta\phi \qquad \text{(A.30)}$$

Appendix B

Sensitivity analysis for variety of objective functionals

B.1 Objective functionals

B.1.1 Viscous dissipation rate

Here, we discuss the details concerning the derivation of the adjoint equations of nanoscale heat conduction problems. The adjoint equations, boundary and initial conditions can be obtained through computing the optimality condition, Eq. (**??**). First, using integration by parts with respect to time t and spatial vector $\boldsymbol{x}$, the stationary points related to the global variables $\tilde{f}_A(t,\boldsymbol{x},\boldsymbol{\xi})$ and $\tilde{f}_B(t,\boldsymbol{x},\boldsymbol{\xi})$ are obtained as follows:

$$j_\Omega = \frac{1}{2Re}\left\{\nabla\boldsymbol{u} + (\nabla\boldsymbol{u})^{\mathrm{T}}\right\} : \left\{\nabla\boldsymbol{u} + (\nabla\boldsymbol{u})^{\mathrm{T}}\right\} + \alpha\boldsymbol{u}\cdot\boldsymbol{u} \tag{B.1}$$

$$j_\Gamma = 0 \tag{B.2}$$

In the following, concern between viscous dissipation rate and the total pressure loss is discussed.

The total kinetic energy of an incompressible fluid is

$$E = \frac{1}{2}\int_{\Omega} \boldsymbol{u}^2 \mathrm{d}\Omega \tag{B.3}$$

B.1.2 Swirl number

$$j_{\Omega} = 0 \tag{B.4}$$

$$j_{\Gamma} = S_w = \frac{T}{rW} \tag{B.5}$$

Swirl number S_w can be defined using T, W and r, which are the rotational moment of kinetic momentum, axial kinetic momentum and characteristic length, respectively. Generally, the hydraulic diameter is used as r.

$$r = \frac{4A}{L} \tag{B.6}$$

with the evaluation surface area A and the sectional length L, which is defined as sum of all-sides composed of the rectangle. T and W are defined as below.

$$T = \boldsymbol{u}_{ax}\left(\boldsymbol{r} \times \boldsymbol{u}_{tg}\right) \tag{B.7}$$

$$W = {\boldsymbol{u}_{ax}}^2 \tag{B.8}$$

while $\boldsymbol{u}_{ax}$ and $\boldsymbol{u}_{tg}$ means the axial and tangential velocity, and $\boldsymbol{r} := (\boldsymbol{x} - \boldsymbol{x}_0)$ is the swirl distance vector to the defined origin $\boldsymbol{x}_0$ then

$$\boldsymbol{r} \times \boldsymbol{u} = \begin{vmatrix} \boldsymbol{i} & \boldsymbol{j} & \boldsymbol{k} \\ x - x_0 & y - y_0 & z - z_0 \\ u & v & w \end{vmatrix} = \begin{pmatrix} (y - y_0)\, w - (z - z_0)\, v \\ (z - z_0)\, u - (x - x_0)\, w \\ (x - x_0)\, v - (y - y_0)\, u \end{pmatrix} \tag{B.9}$$

The rotational moment of kinetic momentum of $\boldsymbol{u}_{ax}\left(\boldsymbol{r}\times\boldsymbol{u}_{tg}\right)$ can be described as below.

$$\begin{aligned}\boldsymbol{u}_{ax}\left(\boldsymbol{r}\times\boldsymbol{u}_{tg}\right) &= \begin{pmatrix} u \\ v \\ w \end{pmatrix} \cdot \begin{pmatrix} (y-y_0)\,w-(z-z_0)\,v \\ (z-z_0)\,u-(x-x_0)\,w \\ (x-x_0)\,v-(y-y_0)\,u \end{pmatrix} \\ &= u\{(y-y_0)\,w-(z-z_0)\,v\}+v\{(z-z_0)\,u-(x-x_0)\,w\}+w\{(x-x_0)\,v-(y-y_0)\,u\}\end{aligned} \tag{B.10}$$

If the x-y plane is the specific outlet plane and the z direction is the rotational axis for the defined objective functional j_Γ, then the axial velocity $\boldsymbol{u}_{ax}$ becomes

$$\boldsymbol{u}_{ax} = \begin{pmatrix} 0 \\ 0 \\ w \end{pmatrix} \tag{B.11}$$

Then, the objective functional can be transformed into simpler formulation as below for the origin $\boldsymbol{x}_0 := (0,0,0)$,

$$j_\Gamma = \frac{xv-yu}{w} \tag{B.12}$$

in which the characteristic length $r = 1$ is used.

B.2 The adjoint problem and topological sensitivity

B.2.1 Viscous dissipation rate minimization problem

The objective functional is as follows,

$$j_\Omega = \frac{1}{2Re}\left\{\nabla \boldsymbol{u} + (\nabla \boldsymbol{u})^{\mathrm{T}}\right\} : \left\{\nabla \boldsymbol{u} + (\nabla \boldsymbol{u})^{\mathrm{T}}\right\} + \alpha \boldsymbol{u} \cdot \boldsymbol{u} \tag{B.13}$$

$$j_\Gamma = 0 \tag{B.14}$$

each derivative of j_Ω and j_Γ for adjoint equation and boundary condition are described below,

$$\begin{cases} \dfrac{\partial j_\Omega}{\partial \boldsymbol{u}} = \dfrac{1}{Re}\nabla^2 \boldsymbol{u} + 2\alpha \boldsymbol{u} \\ \dfrac{\partial j_\Omega}{\partial \nabla \boldsymbol{u}} = \dfrac{2}{Re}\nabla \boldsymbol{u} \\ \dfrac{\partial j_\Omega}{\partial p} = 0 \\ \dfrac{\partial j_\Gamma}{\partial p} = 0 \\ \dfrac{\partial j_\Gamma}{\partial \boldsymbol{u}} = 0 \end{cases} \tag{B.15}$$

Then, by substituting each derivative, the adjoint equation and boundary condition for the flow rate constraint problem can be obtained as,

$$-\frac{1}{Re}\nabla^2 \boldsymbol{v} - (\boldsymbol{u} \cdot \nabla)\boldsymbol{v} + (\nabla \boldsymbol{u}) \cdot \boldsymbol{v} + \nabla q = -\alpha \boldsymbol{v} - \left(\frac{1}{Re}\nabla^2 \boldsymbol{u} + 2\alpha \boldsymbol{u} - \nabla \cdot \frac{2}{Re}\nabla \boldsymbol{u}\right) \tag{B.16}$$

$$-\nabla \cdot \boldsymbol{v} = 0 \tag{B.17}$$

$$\left(-q \cdot \boldsymbol{I} + \frac{1}{Re}\nabla \boldsymbol{v}\right) \cdot \boldsymbol{n} = -(\boldsymbol{u} \cdot \boldsymbol{n}) \cdot \boldsymbol{v} - \frac{2}{Re}\nabla \boldsymbol{u} \cdot \boldsymbol{n} \quad on \quad \Gamma_p \tag{B.18}$$

$$\boldsymbol{v} \cdot \boldsymbol{n} = 0 \qquad on \quad \Gamma_u \tag{B.19}$$

Consequently, as the each derivative with respect to the level set functional ϕ are

$$\begin{cases} \dfrac{\partial j_\Omega}{\partial \phi} = (\alpha_{min} - \alpha_{max})\,\boldsymbol{u}\cdot\boldsymbol{u} \\ \dfrac{\partial j_\Gamma}{\partial \phi} = 0 \\ \dfrac{\partial \alpha}{\partial \phi} = \alpha_{min} - \alpha_{max} \\ \dfrac{\partial G}{\partial \phi} = 1 \end{cases} \tag{B.20}$$

the shape sensitivity for topology optimization problem can be obtained as,

$$\begin{aligned} \delta L &= \left\{ \int_D \frac{\partial j_\Omega}{\partial \phi} \mathrm{d}\Omega + \int_\Gamma \frac{\partial j_\Gamma}{\partial \phi} \mathrm{d}\Gamma + \int_D \left(\frac{\partial \alpha}{\partial \phi} \boldsymbol{u}\cdot\boldsymbol{v} \right) \mathrm{d}\Omega + \lambda \frac{\partial G}{\partial \phi} \right\} \delta\phi \\ &= \int_D \left\{ (\alpha_{min} - \alpha_{max}) \left(\boldsymbol{u}^2 + \boldsymbol{u}\boldsymbol{v} \right) + \lambda \right\} \delta\phi \, \mathrm{d}\Omega \end{aligned} \tag{B.21}$$

B.2.2 Viscous dissipation rate minimization problem considering flow rate constraint

The flow rate constraint functional G is defined as follows,

$$G(\boldsymbol{u}) = \left(\frac{\int_{\Gamma_{out}} \boldsymbol{n}\cdot\boldsymbol{u} \mathrm{d}\Gamma}{rQ_{in}} - 1 \right)^2 - tol \tag{B.22}$$

while, r and tol mean the outflow rate fraction towards the inlet flow rate Q_{in} and the tolerance between the target outflow rate and actual outflow rate on the outlet boundary Γ_{out}, respectively.

The Lagrangian L can be expressed as follows by using the Lagrange undefined multipliers $\boldsymbol{v}$, q and λ_i with considering G_j $(j = 1,2)$(the volume constraint functional G_1 and

outflow rate constraint functional G_2.

$$L = J + \int_D \boldsymbol{v} \cdot F_1 \mathrm{d}\Omega + \int_D q F_2 \mathrm{d}\Omega + \lambda_1 G_1 + \lambda_2 G_2 \tag{B.23}$$

According to the variational of G_2, δG_2 is expressed as follows.

$$\delta G_2 = \lambda_2 \frac{\partial G_2}{\partial \boldsymbol{u}} \cdot \delta \boldsymbol{u} \tag{B.24}$$

And derivative of G_2 for adjoint equation and boundary condition are described below,

$$\begin{cases} \dfrac{\partial G_2}{\partial \boldsymbol{u}} = \dfrac{2}{rQ_{in}} \left(\dfrac{Q_{out}}{rQ_{in}} - 1 \right) \int_{\Gamma_{out}} \boldsymbol{n} \mathrm{d}\Gamma \\ \dfrac{\partial G_2}{\partial p} = 0 \end{cases} \tag{B.25}$$

while, $Q_{out} = \int_{\Gamma_{out}} \boldsymbol{n} \cdot \boldsymbol{u} \mathrm{d}\Gamma$ means actual outflow rate.

Therefore, by inserting the above conditions, the following Lagrangian variation δL transformation can be obtained.

$$\begin{aligned} \delta L = & \int_\Omega \left(\frac{\partial j_\Omega}{\partial \boldsymbol{u}} - \nabla \cdot \frac{\partial j_\Omega}{\partial \nabla \boldsymbol{u}} - \frac{1}{Re} \nabla^2 \boldsymbol{v} - (\boldsymbol{u} \cdot \nabla) \boldsymbol{v} + (\nabla \boldsymbol{u}) \cdot \boldsymbol{v} + \alpha \boldsymbol{v} + \nabla q \right) \delta \boldsymbol{u} \mathrm{d}\Omega \\ & + \int_\Omega \left(-\nabla \cdot \boldsymbol{v} + \frac{\partial j_\Omega}{\partial p} \right) \delta p \mathrm{d}\Omega \\ & + \left\{ \int_{\Gamma_p} \left(\frac{\partial j_\Omega}{\partial \nabla \boldsymbol{u}} \cdot \boldsymbol{n} + \frac{\partial j_\Gamma}{\partial \boldsymbol{u}} - q \cdot \boldsymbol{n} + \frac{1}{Re} \nabla \boldsymbol{v} \cdot \boldsymbol{n} + (\boldsymbol{u} \cdot \boldsymbol{n}) \cdot \boldsymbol{v} \right) \mathrm{d}\Gamma + \lambda_2 \frac{\partial G_2}{\partial \boldsymbol{u}} \right\} \delta \boldsymbol{u} \\ & + \int_{\Gamma_u} \left(\frac{\partial j_\Gamma}{\partial p} + \boldsymbol{v} \cdot \boldsymbol{n} \right) \delta p \mathrm{d}\Gamma + \int_D \left(\frac{\partial \alpha}{\partial \phi} \cdot \delta \phi \boldsymbol{u} \right) \cdot \boldsymbol{v} \mathrm{d}\Omega + \frac{\partial J}{\partial \phi} \cdot \delta \phi + \lambda_1 \left(\frac{\partial G_1}{\partial \phi} \cdot \delta \phi \right) \end{aligned} \tag{B.26}$$

Thus, adjoint equation and boundary condition can be written as,

$$-\frac{1}{Re}\nabla^2\boldsymbol{v}-(\boldsymbol{u}\cdot\nabla)\boldsymbol{v}+(\nabla\boldsymbol{u})\cdot\boldsymbol{v}+\nabla q=-\alpha\boldsymbol{v}-\left(\frac{1}{Re}\nabla^2\boldsymbol{u}+2\alpha\boldsymbol{u}-\nabla\cdot\frac{2}{Re}\nabla\boldsymbol{u}\right) \tag{B.27}$$

$$-\nabla\cdot\boldsymbol{v}=0 \tag{B.28}$$

$$\left(-q\cdot\boldsymbol{I}+\frac{1}{Re}\nabla\boldsymbol{v}\right)\cdot\boldsymbol{n}=-(\boldsymbol{u}\cdot\boldsymbol{n})\cdot\boldsymbol{v}-\frac{2}{Re}\nabla\boldsymbol{u}\cdot\boldsymbol{n}-\lambda_2\frac{2}{rQ_{in}}\left(\frac{Q_{out}}{rQ_{in}}-1\right)\cdot\boldsymbol{n}\quad on\quad\Gamma_p \tag{B.29}$$

$$\boldsymbol{v}\cdot\boldsymbol{n}=0\qquad on\quad\Gamma_u \tag{B.30}$$

Finally, the shape sensitivity for topology optimization problem can be obtained as,

$$\delta L=\left\{\int_D\frac{\partial j_\Omega}{\partial\phi}\mathrm{d}\Omega+\int_\Gamma\frac{\partial j_\Gamma}{\partial\phi}\mathrm{d}\Gamma+\int_D\left(\frac{\partial\alpha}{\partial\phi}\boldsymbol{u}\cdot\boldsymbol{v}\right)\mathrm{d}\Omega+\lambda_1\frac{\partial G_1}{\partial\phi}\right\}\delta\phi \tag{B.31}$$

Determination of the Lagrange undetermined multiplier λ for the flow rate constraint

In this topology optimization problem, the adjoint equation and adjoint boundary conditions are given by the expression (B.27)–(B.30). When the inequality condition is active, in order to determine the undefined lagrange multiplier λ_2, we introduce the concept of the augmented lagrange method as below,

$$\lambda_2=C\lambda_2^\star \tag{B.32}$$

where the arbitrary coefficient C and $\lambda_2^\star$ are expressed as

$$C=exp\left(\left(\frac{Q_{out}}{Q_{in}}\right)^2+a\right)^b \tag{B.33}$$

$$\lambda_2^\star=\frac{\int_{\Gamma_{out}}\left|\frac{\partial G_2}{\partial\boldsymbol{u}}\right|\mathrm{d}\Gamma}{\int_{\Gamma_{out}}\mathrm{d}\Gamma} \tag{B.34}$$

respectively, while a and b are the constant parameters, which the shape of exponential functional is defined by. Note that both $C \geq 0$ and $\lambda_2^\star \geq 0$ satisfy KKT condition. In the actual optimization problem dealing with in this note, when the inequality condition is inactive,

$$\lambda_2 = 0 \tag{B.35}$$

This indicates that the optimization problem with the inequality condition can be deal with as the optimization problem with the equality condition, if we can judge the inactive or active of the inequality condition.

Viscous dissipation rate minimization problem considering swirl constraint

The flow rate constraint functional G is defined as follows,

$$G(\boldsymbol{u}) = \int_{\Gamma_{out}} \left(S_w - {S_w}^t\right)^2 \mathrm{d}\Gamma - tol \tag{B.36}$$

while, ${S_w}^t$ means the initial Swirl number.

The Lagrangian L can be expressed as follows by using the Lagrange undefined multipliers $\boldsymbol{v}$, q and λ_i with considering G_j ($j = 1,2$)(the volume constraint functional G_1 and swirl constraint functional G_2.

$$L = J + \int_D \boldsymbol{v} \cdot F_1 \mathrm{d}\Omega + \int_D q F_2 \mathrm{d}\Omega + \lambda_1 G_1 + \lambda_2 G_2 \tag{B.37}$$

According to the variational of G_2, δG_2 is expressed as follows.

$$\delta G_2 = \lambda_2 \frac{\partial G_2}{\partial \boldsymbol{u}} \cdot \delta \boldsymbol{u} \tag{B.38}$$

And derivative of G_2 for adjoint equation and boundary condition are described below,

$$\begin{cases} \dfrac{\partial G_2}{\partial \boldsymbol{u}} = \int_{\Gamma_{out}} \begin{pmatrix} \dfrac{xv-y}{w} \\ \dfrac{x-yu}{w} \\ -\dfrac{xv-yu}{w^2} \end{pmatrix} \mathrm{d}\Gamma \\ \dfrac{\partial G_2}{\partial p} = 0 \end{cases} \tag{B.39}$$

Therefore, by inserting the above conditions, the following Lagrangian variation δL transformation can be obtained.

$$\begin{aligned} \delta L = & \int_\Omega \left(\frac{\partial j_\Omega}{\partial \boldsymbol{u}} - \nabla \cdot \frac{\partial j_\Omega}{\partial \nabla \boldsymbol{u}} - \frac{1}{Re}\nabla^2 \boldsymbol{v} - (\boldsymbol{u}\cdot\nabla)\boldsymbol{v} + (\nabla \boldsymbol{u})\cdot \boldsymbol{v} + \alpha \boldsymbol{v} + \nabla q \right) \delta \boldsymbol{u} \mathrm{d}\Omega \\ & + \int_\Omega \left(-\nabla \cdot \boldsymbol{v} + \frac{\partial j_\Omega}{\partial p} \right) \delta p \mathrm{d}\Omega \\ & + \left\{ \int_{\Gamma_p} \left(\frac{\partial j_\Omega}{\partial \nabla \boldsymbol{u}} \cdot \boldsymbol{n} + \frac{\partial j_\Gamma}{\partial \boldsymbol{u}} - q \cdot \boldsymbol{n} + \frac{1}{Re} \nabla \boldsymbol{v} \cdot \boldsymbol{n} + (\boldsymbol{u}\cdot\boldsymbol{n})\cdot \boldsymbol{v} \right) \mathrm{d}\Gamma + \lambda_2 \frac{\partial G_2}{\partial \boldsymbol{u}} \right\} \delta \boldsymbol{u} \\ & + \int_{\Gamma_u} \left(\frac{\partial j_\Gamma}{\partial p} + \boldsymbol{v}\cdot\boldsymbol{n} \right) \delta p \mathrm{d}\Gamma + \int_D \left(\frac{\partial \alpha}{\partial \phi} \cdot \delta\phi \boldsymbol{u} \right) \cdot \boldsymbol{v} \mathrm{d}\Omega + \frac{\partial J}{\partial \phi} \cdot \delta\phi + \lambda_1 \left(\frac{\partial G_1}{\partial \phi} \cdot \delta\phi \right) \end{aligned} \tag{B.40}$$

Thus, adjoint equation and boundary condition can be written as,

$$-\frac{1}{Re}\nabla^2 \boldsymbol{v} - (\boldsymbol{u}\cdot\nabla)\boldsymbol{v} + (\nabla \boldsymbol{u})\cdot\boldsymbol{v} + \nabla q = -\alpha \boldsymbol{v} - \left(\frac{1}{Re}\nabla^2 \boldsymbol{u} + 2\alpha \boldsymbol{u} - \nabla \cdot \frac{2}{Re}\nabla \boldsymbol{u} \right) \tag{B.41}$$

$$-\nabla \cdot \boldsymbol{v} = 0 \tag{B.42}$$

$$\left(-q\cdot \boldsymbol{I} + \frac{1}{Re}\nabla \boldsymbol{v} \right) \cdot \boldsymbol{n} = -(\boldsymbol{u}\cdot\boldsymbol{n})\cdot\boldsymbol{v} - \frac{2}{Re}\nabla \boldsymbol{u}\cdot\boldsymbol{n} - \lambda_2 \begin{pmatrix} \dfrac{xv-y}{w} \\ \dfrac{x-yu}{w} \\ -\dfrac{xv-yu}{w^2} \end{pmatrix} \quad on \quad \Gamma_p \tag{B.43}$$

$$\boldsymbol{v}\cdot\boldsymbol{n} = 0 \qquad on \quad \Gamma_u \tag{B.44}$$

Finally, the shape sensitivity for topology optimization problem can be obtained as,

$$\delta L = \left\{ \int_D \frac{\partial j_\Omega}{\partial \phi} \mathrm{d}\Omega + \int_\Gamma \frac{\partial j_\Gamma}{\partial \phi} \mathrm{d}\Gamma + \int_D \left(\frac{\partial \alpha}{\partial \phi} \boldsymbol{u} \cdot \boldsymbol{v} \right) \mathrm{d}\Omega + \lambda_1 \frac{\partial G_1}{\partial \phi} \right\} \delta\phi \tag{B.45}$$

Determination of the Lagrange undetermined multiplier λ for the swirl constraint

In this topology optimization problem, the adjoint equation and adjoint boundary conditions are given by the expression (B.41)–(B.44). When the inequality condition is active, in order to determine the undefined lagrange multiplier λ_2, we introduce the concept of the augmented lagrange method as below,

$$\lambda_2 = C\lambda_2^\star \tag{B.46}$$

where the arbitrary coefficient C and $\lambda_2^\star$ are expressed as

$$C = exp\left(\left(\frac{Q_{out}}{Q_{in}} \right)^2 + a \right)^b \tag{B.47}$$

$$\lambda_2^\star = \frac{\int_{\Gamma_{out}} \left| \frac{\partial G_2}{\partial \boldsymbol{u}} \right| \mathrm{d}\Gamma}{\int_{\Gamma_{out}} \mathrm{d}\Gamma} \tag{B.48}$$

respectively, while a and b are the constant parameters, which the shape of exponential functional is defined by. Note that both $C \geq 0$ and $\lambda_2^\star \geq 0$ satisfy KKT condition. In the actual optimization problem dealing with in this note, when the inequality condition is inactive,

$$\lambda_2 = 0 \tag{B.49}$$

This indicates that the optimization problem with the inequality condition can be deal with as the optimization problem with the equality condition, if we can judge the inactive or active of the inequality condition.

B.2.3 Swirl maximization problem

In case the x-y plane is the specific outlet plane and the z direction is the rotational axis for the objective functional j_Γ, the objective functional is as follows,

$$j_\Omega = 0 \tag{B.50}$$

$$j_\Gamma = S_w = \frac{xv - yu}{w} \tag{B.51}$$

in which the characteristic length $r = 1$ is used.

Therefore, each derivative of j_Ω and j_Γ for adjoint equation and boundary condition are described below,

$$\begin{cases} \dfrac{\partial j_\Omega}{\partial \boldsymbol{u}} = 0 \\ \dfrac{\partial j_\Omega}{\partial \nabla \boldsymbol{u}} = 0 \\ \dfrac{\partial j_\Omega}{\partial p} = 0 \\ \dfrac{\partial j_\Gamma}{\partial p} = 0 \\ \dfrac{\partial j_\Gamma}{\partial \boldsymbol{u}} = \begin{pmatrix} \dfrac{xv - y}{w} \\ \dfrac{x - yu}{w} \\ -\dfrac{xv - yu}{w^2} \end{pmatrix} \end{cases} \tag{B.52}$$

Then, by substituting each derivartive, the adjoint equation and boundary condition for the swirl maximization problem can be obtained as,

$$-\frac{1}{Re}\nabla^2\boldsymbol{v}-(\boldsymbol{u}\cdot\nabla)\boldsymbol{v}+(\nabla\boldsymbol{u})\cdot\boldsymbol{v}+\nabla q=-\alpha\boldsymbol{v} \tag{B.53}$$

$$-\nabla\cdot\boldsymbol{v}=0 \tag{B.54}$$

$$\left(-q\cdot\boldsymbol{I}+\frac{1}{Re}\nabla\boldsymbol{v}\right)\cdot\boldsymbol{n}=-(\boldsymbol{u}\cdot\boldsymbol{n})\cdot\boldsymbol{v}-\begin{pmatrix}(xv-y)/w\\(x-yu)/w\\-(xv-yu)/w^2\end{pmatrix}\quad on\quad \Gamma_p \tag{B.55}$$

$$\boldsymbol{v}\cdot\boldsymbol{n}=0\qquad on\quad \Gamma_u \tag{B.56}$$

Consequently, as the each derivative with respect to the level set functional ϕ are

$$\begin{cases}\dfrac{\partial j_\Omega}{\partial\phi}=0\\[2ex]\dfrac{\partial j_\Gamma}{\partial\phi}=0\\[2ex]\dfrac{\partial\alpha}{\partial\phi}=\alpha_{min}-\alpha_{max}\\[2ex]\dfrac{\partial G}{\partial\phi}=1\end{cases} \tag{B.57}$$

the shape sensitivity for topology optimization problem can be obtained as,

$$\begin{aligned}\delta L&=\left\{\int_D\frac{\partial j_\Omega}{\partial\phi}\mathrm{d}\Omega+\int_\Gamma\frac{\partial j_\Gamma}{\partial\phi}\mathrm{d}\Gamma+\int_D\left(\frac{\partial\alpha}{\partial\phi}\boldsymbol{u}\cdot\boldsymbol{v}\right)\mathrm{d}\Omega+\lambda\frac{\partial G}{\partial\phi}\right\}\delta\phi\\&=\int_D\{(\alpha_{min}-\alpha_{max})\,\boldsymbol{u}\boldsymbol{v}+\lambda\}\,\delta\phi\,\mathrm{d}\Omega\end{aligned} \tag{B.58}$$

References

[1] Aage, N., Poulsen, T. H., Gersborg-Hansen, A., and Sigmund, O. (2008). Topology optimization of large scale stokes flow problems. *Structural and Multidisciplinary Optimization*, 35(2):175–180.

[2] Allaire, G., de Gournay, F., Jouve, F., and Toader, A.-M. (2005). Structural optimization using topological and shape sensitivity via a level set method. *Control and Cybernetics*, 34(1):59–81.

[3] Allaire, G., Jouve, F., and Toader, A.-M. (2004). Structural optimization using sensitivity analysis and a level-set method. *Journal of Computational Physics*, 194(1):363–393.

[4] Amstutz, S. (2005). The topological asymptotic for the Navier-Stokes equations. *ESAIM: Control, Optimisation and Calculus of Variations*, 11(3):401–425.

[5] Amstutz, S. (2006). Topological sensitivity analysis for some nonlinear PDE systems. *Journal de Mathématiques Pures et Appliquées*, 85(4):540–557.

[6] Amstutz, S. and Andrä, H. (2006). A new algorithm for topology optimization using a level-set method. *Journal of Computational Physics*, 216(2):573–588.

[7] Angot, P., Bruneau, C.-H., and Fabrie, P. (1999). A penalization method to take into account obstacles in incompressible viscous flows. *Numerische Mathematik*, 81(4):497–520.

[8] Bajura, R. A. (1971). A model for flow distribution in manifolds. *Journal of Engineering for Power*, 93(1):7–12.

[9] Bajura, R. A. and Jones, E. H. (1976). Flow distribution manifolds. *Journal of Fluids Engineering*, 98(1):654–666.

[10] Bassiouny, M. K. and Martin, H. (1984a). Flow distribution and pressure drop in plate heat exchangers-I U-type arrangement. *Chemical Engineering Science*, 39(3):693–700.

[11] Bassiouny, M. K. and Martin, H. (1984b). Flow distribution and pressure drop in plate heat exchangers-Ⅱ Z-type arrangement. *Chemical Engineering Science*, 39(3):701–704.

[12] Bendse, M. P. and Kikuchi, N. (1988). Generating optimal topologies in structural design using a homogenization method. *Computer Methods in Applied Mechanics and Engineering*, 71(2):197–224.

[13] Bendse, M. P. and Sigmund, O. (1997). *Optimization of Structural Topology, Shape and Material*. Springer, Berlin.

[14] Borrvall, T. and Petersson, J. (2003). Topology optimization of fluids in stokes flow. *International Journal of Numerical Methods in Fluids*, 41(1):77–107.

[15] Bruns, T. E. (2007). Topology optimization of convection-dominated, steady-state heat transfer problems. *International Journal of Heat and Mass Transfer*, 50(15–16):2859–2873.

[16] Bueno-Orovio, A., Castro, C., Palacios, F., and Zuazua, E. (2012). Continuous Adjoint Approach for the Spalart-Allmaras Model in Aerodynamic Optimization. *AIAA Journal*, 50(3):631–646.

[17] Burger, M., Hackl, B., and Ring, W. (2004). Incorporating topological derivatives into level set methods. *Journal of Computational Physics*, 194(1):344–362.

[18] Challis, V. J. and Guest, J. K. (2009). Level set topology optimization of fluids in stokes flow. *International Journal of Numerical Methods in Engineering*, 79(10):1284–1308.

[19] Deng, Y., Liu, Z., Wu, J., and Wu, Y. (2013). Topology optimization of steady Navier-Stokes flow with body force. *Computer Methods in Applied Mechanics and Engineering*, 255(1):306–321.

[20] Deng, Y., Liu, Z., Zhang, P., Liu, Y., and Wu, Y. (2011). Topology optimization of unsteady incompressible Navier-Stokes flows. *Journal of Computational Physics*, 230(24):6688–6708.

[21] Diaz, A. R. and Kikuchi, N. (1992). Solutions to shape and topology eigenvalue optimization problems using a homogenization method. *International Journal of Numerical Methods in Engineering*, 35(7):1487–1502.

[22] Dijk, N. P. V., Maute, K., Langelaar, M., and Keulen, F. V. (2013). Level-set methods for structural topology optimization: a review. *Structural and Multidisciplinary Optimization*, 48(3):437–472.

[23] Dilgen, C. B., Dilgen, S. B., Fuhrman, D. R., Sigmund, O., and Lazarov, B. S. (2018). Topology optimization of turbulent flows. *Computer Methods in Applied Mechanics and Engineering*, 331(1):363–393.

[24] Duan, X. B., Ma, Y. C., and Zhang, R. (2008). Shape-topology optimization for Navier-Stokes problem using variational level set method. *Journal of Computational and Applied Mathematics*, 222(2):487–499.

[25] Dupuis, A., Chatelain, P., and Koumoutsakos, P. (2008). An immersed boundary–lattice-Boltzmann method for the simulation of the flow past an impulsively started cylinder. *Journal of Computational Physics*, 227(9):4486–4498.

[26] Dwight, R. P. and Brezillon, J. (2006). Effect of various approximations of the discrete adjoint on gradient-based optimization. 44th AIAA Aerospace Sciences Meeting and Exhibit.

[27] Eschenauer, H., Kobelev, V., and Schumacher, A. (1994). Bubble method for topology and shape optimization of structures. *Structural Optimization*, 8(1):42–51.

[28] Fadlun, E. A., Verzicco, R., Orlandi, P., and Mohd-Yusof, J. (2000). Combined immersed-boundary finite-difference methods for three-dimensional complex flow simulations. *Journal of Computational Physics*, 161(1):35–60.

[29] Feng, Z.-G. and Michaelides, E. E. (2005). Proteus: a direct forcing method in the simulations of particulate flows. *Journal of Computational Physics*, 202(1):20–51.

[30] Gersborg-Hansen, A., Berggren, M., and Dammann, B. (2006). Topology optimization of mass distribution problems in Stokes flow. In *IUTAM symposium on topological design optimization of structures, machines and materials*, pages 356–374, Netherlands. Springer.

[31] Gersborg-Hansen, A., Sigmund, O., and Haber, R. B. (2005). Topology optimization of channel flow problems. *Structural and Multidisciplinary Optimization*, 30(3):181–192.

[32] Hassan, J. M., Mohammed, W. S., Mohamed, T. A., and Alawee, W. H. (2014). Review on Single-Phase Fluid Flow Distribution in Manifold. *International Journal of Science and Research*, 3(1):325–330.

[33] He, L., Kao, C.-Y., and Osher, S. (2007). Incorporating topological derivatives into shape derivatives based level set methods. *Journal of Computational Physics*, 225(1):891–909.

[34] Hestenes, M. R. (1969). Multiplier and gradient methods. *Journal of Optimization Theory and Applications*, 4(5):303–320.

[35] Iaccarino, G. and Verzicco, R. (2003). Immersed boundary technique for turbulent flow simulations. *Applied Mechanics Reviews*, 56(3):331–347.

[36] Kalitzin, G., Medic, G., Iaccarino, G., and Durbin, P. (2005). Near-wall behavior of RANS turbulence models and implications for wall functions. *Journal of Computational Physics*, 204(1):265–291.

[37] Kavvadias, I. S., Papoutsis-Kiachagias, E. M., Dimitrakopoulos, G., and Giannakoglou, K. C. (2015). The continuous adjoint approach to the k-omega SST turbulence model with applications in shape optimization. *Engineering Optimization*, 47(11):1523–1542.

[38] Kontoleontos, E. A., Papoutsis-Kiachagias, E. M., Zymaris, A. S., Papadimitriou, D. I., and Giannakoglou, K. C. (2013). Adjoint-based constrained topology optimization for viscous flows, including heat transfer. *Engineering Optimization*, 45(8):941–961.

[39] Kreissl, S. and Maute, K. (2012). Levelset based fluid topology optimization using the extended finite element method. *Structural and Multidisciplinary Optimization*, 46(3):311–326.

[40] Kreissl, S., Pingen, G., and Maute, K. (2011). Topology optimization for unsteady flow. *International Journal of Numerical Methods in Engineering*, 87(13):1229–1253.

[41] Kubo, S., Yaji, K., Yamada, T., Izui, K., and Nishiwaki, S. (2016). A level set-based topology optimization for optimal manifold designs with flow uniformity in plate-type microchannel reactors. *Structural and Multidisciplinary Optimization*, 111(11):1–17.

[42] Launder, B. and Spalding, D. (1974). The numerical computation of turbulent flows. *Computer Methods in Applied Mechanics and Engineering*, 3(2):269–289.

[43] Lee, K. (2012). *Topology optimization of convective cooling system designs*. PhD thesis, The University of Michigan.

[44] Liu, Z., Gao, Q., Zhang, P., Xuan, M., and Wu, Y. (2011). Topology optimization of fluid channels with flow rate equality constraints. *Structural and Multidisciplinary Optimization*, 44(1):31–37.

[45] Ma, Z. D., Kikuchi, N., and Cheng, H. C. (1995). Topological design for vibrating structures. *Computer Methods in Applied Mechanics and Engineering*, 121(1–4):259–280.

[46] Majundar, S., Iaccarino, G., and Durbin, P. (2001). RANS solvers with adaptive structured boundary non-conforming grids. *Annual Research Briefs 2001*, pages 353–366.

[47] Matsumori, T., Kondoh, T., Kawamoto, A., and Nomura, T. (2013). Topology optimization for fluid-thermal interaction problems under constant input power. *Structural and Multidisciplinary Optimization*, 47(4):571–581.

[48] Mittal, S. and Iaccarino, G. (2005). Immersed boundary methods. *Annual Review of Fluid Mechanics*, 37:239–261.

[49] Mohammadi, M., Jovanovic, G. N., and Sharp, K. V. (2013). Numerical study of flow uniformity and pressure characteristics within a microchannel array with triangular manifolds. *Computers & Chemical Engineering*, 52:134–144.

[50] Nishiwaki, S., Frecker, M. I., Min, S., and Kikuchi, N. (1998). Topology optimization of compliant mechanisms using the homogenization method. *International Journal of Numerical Methods in Engineering*, 42(3):535–559.

[51] Olesen, L. H., Okkels, F., and Bruus, H. (2006). A high-level programming-language implementation of topology optimization applied to steady-state Navier-Stokes flow. *International Journal of Numerical Methods in Engineering*, 65(7):975–1001.

[52] Osher, S. and Sethian, J. A. (1988). Front propagating with curvature dependent speed: algorithms based on Hamilton-Jacobi formulations. *Journal of Computational Physics*, 78(1):12–49.

[53] Othmer, C. (2008). A continuous adjoint formulation for the computation of topological and surface sensitivities of ducted flows. *International Journal of Numerical Methods in Fluids*, 58:861–877.

[54] Otomori, M., Yamada, T., Izui, K., and Nishiwaki, S. (2015). Matlab code for a level set-based topology optimization method using a reaction diffusion equation. *Structural and Multidisciplinary Optimization*, 51(5):1159–1172.

[55] Pan, M., Tang, Y., Pan, L., and Lu, L. (2008). Optimal design of complex manifold geometries for uniform flow distribution between microchannels. *Chemical Engineering Journal*, 137(2):339–346.

[56] Papadimitriou, D. I. and Giannakoglou, K. C. (2007). A continuous adjoint method with objective function derivatives based on boundary integrals, for inviscid and viscous flows. *Computers & Fluids*, 36(2):325–341.

[57] Papoutsis-Kiachagias, E. M., Kontoleontos, E. A., Zymaris, A. S., Papadimitriou, D. I., and Giannakoglou, K. C. (2011). Constrained topology optimization for laminar and turbulent flows, including heat transfer. EUROGEN 2011.

[58] Peskin, C. S. (1972a). *Flow patterns around heart valves: A digital computer method for solving the equations of motion*. PhD thesis, Albert Einstein College of Medicine.

[59] Peskin, C. S. (1972b). Flow patterns around heart valves: A numerical method. *Journal of Computational Physics*, 10(2):252–271.

[60] Pironneau, O. (1973). On optimum profiles in Stokes flow. *Journal of Fluid Mechanics*, 59(1):117–128.

[61] Pironneau, O. (1974). On optimum design in fluid mechanics. *Journal of Fluid Mechanics*, 64(1):97–110.

[62] Rockafellar, R. T. (1973). A dual approach to solving nonlinear programming problems by unconstrained optimization. *Mathematical Programming*, 5(1):354–373.

[63] Sarstedt, P., Kachel, G., Ettrich, J., and Bühler, K. (2016). Topology optimization for fluid employing local optimality criteria. ECCOMAS Congress 2016.

[64] Shu, C., Liu, N., and Chew, Y. (2007). A novel immersed boundary velocity correction–lattice Boltzmann method and its application to simulate flow past a circular cylinder. *Journal of Computational Physics*, 226(2):1607–1622.

[65] Sigmund, O. (1997). On the design of compliant mechanisms using topology optimization. *Mechanics Based Design of Structures and Machines*, 25(4):493–524.

[66] Sigmund, O. and Petersson, J. (1998). Numerical instabilities in topology optimization: A survey on procedures dealing with checkerboards, mesh-dependencies and local minima. *Structural and Multidisciplinary Optimization*, 16:68–75.

[67] Smagorinsky, J. (1963). General circulation experiments with the primitive equations i. the basic experiment. *Monthly Weather Review*, 91(3):99–164.

[68] Sokolowski, J. and Zochowski, A. (1999). On the Topological Derivative in Shape Optimization. *SIAM Journal of Control and Optimization*, 37(4):1251–1272.

[69] Spalart, P., Jou, W., Strelets, M., and Allmaras, S. (1997). Comments on the Feasibility of LES for Wings, and on a Hybrid RANS/LES Approach. Proc. First AFOSR International Conference on DNS/LES.

[70] Spalding, D. B. (1961). A Single Formula for the "Law of the Wall". *Journal of Applied Mechanics*, 28(3):455–458.

[71] Srinath, D. and Mittal, S. (2010). An adjoint method for shape optimization in unsteady viscous flows. *Journal of Computational Physics*, 229(6):1994–2008.

[72] Suzuki, K. and Kikuchi, N. (1991). A homogenization method for shape and topology optimization. *Computer Methods in Applied Mechanics and Engineering*, 93(3):291–318.

[73] Tonkovich, A., Kuhlmann, D., Rogers, A., McDaniel, J., Fitzgerald, S., Arora, R., and Yuschak, T. (2005). Microchannel technology scale-up to commercial capacity. *Chemical Engineering Research and Design*, 83(A6):634–639.

[74] Tonomura, O., Tanaka, S., Noda, M., Kano, M., Hasebe, S., and Hashimoto, I. (2004). CFD-based optimal design of manifold in plate-fin microdevices. *Chemical Engineering Journal*, 101(1–3):397–402.

[75] Tseng, Y.-H. and Ferziger, J. H. (2003). A ghost-cell immersed boundary method for flow in complex geometry. *Journal of Computational Physics*, 192(2):593–623.

[76] Uhlmann, M. (2005). An immersed boundary method with direct forcing for the simulation of particulate flows. *Journal of Computational Physics*, 209(2):448–476.

[77] Wang, M. Y., Wang, X., and Guo, D. (2003). A level set method for structural topology optimization. *Computer Methods in Applied Mechanics and Engineering*, 192(1-–2):227–246.

[78] Wang, Z., Fan, J., and Luo, K. (2008). Combined multi-direct forcing and immersed boundary method for simulating flows with moving particles. *International Journal of Multiphase Flow*, 34(3):283–302.

[79] Wilcox, D. (1993). *Turbulence Modeling for CFD*. DCW Industries, Inc., La Canada, CA.

[80] Yaji, K., Yamada, T., Yoshino, M., Matsumoto, T., Izui, K., and Nishiwaki, S. (2014). Topology optimization using the lattice Boltzmann method incorporating level set boundary expressions. *Journal of Computational Physics*, 274(1):158–181.

[81] Yamada, T., Izui, K., Nishiwaki, S., and Takezawa, A. (2010). A topology optimization method based on the level set method incorporating a fictitious interface energy. *Computer Methods in Applied Mechanics and Engineering*, 199(45–48):2876–2891.

[82] Yoon, G. H. (2016). Topology optimization for turbulent flow with Spalart-Allmaras model. *Computer Methods in Applied Mechanics and Engineering*, 303(1):288–311.

[83] Zhou, S. and Li, Q. (2008). A variational level set method for the topology optimization of steady-state Navier-Stokes flow. *Journal of Computational Physics*, 227(24):10178–10195.

[84] Zymaris, A. S., Papadimitriou, D. I., Giannakoglou, K. C., and Othmer, C. (2009). Continuous adjoint approach to the Spalart-Allmaras turbulence model for incompressible flows. *Computers & Fluids*, 38(8):1528–1538.

[85] Zymaris, A. S., Papadimitriou, D. I., Giannakoglou, K. C., and Othmer, C. (2010). Adjoint wall functions: a new concept for use in aerodynamic shape optimization. *Journal of Computational Physics*, 229(13):5228–5245.

List of Publications

International Journal Papers

[1] Kentaro Yaji, Takayuki Yamada, Seiji Kubo, Kazuhiro Izui and Shinji Nishiwaki, A topology optimization method for a coupled thermal-fluid problem using level set boundary expressions, *Journal of Heat and Mass Transfer*, Vol. 81, Issue 1, 2015, pp. 878–888.

[2] Seiji Kubo, Kentaro Yaji, Takayuki Yamada, Kazuhiro Izui and Shinji Nishiwaki, A level set-based topology optimization method for optimal manifold designs with flow uniformity in plate-type microchannel reactors, *Structural and Multidisciplinary Optimization*, Vol.55, Issue 4, 2017, pp.1311-1327.

[3] Seiji Kubo, Atsushi Koguchi, Kentaro Yaji, Takayuki Yamada, Kazuhiro Izui and Shinji Nishiwaki, Level set-based topology optimization for turbulent flow using an immersed boundary method, *Journal of Computational Physics*, *submitted*.

Domestic Journal Papers (in Japanese)

[1] Kentaro Yaji, Takayuki Yamada, Seiji Kubo, Kazuhiro Izui and Shinji Nishiwaki, Topology optimization method based on level set method in Oseen flow, *Transactions*

of the Japan Society for Computational Methods in Engineering, Vol. 12, No. 02-121212, 2012, pp. 7–12.

[2] Seiji Kubo, Kentaro Yaji, Takayuki Yamada, Kazuhiro Izui and Shinji Nishiwaki, Level set-based topology optimization of steady state incompressible viscous flows under outflow rate inequality constraint, *Transactions of the Japan Society of Mechanical Engineers*, Vol. 80, No. 815, 2014, pp. DSM0213.

[3] Atsushi Koguchi, Seiji Kubo, Kentaro Yaji, Takayuki Yamada, Kazuhiro Izui and Shinji Nishiwaki, Topology optimization method for incompressible viscous flow applying an immersed boundary method, *Transactions of the Japan Society of Mechanical Engineers*, Vol. 84, No. 860, 2018, pp. 17-00551.

International Conferences

[1] Seiji Kubo, Kazuhiro Izui, Shinji Nishiwaki, Level-set based topology optimization of Stokes flow, 10th World Congress on Computational Mechanics (WCCM-10), 8 - 13, July, 2012, Sao Paulo, Brazil, No. 19002.

[2] Seiji Kubo, Kentaro Yaji, Takayuki Yamada, Kazuhiro Izui, Shinji Nishiwaki, Topology optimization of steady incompressible viscous flow for fluidic device, JSME-CMD International Computational Mechanics Symposium 2012 (JSME-CMD ICMS 2012), 9 - 11, October, 2012, Kobe, Japan, No. 105.

[3] Kentaro Yaji, Takayuki Yamada, Seiji Kubo, Kazuhiro Izui, Shinji Nishiwaki, A topology optimization method under Oseen flow based on the level set method, ICOME/JASCOME Symposium 2012, 12 - 14, December, 2012, Kyoto, Japan, No. J02.

[4] Seiji Kubo, Kentaro Yaji, Takayuki Yamada, Kazuhiro Izui, Shinji Nishiwaki, Level set based topology optimization of switching fluidic device for incompressible viscous flow, 10th World Congress of Structural and Multidisciplinary Optimisation (WCSMO-10), 19 - 24, May, 2013, Orland, Florida, USA, No. 5328.

[5] Seiji Kubo, Kentaro Yaji, Takayuki Yamada, Kazuhiro Izui, Shinji Nishiwaki, Flow rate constrained topology optimization of manifold with level set-based boundary representation, 5th Asia Pacific Congress on Computational Mechanics (APCOM 2013), 11 - 14, December, 2013, Singapore, Singapore, No. 1922.

[6] Seiji Kubo, Kentaro Yaji, Takayuki Yamada, Kazuhiro Izui, Shinji Nishiwaki, Topology optimization of hydrodynamic Microfluidic mixer based on the level-set based boundary expression, International Conference on Engineering and Applied Sciences Optimization (OPT-i), 4 - 6, June, 2014, Kos Island, Greece, No. 3251.

[7] Seiji Kubo, Atsushi Koguchi, Kentaro Yaji, Takayuki Yamada, Kazuhiro Izui, Shinji Nishiwaki, Level set-based topology optimization method for fluid problem incorporating with an immersed boundary method, 1st Asian Congress of Structural and Multidisciplinary Optimization (ACSMO 2016), 22 - 26, May, 2016, Nagasaki, Japan, No. 3A2-2.

[8] Seiji Kubo, Atsushi Koguchi, Kentaro Yaji, Takayuki Yamada, Kazuhiro Izui, Shinji Nishiwaki, A level-set based topology optimization method for incompressible flow incorporating with an immersed boundary method, International Conference on Evolutionary and Deterministic Methods for Design Optimization and Control with Applications to Industrial and Societal Problems (EUROGEN 2017), 13 - 15, September, 2017, Madrid, Spain, No. 039.

Domestic Conferences

[1] 矢地謙太郎，山田崇恭，久保世志，泉井一浩，西脇眞二， 流体冷却式ヒートシンクを対象としたレベルセット法に基づくトポロジー最適化，第18回計算工学講演会，日本計算工学会， 2013年6月19日-21日，東京，日本，No. F-13-2.

[2] 久保世志，矢地謙太郎，山田崇恭，泉井一浩，西脇眞二， 流量制約を考慮した非圧縮粘性流れのレベルセット法に基づくトポロジー最適化， 日本機械学会第23回設計工学・システム部門講演会， 日本機械学会，2013年10月23日-25日，読谷村，日本，No.1113.

[3] 古口睦士，久保世志，矢地謙太郎，山田崇恭，泉井一浩，西脇眞二, 角運動量を考慮した非圧縮性粘性流れのトポロジー最適化, 第28回計算力学講演会，日本機械学会， 2015年10月10日-12日，横浜，日本，No. 192.

[4] 古口睦士，久保世志，矢地謙太郎，山田崇恭，泉井一浩，西脇眞二, 壁面の取り扱いに埋め込み境界法を用いた定常の非圧縮性粘性流れのトポロジー最適化, 第26回設計工学・システム部門講演会，日本機械学会，2016年10月8日-10日，横浜，日本，No. 2309.

[5] 古口睦士，久保世志，矢地謙太郎，山田崇恭，泉井一浩，西脇眞二, 埋め込み境界で壁法則を適用した定常の非圧縮性粘性流れのトポロジー最適化, 第12回最適化シンポジウム2016(OPTIS 2016)，日本機械学会，2016年12月6日-7日，札幌，日本，No. 1112.